



TECHNISCHE  
UNIVERSITÄT  
WIEN  
Vienna University of Technology

## DIPLOMARBEIT

# Electron Vortex Beams in Magnetic Fields

Ausgeführt am Institut für

Festkörperphysik  
der Technischen Universität Wien

unter der Anleitung von a.o. Univ.Prof. Dipl.-Ing. Mag.rer.nat. Dr.techn. Peter  
Schattschneider

durch

Schachinger Thomas

Radetzkystraße 10/13, 1030 Wien

---

Datum

---

Unterschrift

## Table of Contents

1	Introduction .....	11
2	Theoretical Background.....	15
2.1	Peculiar Electron Vortex Beam Rotations.....	15
2.1.1	The Transmission Electron Microscope.....	15
2.1.2	TEM Objective Lens .....	18
2.1.3	Standard Image Rotation in TEM – Larmor-Rotation .....	22
2.1.4	Electron Vortex Beams .....	25
2.1.4.1	Wave-Mechanical Description.....	25
2.1.4.2	Classical Description .....	31
2.1.5	Theoretical Prediction of Peculiar Rotations – Landau States and LG-Beams in Uniform Magnetic Fields.....	32
2.1.6	Semi-classical Derivation of the Electron Vortex Rotation in a Magnetic Lens Field:.....	38
2.2	Spin-to-Orbit Conversion – The Electron STOC-Process .....	44
2.2.1	Electron Spin - Polarization.....	44
2.2.2	STOC-Process for Electrons .....	45
3	Methods.....	49
3.1	Vortex Rotation Experiments.....	49
3.1.1	Experimental Parameters .....	49
3.1.2	Experimental Setup .....	51
3.1.3	Electron Beam Cutting.....	54
3.1.4	Experimental Procedure – Cutting the Line of Electron Vortices Step by Step.....	60
3.1.5	Azimuthal Angle Determination .....	62
3.1.6	Numerical Simulation of the Vortex Rotation Experiment.....	68
3.2	Numerical Simulation of the proposed STOC-Device .....	70
4	Results.....	72
4.1	Vortex Rotation Results .....	72
4.1.1	Image Rotation of a Cu-Grid on the Tecnai G20 LaB <sub>6</sub> TEM.....	72
4.1.2	Image Rotation of a Silicon-Knife-Edge on the Tecnai F20 FEG TEM .....	75
4.1.3	Measurements of the Vortex Rotation.....	77
4.1.4	Numerical Results.....	90
4.2	STOC-Process Simulation Results.....	98
5	Conclusion and Outlook.....	108
6	Bibliography.....	113

## List of Figures

Figure 1: Left: Vortex motion in air induced by an airplanes' wing tip. ....	11
Figure 2: Left: Picture of the Philips/FEI Tecnai G2 F20 TEM at the TU-Vienna.....	17
Figure 3: Left: Side-view picture of the objective pole piece of a FEI Tecnai F20.....	19
Figure 4: Illustrates the "Pillendose" for the calculation of the radial component .....	20
Figure 5: Course of some electron paths incident from the right hand side. ....	21
Figure 6: Electron optical imaging through a rotational symmetric magnetic field .....	22
Figure 7: Drawing, showing the used cylindrical coordinate system for the electrons motion .....	23
Figure 8: Sketch, showing why LR instead of cyclotron motion is observed in the TEM .....	25
Figure 9: Left: Transmission function of the holographic mask. ....	27
Figure 10: Calculated transverse intensity distributions of LG beams.....	28
Figure 11: Left: The picture shows xy- and xz-profiles of the first 12 LG modes .....	29
Figure 12: Graphical representation of a simulation of the wavefronts and transverse amplitude ...	32
Figure 13: Simulated transverse intensity distribution and APC of LS-LG-modes .....	35
Figure 14: Plot of the probability density of a OAM - "balanced" superposition .....	36
Figure 15: Plot of the probability density of an OAM - "unbalanced" superposition .....	37
Figure 16: The same as in Figure 15, but with reversed sign of the topological charge .....	37
Figure 17: Shows the azimuthal velocity components for pure rotational- and irrotational vortices.....	39
Figure 18: Diagram, showing the azimuthal angle of rotation over the z-shift .....	42
Figure 19: Left: q-plate patterns for different values of $\alpha_0$ and $q$ .....	46
Figure 20: Proposed integration scheme of an electron STOC device (q-filter) into a TEM column ...	47
Figure 21: Left: SEM image of the holographic electron vortex mask .....	50
Figure 22: Sketch of the experimental setup (not to scale).....	52
Figure 23: Left: The sketch shows schematically, how to align the KE in the TEM sample holder.....	53
Figure 24: Schematic drawing to illustrate azimuthal angle errors introduced.....	55
Figure 25: Angle error estimation over the z-shift for different surface roughnesses. ....	56
Figure 26: Schematic sketch showing the influence of the breaking edge angle $\Phi_{KE}$ .....	57
Figure 27: Left: Side view SEM picture of the Si-KE. ....	57
Figure 28: SEM side view of the Si-KE region marked with a red arrow in Figure 27 .....	58
Figure 29: Shows a screenshot of the image analysis software DM3 .....	63
Figure 30: Compares three different contrast levels of a single vortex order .....	64
Figure 31: Two intensity distributions of cut EVB with different maximum intensities .....	65

Figure 32: Depicts the angular spread of a single pixel and its bisector for a typical measurement ..	66
Figure 33: Sketch, showing the geometrical setup to determine the skew angle .....	67
Figure 34: TEM images of a z-shift series of a Cu-grid at 92.8 % OL excitation .....	72
Figure 35: Shows the measured azimuthal rotation angle data of the Cu-grid z-shift series .....	73
Figure 36: Visualisation of the estimated slopes $\bar{\sigma}$ and OL fields $B_z$ with their standard errors .....	75
Figure 37: TEM image series of the Si-KE rotation experiment at 95.8 % OL excitation .....	76
Figure 38: Diagram shows the measured azimuthal rotation angle data of the Si-KE z-shift series ...	76
Figure 39: Images of EVB rotation, part one (+ 350 $\mu\text{m}$ to + 175 $\mu\text{m}$ ) of a full z-shift series .....	78
Figure 40: Part two of the same z-shift series ranging from + 150 $\mu\text{m}$ to - 125 $\mu\text{m}$ .....	79
Figure 41: Part three of the same z-shift series ranging from - 150 $\mu\text{m}$ to - 375 $\mu\text{m}$ . .....	80
Figure 42: Experimental image at a z-shift height of 0 $\mu\text{m}$ and a C2 over-focus value $z_f$ of 11 $\mu\text{m}$ . ....	81
Figure 43: Diagram, showing the experimentally observed azimuthal rotation angles of EVB.....	82
Figure 44: Excerpt of a z-shift series showing the z-shift region where the peculiar rotations are expected to occur.....	83
Figure 45: Z-shift series of a vortex rotation experiment, exhibiting the predicted LS behaviour .....	84
Figure 46: Images of a single vortex order visualizing the still standing EVB LS for $\sigma \cdot m < 0$ .....	86
Figure 47: Images of the $m = +3$ vortex order of the same experiment as in Figure 46. ....	87
Figure 48: Diagram, showing the measured azimuthal rotation angles of Figure 46 and Figure 47 ...	88
Figure 49: Shows a scatter plot, depicting the measured slopes and their estimated error for different vortex orders $m$ for z-shift values “far” off ( $>100 \mu\text{m}$ ) the focal region. ....	89
Figure 50: Same as Figure 49, but for z-shift values in close vicinity to the focus ( $ z  < 100 \mu\text{m}$ ) .....	90
Figure 51: Excerpt of a z-shift series ranging from -300 $\mu\text{m}$ to +300 $\mu\text{m}$ , using a wave mechanical simulation of the vortex rotation experiment .....	91
Figure 52: Shows the measured azimuthal angles of the simulated data in Figure 51 .....	92
Figure 53: Gamma expanded z-shift series of a single cut vortex order $m = +3$ , simulated .....	93
Figure 54: Shows the measured azimuthal angles of Figure 53.....	94
Figure 55: Ray tracing simulation, showing the electron distribution .....	95
Figure 56: Numerically extracted azimuthal rotation angles of the simulated electron trajectories..	97
Figure 57: Real space map of the ring-like electron distribution 0.2 m in front of the quadrupole....	98
Figure 58: Left: Reciprocal space map of the output beam where only LF equations were used.....	99
Figure 59: Reciprocal space map of the simulated electrons after their flight through the quadrupole with the spin simulation switched on .....	100
Figure 60: ES evolution in units of the Bohr magneton over the course of the quadrupole .....	100
Figure 61: Modulus of the transverse velocity components after the passage of the quadrupole	

plotted over the initial azimuthal angle $\varphi_0$ .....	101
Figure 62: Left: The difference between the initial azimuthal angle and the final one.....	102
Figure 63: Reciprocal space map after passing the quadrupole for electrons carrying initial positive OAM .....	103
Figure 64: Modulus of the transverse velocity components of electrons carrying positive OAM plotted over the initial azimuth position $\varphi_0$ .....	104
Figure 65: Left: The norm of the transverse velocity components .....	105
Figure 66: Left: Longitudinal electron velocity deviations induced by the SCOFF model .....	106
Figure 67: Left: Zoom in of the reciprocal space map given in Figure 66 .....	106
Figure 68: Shows a graphic summing up the findings of cut-EVB rotation experiments for the whole accessible z-shift region by comparing the OAM of the two complementary vortex phenomena, rotational and irrotational vortices .....	109

## List of Tables

Table 1: Shows the general photon angular momentum balance for the STOC process. ....	47
Table 2: Lists the estimated slopes and OL field strengths with absolute and relative standard errors, as well as the $R^2$ value for various lens settings gained from Cu-grid z-shift series image rotation measurements. ....	74
Table 3: Lists the estimated slopes and OL field strengths with absolute and relative standard errors, as well as the $R^2$ value for three OL settings, acquired in z-shift series experiments with a Si-KE. ....	77
Table 4: Lists the estimated slopes with absolute and relative standard errors for the experiment shown in Figure 39 to Figure 41 and Figure 43 and z-shift regions above +130 $\mu\text{m}$ and beyond -130 $\mu\text{m}$ . ....	85
Table 5: Lists the estimated slopes with absolute and relative standard errors for the experiment shown in Figure 44 and z-shift regions $ z  > 130 \mu\text{m}$ . ....	85
Table 6: Lists the estimated slopes with absolute and relative standard errors for the experiment shown in Figure 45 and z-shift regions $ z  > 130 \mu\text{m}$ . ....	86
Table 7: Lists the estimated slopes with absolute and relative standard errors for the two experiments shown in Figure 48 in a z-shift region roughly around the magnetic beam waist. ....	88

## List of Abbreviations

APC	Azimuthal Probability Current
AV	Acceleration Voltage
CC	Counter-Clockwise (Rotation)
CW	Clockwise (Rotation)
DM3	Digital Micrograph 3
EELS	Electron Energy Loss Spectroscopy
ES	Electron Spin
EVB	Electron Vortex Beam
FIB	Focused Ion Beam
FWHM	Full Width at Half Maximum
LF	Lorentz-Force
LG	Laguerre-Gaussian
LR	Larmor-Rotation(s)
LS	Landau State(s)
OA	Optical Axis
OAM	Orbital Angular Momentum
OL	Objective Lens
OVB	Optical Vortex Beams
PP	Pole Piece
QM	Quantum Mechanics
SAM	Spin Angular Momentum
SCOFF	Sharp-Cut-Off-Fringe-Fields
SEM	Scanning Electron Microscope
(Si)-KE	(Silicon)-Knife-Edge
STEM	Scanning Transmission Electron Microscope
STOC	Spin-to-Orbit Conversion
TEM	Transmission Electron Microscope/Microscopy

## Zusammenfassung

Da es erst seit 2010 möglich ist Elektronen-Vortex-Strahlen (EVB) im Transmissionselektronenmikroskop (TEM) herzustellen, ist über deren Bewegung in magnetischen Feldern bislang noch wenig bekannt. Diese ringförmigen Elektronenstrahlen besitzen quantisierten Bahndrehimpuls (OAM), sowie ein quantisiertes magnetisches Moment. Diese Eigenschaften machen EVB besonders interessant, unter Anderem für Nanopartikelmanipulation und die Bestimmung der Ausrichtung atomarer magnetischer Momente. Weiters gibt es auch Ansätze, die EVB in einem Quadrupol-Wien-Filter zur Elektronenspin (ES) Polarisation einzusetzen.

Laut gängiger elektronenoptischer Abbildungstheorie zeigen alle Elektronen, welche das magnetische Linsenfeld in einem TEM durchlaufen, dieselbe Rotationsgeschwindigkeit, und zwar Larmor-Rotation (LR). Kürzlich wurde auf theoretischer Basis vorhergesagt, dass EVB, welche durch ein parallel zur Strahlachse ausgerichtetes homogenes magnetisches Feld propagieren, so genannten Landau-Zuständen entsprechen. Diese sollen abweichende Rotationsgeschwindigkeiten zeigen, und zwar Zyklotron- (2-fache LR), LR, sowie keine Rotation.

Das Ziel dieser Arbeit war es, die Propagation von EVB im Magnetfeld der TEM Objektivlinse experimentell, sowie theoretisch zu untersuchen. Dazu wurden numerische Simulationen durchgeführt, die die Bahn der Elektronen mithilfe der Lorentzkraft und realistischen Parametern für das Linsenfeld berechnen. Selbige Simulation wurde auch für die Betrachtung des, obig erwähnten, Quadrupol-ES-Polarisators angepasst. Überdies wurde ein semiklassisches Model eingeführt, sowie die Ergebnisse von wellenmechanischen Simulationen zum Vergleich herangezogen.

Die experimentellen Ergebnisse zeigen ein komplexes Rotationsverhalten von EVB in magnetischen Feldern, welches stark von der radialen Ausdehnung der betrachteten EVB abhängt. Ist deren Radius wesentlich größer als die so genannte magnetische Strahlweite, zeigt sich, unabhängig vom OAM des EVB, ausschließlich LR. Erreicht der Strahlradius jedoch die Größenordnung der magnetischen Strahlweite, zeigen sich, abhängig vom OAM und der Ausrichtung des Magnetfeldes, drei verschiedene Rotationsgeschwindigkeiten (0, LR, 2LR). Diese Beobachtung deckt sich mit der theoretischen Vorhersage der Landau Zustände.

Das Verhalten des untersuchten Quadrupol-ES-Polarisators konnte bestätigt werden. Jedoch verschwand dieser ES polarisierende Effekt unter Miteinbeziehung eines einfachen Streufeldmodells.



## Abstract

Since it became possible to create electron vortex beams (EVB) in transmission electron microscopes (TEM) in 2010, it has been very important to understand their motion, in particular in the magnetic lens fields in a TEM. These doughnut shaped beams carry quantized orbital angular momentum (OAM) as well as a quantized magnetic moment. These properties render them attractive for applications like particle manipulation and mapping magnetic moments on the atomic scale. Additionally there have been proposals to employ EVB in an electron spin (ES) polarizing quadrupole-Wien-filter.

Standard electron imaging theory predicts that all electrons traversing the magnetic lens field in a TEM rotate with the same angular speed, which is the Larmor-frequency. Recently, it has been argued that EVB propagating through uniform magnetic fields parallel to the beam axis represent so called Landau states, which should show peculiar rotations, including no-, Larmor- (LR) and cyclotron (double-Larmor) azimuthal rotations.

The aim of this work was to experimentally, as well as theoretically investigate EVB propagation within the magnetic field of the TEM objective lens (OL). An additional goal was to simulate the above mentioned quadrupole-ES-polarizer.

Numerical ray tracing calculations using the classical Lorentz force were performed using realistic parameters for the OL field. Additionally a semi-classical model was introduced, as well as results of wave-mechanical simulations were compared with the experiments. The numerical ray tracing code was also adapted to investigate the proposed quadrupole-ES-polarizer.

It could be shown that EVB exhibit a complex rotational behaviour in magnetic fields that strongly depends on their radial extension. Electron beams with a diameter that is much larger than a field specific length parameter, called magnetic beam waist, show only LR, independent of their OAM. In contrast to that, peculiar EVB rotations (0, LR, 2LR), depending on their OAM and orientation of the magnetic field, have been observed for electron beams with a radial extension of the order of the magnetic beam waist. This is in accordance with the theoretical predicted Landau states.

The ES-polarizing effect of the simulated quadrupole could be confirmed. However, the ES-polarizing effect vanishes, when taking into account a simple fringe field model.

## Acknowledgements

At this point I want to take the chance to express my gratitude towards all the people around me who endorsed me on the way to and in the course of this work or contributed in any other way to finalize this humble attempt to understand a bit more of our physical universe.

At first I have to thank my kind and open minded supervisor Peter Schattschneider for introducing me to the “strange sparks from the vacuum”, (Schattschneider, Schachinger et al. submitted), electron vortices, and the idea to the experiment given herein to unravel their rotational dynamics. His patience and motivation seem to be the right recipe. Especially giving me the chance to present this work at conferences was very enlightening. As with him, I had many fruitful discussions with Stefan Löffler, whom I want to thank, too, very much, not only for discussing, but for all other kinds of troubleshooting. Additionally I want to thank Michael Stöger-Pollach for his experimental expertise with TEMs, Andreas Steiger-Thirfield for producing fine holographic vortex masks with the focused ion beam machine, Jakob Gruber and Thomas Gamerith for helping me preparing the knife edge as well as Isabella Floss for providing some wave-mechanical simulations of the experiment. I also appreciate Konstantin Bliokh’s help with the manuscript for publishing some of the findings contained herein.

I also appreciate the financial support of the Austrian Science Fund (FWF) Grant Nr.: I543-N20, the Vienna University of Technology, especially the Institute for Solid State Physics and the Austrian Society for Electron Microscopy (ASEM).

Moreover it was my wonderful wife Marie-Luise who not only blessed me with two lovely kids but also took great care of them such that I could concentrate on the “minor” things of life. Particularly in the last weeks getting this work done demanded a lot of patience and stamina, I really want to thank her for that. And even little Leopold and Joseph contributed by bringing me back to earth. Just like my best friend Martin Schnabl who also assisted me at the last experiment. And last but not least, I want to thank my parents Elfriede and Franz for their faithful support all the way up to now.

“We know nothing. This is the first. Therefore we should be very modest. This is the second. And not to claim “we know”, when we don’t know. That is the third. That is the attitude I’d like to popularize. There is little hope to success”, Karl Popper.

## 1 Introduction

The aim of this work is to deepen our understanding of the electron vortex beams' (EVB) propagation through magnetic fields, in particular in the objective lens field of a transmission electron microscope (TEM), and in a quadrupole Wien filter.

In fluid dynamics a vortex is characterised by the spinning motion of the fluid constituents around a common centre. Particles within such a vortex follow a closed loop. When this vortex is moving through space, the closed loop movement opens up, so that the particles follow helical trajectories (Demtröder 2005a), see Figure 1, left.

A vortex beam can be described by transferring this intuitive picture to electromagnetic waves. There, it is the Poynting vector describing the directional energy flux per time going through a unit area, which represents the helical motion of aforementioned spinning particles. This helical Poynting vector is generated by a wavefront that is spiralling around a so called phase singularity, see Figure 1, right.

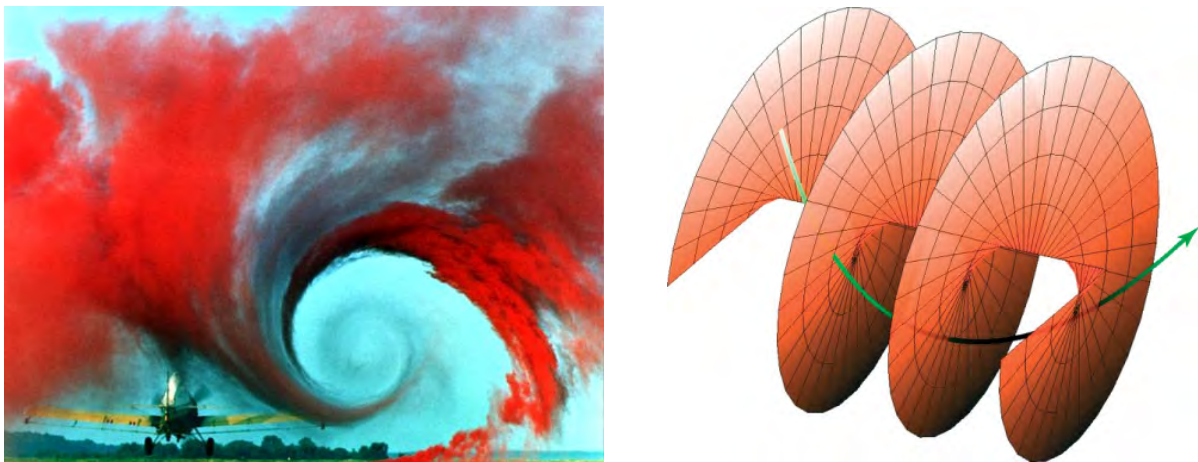


Figure 1: Left: Vortex motion in air induced by an airplanes' wing tip (NASA 1990). Right: Helical wavefront with associated helical Poynting vector (Torres and Torner 2011).

First signs of these electromagnetic, photonic or optical vortex beams (OVB) could have already been observed in the 1950s (Findlay 1951). But at that time there was no theory describing these observations, so that their significance was underestimated. The same holds for the creation of helical spiralling electron beams in the 1970s by Beck, Mills and Munro. To create millimetre wave radiation, their idea to structure the electron beam instead of the microwave cavity, led them to the

early realization of EVB. They were incorporating an annular electron gun, immersed in a strong magnetic field. A subsequently following magnetic jump, where the field rapidly reversed sign over a few millimetres spatial distance produced annular electron beams, carrying high amounts of angular momentum (Beck and Mills 1971, Mills 1971, Munro 1971, Beck and Mills 1973). At that time, Nye and Berry were trying to understand radio echoes from the bottom of the Antarctic ice sheet, and came up with the first theoretical description of vortex beams (Nye and Berry 1974). By choosing the title “Dislocations in wave trains”, they already pointed out that wavefronts, just as crystals can show dislocation lines. Presumably Beck and his co-workers were not aware of this work, which also accounted for the underestimation of their discovery of EVB. Nearly twenty years later, OVB have been created experimentally for the first time (Bazhenov, Vasnetsov et al. 1990), and two years later (Heckenberg, McDuff et al. 1992). Since then, there has been a growing interest in “twisted” photon beams, with an increasing number of applications, such as optical tweezers exerting torque on microscopic particles (He, Friese et al. 1995), as well as optical micro motors (Knöner, Parkin et al. 2007), cooling mechanisms (Kuppens, Rauner et al. 1998), aberration correction in optical systems (Jesacher, Schwaighofer et al. 2007), encoding information in the radio frequency domain (Tamburini, Mari et al. 2011), trapping of Bose-Einstein condensates (Bongs, Burger et al. 2001), improving the resolution of optical microscopy beyond the diffraction limit (Rittweger, Han et al. 2009), and the detection of exoplanets (Serabyn, Mawet et al. 2010). Even hard x-ray OVB have recently been produced by using a free-electron-laser (Hemsing, Knyazik et al. 2013).

Additional sources and further information on OVB can be found in the two review articles “Advances in optical angular momentum” and “Tweezers with a twist” (Franke-Arnold, Allen et al. 2008, Padgett and Bowman 2011).

Exactly twenty years after Bazhenov and his group created optical vortices, and nearly forty years after Beck and his colleagues already used spiralling electron beams to build microwave generators, Uchida and co-workers used a stack of graphite thin films to imitate a screw dislocation, which, illuminated with a parallel electron beam, (re-)created electron beams carrying a (fork-) dislocation. This was holographically proven using a Möllenstedt biprism (Uchida and Tonomura 2010).

Although this was an impressive proof of principle, there were several drawbacks limiting the applicability of the aforementioned technique. For instance, it is a tedious procedure to prepare and find proper regions on the graphite thin films strongly reducing the reproducibility. Moreover, such thin film structures suffer rapidly from beam damage and contamination. Additionally, there is a significant loss of intensity due to high angle scattering and absorption in the thin films.

Most of these disadvantages were overcome shortly after Uchidas' and collaborators' observations by transposing the method of using computer-generated holograms to create OVB to the field of accelerated particle physics (Verbeeck, Tian et al. 2010a). Since then, it has been routinely possible to produce free electron beams, carrying high amounts of angular momentum, up to  $100 \hbar$  (McMorran, Agrawal et al. 2011). To clearly distinguish the spin angular momentum of electronic and photonic beams, the angular momentum of vortex beams was coined orbital angular momentum (OAM). Using holographic vortex masks turned out to be a very robust and replicable technique, albeit the intensity problem still remained. The mask itself blocks half of the incoming beam electrons, 50 % of the other half are distributed to the central beam carrying no OAM, such that only 12.5 % or one eighth of the incoming electrons are in an OAM state, carrying OAM of  $\pm \hbar$ . In reality it is even less, because some of the electrons are diffracted to higher OAM orders, due to the binary grating structure (Verbeeck, Tian et al. 2010b). Ideas and experimental evidence, to overcome this shortcoming using Zernike phase plates and the TEM's astigmatism have been presented recently (Schattschneider, Stöger-Pollach et al. 2012b). Additionally, it has been shown that the phase structure of the electron beam can be manipulated to create EVB using a probe corrector (Clark, Béch e et al. 2013) or magnetic monopole like magnetized nanoscale needles, placed in the centre of an aperture (B ech e, Boxem et al. 2013).

In contrast to optical vortices, EVB do carry a quantized magnetic moment, even without spin polarization. This is a result of their spiralling electron current. Even though the possibility to use EVB for mapping magnetic moments on the mesoscale has been ruled out (Schattschneider, L offler et al. 2012, Rusz and Bhowmick 2013), they can be focused to atomic size (Schattschneider, St oger-Pollach et al. 2012a), thus opening the road for future applications like mapping magnetic moments on the atomic scale (Schattschneider, Verbeeck et al. 2010, Rusz and Bhowmick 2013) and particle manipulation (Verbeeck, Tian et al. 2013). It could also be envisioned, that due to their significantly reduced diffusion when centred on atomic columns, electron vortices will further improve the atomic resolution of STEM-EELS techniques (L offler and Schattschneider 2012, Xin and Zheng 2012, Lubk, Clark et al. 2013).

Despite their promising future for a variety of applications, the field of electron vortex research just departed from their discovery, so that some fundamental questions are still waiting to be resolved. Concerning their future application to map magnetic moments, one of the fundamental questions is their propagation dynamics in magnetic fields. In the absence of such, electron vortices would practically behave like their "bosonic twins" the OVB (Gallatin and McMorran 2012), but due to the electrons charge there should be an interaction with magnetic fields, in particular with the magnetic

lens fields in a TEM.

Firstly, Gallatin, Bliokh and their co-workers theoretically predicted such interactions (Bliokh, Schattschneider et al. 2012, Gallatin and McMorran 2012). Bliokh and his co-workers stated that these interactions show up in the form of peculiar rotations of EVB in uniform magnetic fields parallel to the beam axis, which would be in contrast to standard imaging theory, predicting the same rotational speeds for all objects traversing the TEM lens field.

And secondly, Karimi and co-workers proposed a device able to convert an incoming EVB to an (at least partly) spin polarized one, and vice versa by the use of a quadrupole Wien filter (Karimi, Marrucci et al. 2012b).

Therefore this thesis will be split into two main parts, the more extensive first part on the experimental observations of electron vortices' rotational behaviour in the magnetic lens field of a TEM. Testing the predictions of Bliokh and his co-workers, and a more concise second part that will review Karimis' and co-workers' proposals concerning electron spin (ES) polarisation by a process called spin-to-orbital angular momentum conversion (STOC). This will be done using a ray tracing numerical simulation code employing the classical Lorentz force. In order to include the ES interaction, the same force that described the Stern-Gerlach effect will be introduced. The temporal evolution of the ES will be accounted for by the precession equation. It should be noted that this ansatz is commonly used in analysing and building electron-optical elements for electron microscopy, because quantum mechanical effects, like diffraction, are only relevant for looking at the close vicinity of the focal point.

## 2 Theoretical Background

This chapter is meant to give the reader a sufficient theoretical background to understand the scope and implications of the work done.

The first part will start with a general introduction to the TEM, and then it is necessary to look a bit closer to the objective lens and the image formation. After that, the recently discovered EVB will be covered in more detail, so that the following theoretical predictions from Bliokh and his co-workers appear in a more intuitive way.

The second part will introduce an alternative way to create OVB incorporating the photon spin as well as the proposals from Karimi and his colleagues to transfer this new technique to electron microscopy, using a “space-variant Wien filter”.

### 2.1 Peculiar Electron Vortex Beam Rotations

#### 2.1.1 The Transmission Electron Microscope

The deep seated motivation to explore and determine nature’s (organic and inorganic) building blocks to ever decreasing length scales, led to the development of the first transmission electron microscopes by R. Rüdénberg, E. Ruska and B. v. Borries in 1931 (Rüdénberg 1943, Calbick 1944, Glaser 1952). To improve the resolution power of microscopes beyond the optical diffraction limit, which is of the order of the used light wavelength (approx. 500 nm), their idea of building an “Übermikroskop”, primary based on the discovery of the lightest and smallest fundamental particle by J. J. Thompson, about three and a half decades before, the electron. In their view the electron had a classical electron radius of the order of a few femtometers. Furthermore J. J. Thompson used an apparatus which deflected and focused cathode rays in an evacuated tube to reveal that electrons constitute cathode rays. The further improvement of this principle plus the derivation of the lens maker’s equation for electrons in electromagnetic fields, stemming from the “father” of electron optics H. Busch (Busch 1926), paved the way for inventing the TEM.

Apart from their low radius/wavelength which predestined electrons for high resolution imaging there are a few other advantages. They are the lightest most abundant stable fundamental particles showing therefore nearly no inertia and together with their electric charge they can be easily accelerated, guided and deflected by electromagnetic fields. Also they can be simply



extracted out of metal surfaces, and vanish again after detection without contamination. And due to their strong interaction with solids, only small volumes of sample material are needed, < 1 mm in diameter and a sample thicknesses of a few tens of nm (Glaser 1952, Schattschneider, Stöger-Pollach et al. 2011).

Despite these benefits, electron optics strongly suffer from undesired image distortions, so called aberrations. Most important are the chromatic - as well as the spherical aberrations because they lower the attainable resolution significantly, so that much effort went into their understanding and correction in the last decades (Haider, Uhlemann et al. 1998, Freitag, Kujawa et al. 2005).

These efforts paid off and brought the TEM technique as far as visualizing even the lightest building blocks of matter, like carbon and hydrogen (Meyer, Girit et al. 2008) and being able to resolve atomic structures down to 47 pm in a Ge  $\langle 114 \rangle$  crystal (Erni, Rossell et al. 2009).

Up to 1972 TEMs were produced equipped with magnetic- and/or electrostatic condenser/objective/projective lenses, but from then on only the magnetic systems were pushed forward, owing to the higher focusing strength of magnetic lenses and some engineering problems (which could be solved nowadays) with electrostatic lenses, like high voltage breakdown and easy contamination. Nevertheless electrostatic TEMs had also a few very promising properties like their very low power consumption and compact size (Orloff 1997).

The main parts and basic function of a TEM, see Figure 2, can be described quite well by simply following the path of a swarm or bundle of electrons through the microscope, starting with their “birth” (mostly) at the top of TEM. There, one can find the electron source, represented by a sharp metal tip, which emits electrons using thermionic- or field emission effects on its surface, see Figure 2, right. The type of emission determines the energy width (monochromaticity), which is typically of the order of 1 – 3 eV for thermionic- and 0.3 - 0.8 eV for field emission sources. The diameter of the tip or rather the size of the electron emitting region on it is crucial in order to get fine focused spots and high spatial coherence. A representative value for the quality of an electron source is given by the brightness that is how much current per surface area is emitted into a certain solid angle. For thermionic sources it is  $\sim 10^{10} \text{ Am}^{-2}\text{sr}^{-1}$ , and for field emission devices  $\sim 10^{13} \text{ Am}^{-2}\text{sr}^{-1}$ . To prevent electron collisions with gas molecules as well as the generation of arcs between the cathode and the anode, the column must be evacuated to  $10^{-4} \text{ Pa}$  and the region around the source to  $10^{-7} - 10^{-9} \text{ Pa}$ , depending on the type of source. After the electrons are extracted, they get accelerated by electrostatic fields, typical acceleration voltages (AV) are 60 - 300 kV. E.g. biological samples suffer more from beam damage, thus the AV has to be reduced. The electrons travel with 70 % of the velocity of light (at 200 kV AV) down the column, where several beam adjusting

deflection plates apply transverse electric fields to align their path to the optical axis (OA) before they enter the first magnetic lenses. These two to three beam forming lenses are called the condenser system, and, depending on the experimental setup, form a parallel beam for standard TEM imaging or a convergent beam, with a spot size typically of the order of  $2 \text{ \AA}$  (down to  $0.5 \text{ \AA}$  (Dellby, Bacon et al. 2011)), for e.g. scanning TEM.

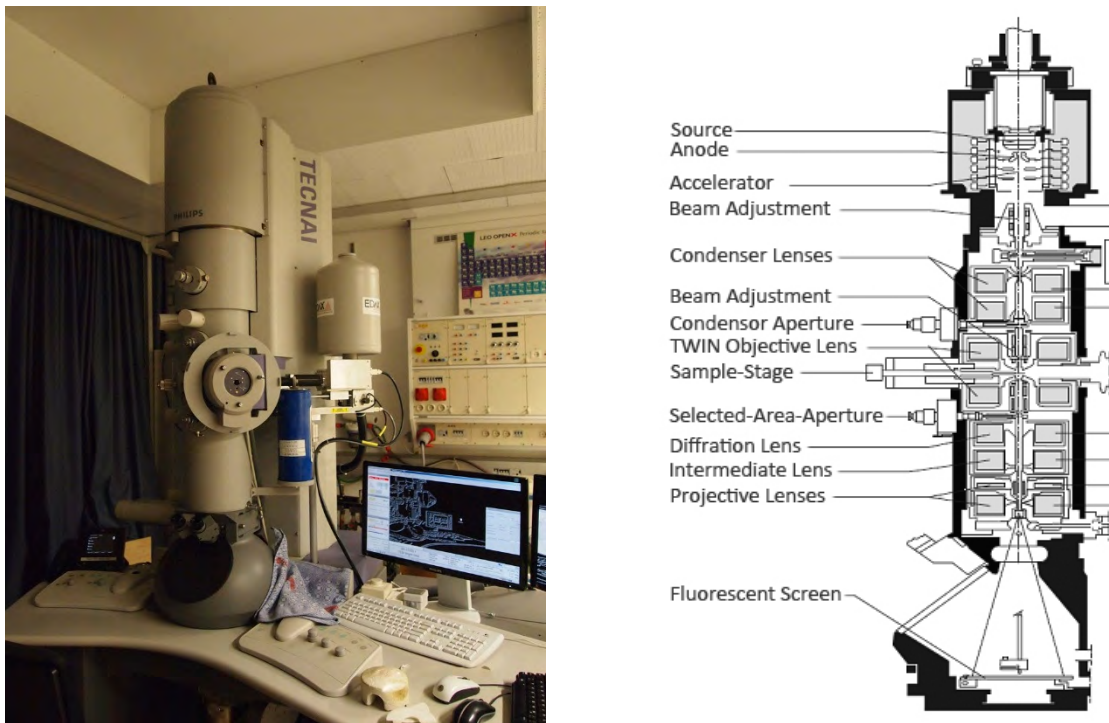


Figure 2: Left: Picture of the Philips/FEI Tecnai G2 F20 TEM at the TU-Vienna. Right: Schematic cross section of a comparable Philips CM 200 TEM, taken from (Bergmann and Schäfer 2004).

At the exit of the condenser system the bundle of electrons gets partly blocked by the beam forming- or condenser aperture/diaphragm that enables the user to balance the illumination between intensity and spatial coherence. Subsequently the most important lens for image formation is deflecting the electrons, the objective lens (OL). Here approximately at the so called eucentric height of the sample-stage, and at the same time in the front focal- or object-plane of the OL, the electrons meet with the object of interest; the  $\sim 10$  - $300 \text{ nm}$  thick specimen. Due to their strong interaction with matter they get deflected according to their incident position relative to the atomic/crystal potential, see for example the authors project work (Schachinger 2012). The specimen is mounted on a  $\sim 3 \text{ mm}$  in diameter ring in the sample-stage, which can be manipulated on the nanometre scale in  $x,y,z$ -direction and tilted  $\sim \pm 40^\circ$  in two directions, depending on the OL design. The eucentric height, defined as the stage (goniometer) tilting axis, marks the very  $z$ -

position, where the microscope calibration is valid; this is why bringing the sample to this position is a very fundamental thing in electron microscopy. If the sample is in the eucentric height, tilting it does not change its lateral position. About 3 mm further down the column in the backfocal- or image-plane of the OL, the electron swarm is limited by the contrast aperture, which can be used to enhance image contrast. In order to obtain also diffractograms of the specimen, the TEM operator can switch on and off the diffraction lens. This lens has got an own aperture, called selected area diffraction aperture, which is below the OL. The task of the following set of magnetic lenses, which consist of the intermediate- and projective lenses, is to magnify the image of the specimen, made with the OL, more than a million times. And finally, after about two meters of flight or 10 ns, the electrons land, one after another, on a fluorescent (zinc sulfide) screen, making the normally invisible electrons visible to the eye by a greenish light. Alternatively this screen can be lifted, so that the electrons can reach the charge coupled device (CCD), to collect intensity maps pictures. In modern instruments, the fluorescent screen is completely removed by the before mentioned charge coupled device, such that the whole microscope can be fully encapsulated and shielded to reach higher vibrational and thermal stability. Interestingly, owing to the low beam currents of the order of pA to nA in combination with the high AV, there is only one to a hand full electrons in the whole microscope present at the same time, justifying the “one after another” model, such that the so called Boersch effect, describing electron-electron repulsion inside electron beams, can be safely neglected (Glaser 1952, Bergmann and Schäfer 2004, Schattschneider, Stöger-Pollach et al. 2011).

### 2.1.2 TEM Objective Lens

In the preceding section we have seen, that the only magnetic field accessible by the sample stage is the one of the OL field, therefore it should be described in more detail in this section, following (Glaser 1952, Williams and Carter 1996, Orloff 1997)

The magnetic OL of a TEM is formed by the rotational symmetric magnetic field within the gap of the pole piece (PP), depicted in Figure 3, left. The magnetic flux is generated by a current flow through insulated wire coils, which are positioned inside a ferromagnetic (soft magnetic) cylindrical yoke, see Figure 3, right. A thermal distributor plate and additional cooling pipes for water cooling, guarantee an effective heat dissipation of the resistive losses of the copper windings, and therefore high mechanical and electrical stability. The magnetic flux is channelled through the yoke, the directly attached poles and subsequently, through the PP set onto the pole. They consist of a soft magnetic material such as iron, iron-cobalt - or a nickel-cobalt alloy, exhibiting a high permeability.

The electron beam traverses the OL through a 3 mm bore in the PPs. Generally the whole PP has to be machined with very high precision to reduce deviations from the rotational symmetry, as they would introduce image distortions like astigmatism. Now, the magnetic flux lines leave the PP and spread into the typical 3 to 10 mm wide gap (s) in between the PPs. These rotational symmetric “stray fields” represent a convex electron- or round lens, which means electrons entering the OL at a certain radial distance to the OA are always bent towards the OA, no matter which direction the current is sent through the insulated wire coils. Such round lenses always show aberrations as long there are no space charges involved and the lens field is static, according to Scherzers’ Theorem (Scherzer 1936). To correct these aberrations, multipole fields have been used successfully (Haider, Uhlemann et al. 1998).

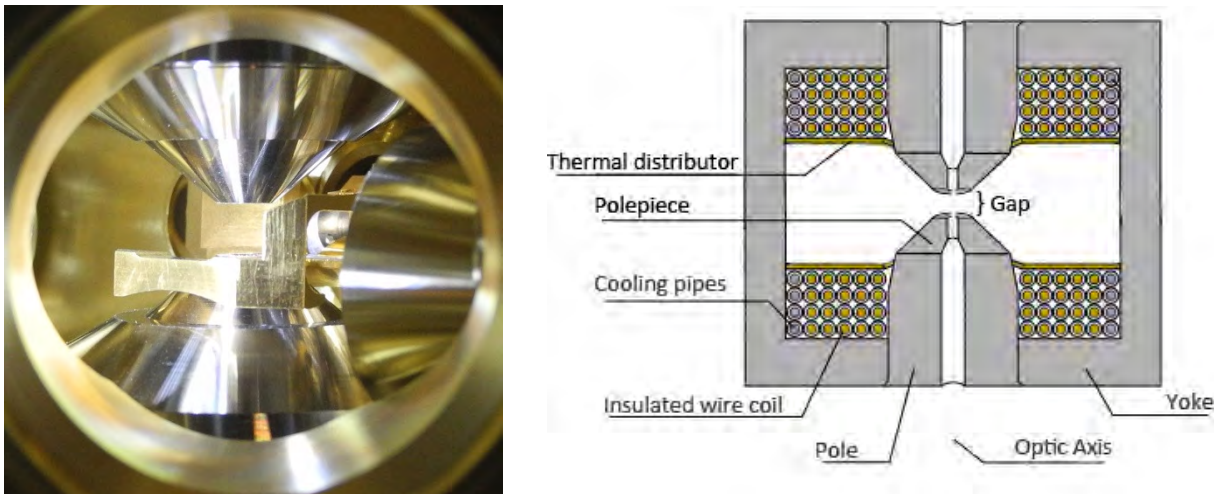


Figure 3: Left: Side-view picture of the objective pole piece of a FEI Tecnai F20 and the brass cooling finger. Right: Schematic drawing of a magnetic lens, adapted by the author, original by (Hat'nCoat 2009).

A great deal of theoretical work, including the mathematical description of these OL stray fields and calculation of electron trajectories passing such magnetic lenses, has been done by Walter Glaser in the 1950s. This is why the characteristic bell shaped magnetic field of such electron lenses is called Glaser’s “Glockenfeld”. Its z-component obeys the relation,

$$B_z(z) = \frac{B_0}{1 + \left(\frac{z}{d}\right)^2}, \quad (2.1)$$

where  $B_0$  represents the maximum field intensity at the position  $z = 0$  (the lens centre) and  $2d$  represents the full width at half maximum (FWHM) of the field distributions’ z-component. The radial component of the OL field can be obtained using the solenoidality of the magnetic field,

which is the absence of magnetic sources, in its integral form  $\oint \vec{B} d\vec{A} = 0$ .

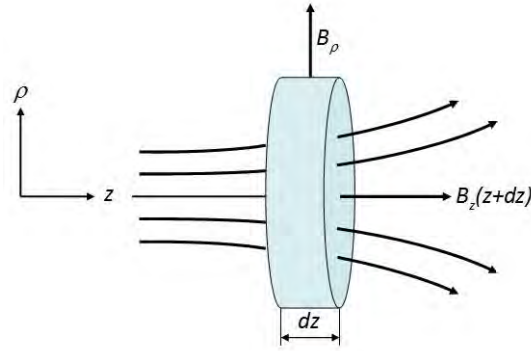


Figure 4: Illustrates the "Pillendose" for the calculation of the radial component of rotational symmetric magnetic fields.

Calculating this integral for the volume element ("Pillendose") shown in Figure 4 gives the expression  $2\pi \cdot \rho \cdot dz \cdot B_\rho + \pi \cdot \rho^2 \cdot B_z(z+dz) - \pi \cdot \rho^2 \cdot B_z(z) = 0$ , where the series expansion

$B_z(z+dz) \approx B_z(z) + \frac{dB_z}{dz} \cdot dz$  has been used to get the following expression,

$$B_\rho = -\frac{\rho}{2} \cdot \frac{\partial B_z}{\partial z}. \quad (2.2)$$

This only holds for paraxial electron trajectories, where  $B_z$  does not change significantly over the radial distance. And finally the azimuthal component  $B_\phi$  is zero due to its rotational symmetry. Important parameters introduced to describe the strength of an electron optical lens are  $\omega$  and  $k^2$ , which should not be confused with the later on used parameters describing the angular frequencies and wave vectors.  $\omega$  and  $k^2$  are defined as,

$$\omega = \sqrt{1 + k^2}, \quad (2.3)$$

and  $k^2$ , being,

$$k^2 = \frac{e}{8m_e} \cdot \frac{B_0^2 \cdot d^2}{U^*}. \quad (2.4)$$

$k^2$  connects characteristic parameters defining an electron lens, that are the maximum magnetic field strength in z-direction at the centre of the OL  $B_0$ , the half FWHM of the lens field  $d$  and the "Ersatzspannung"  $U^*$ , which is related to the AV  $U$  like,

$$U^* = U \cdot \left( 1 + \frac{e}{2 \cdot m_e \cdot c^2} \cdot U \right), \quad (2.5)$$

and stems from relativistic effects, as well as the elementary charge  $e$  and the electrons invariant

mass  $m_e$ . Figure 5 shows on the one hand the bell shaped magnetic field of above described PP according to equation (2.1), and on the other, seven trajectories of electrons traversing such a “Glaser-Glockenfeld” for various  $\omega$  ranging from 1.1 to 3.5.

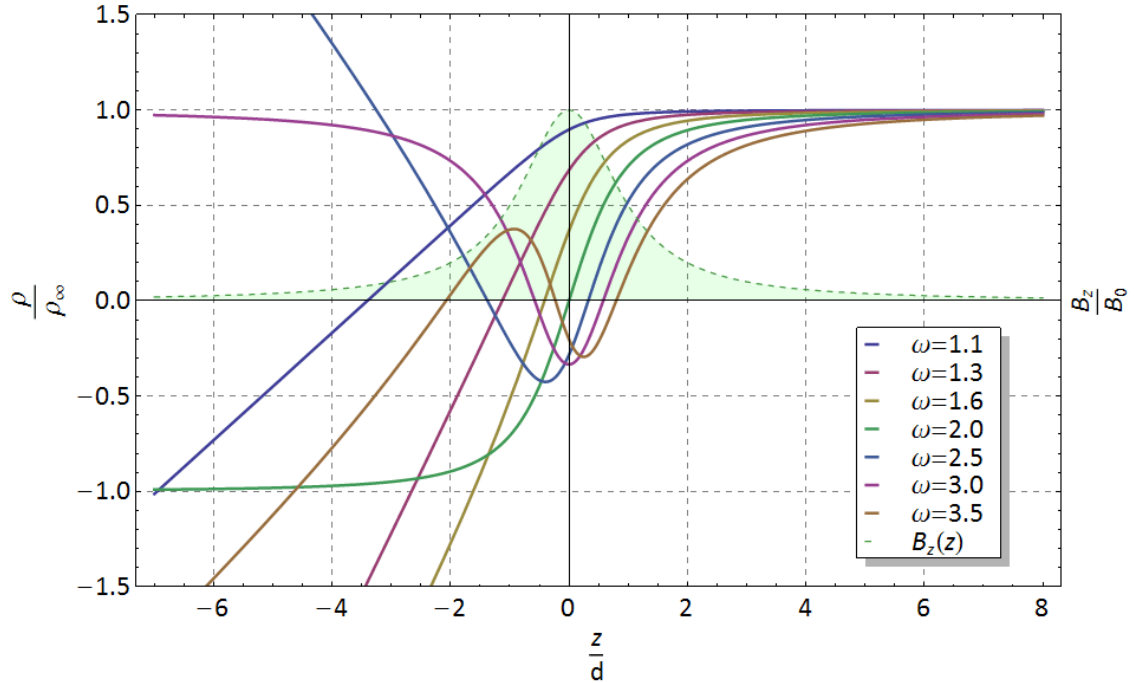


Figure 5: Course of some electron paths incident from the right hand side parallel to the OA, being deflected by a bell-shaped magnetic field (“Glaser-Glockenfeld”), dashed line, for various lens strengths  $\omega$ , solid lines.

It can be proved that the OL shows lowest focal distance as well as highest refraction power, and therefore highest magnification values, which is the ratio between the size of an object and its image, for a lens with the strength  $k^2 = 3$ . This is why modern OL, also the S-Twin lens of FEI, work at and around this  $k^2$  value. The electron path for this  $k^2$  value is shown in Figure 5 with a  $\omega$  value of two, where it can be seen that an incoming parallel beam is focused to the OL centre. It turns out, that the lowest achievable focal distance is equal to half the FWHM of the OL field  $d$ . To find out  $d$ , reforming of equation (2.4) leads to the following expression,

$$d = \sqrt{\frac{8m_e}{e} \cdot \frac{\sqrt{U^*}}{B_0}} \cdot k. \quad (2.6)$$

Using the known values from the Tecnai F20 S-Twin OL,  $B_0$  equals approximately 1.9 T (Tiemeijer 2013, Zweck 2013) and  $U^* = 239$  kV,  $2d$  equals 6.02 mm, which is about 12 % more than the known value for the gap width of 5.4 mm (FEI 2013). Measurements of the lens field have shown that the larger the bore diameter  $b$  and the smaller the gap  $s$  of a PP is chosen, the more difference

between  $d$  and  $s$  is observed, e.g. for  $b = 10$  mm and  $s = 3$  mm the  $2d$  value is more than 200 % larger than  $s$ , for  $b = 5$  mm and  $s = 5$  mm,  $2d$  is only 16 % larger than  $s$ , see (Glaser 1952), page: 185. As the bore diameter  $b$  equals 3 mm for the S-Twin OL the result for  $2d$  being 12 % larger than  $s$  is quite reasonable. Thus this value will be chosen for further considerations and simulations. Note that  $\omega$  and  $k$  will be used to describe angular frequencies, respectively, wavevectors, outside this section.

### 2.1.3 Standard Image Rotation in TEM – Larmor-Rotation

This section will cover the aspect of electron optics employing magnetic lens, just as the one described above, that the generated image of an object is rotated by a certain azimuth angle with the centre of rotation being the OA, as well as that the rotational speed depends on the magnetic field strength. This aspect is called image- or Larmor-Rotation (LR), see Figure 6.

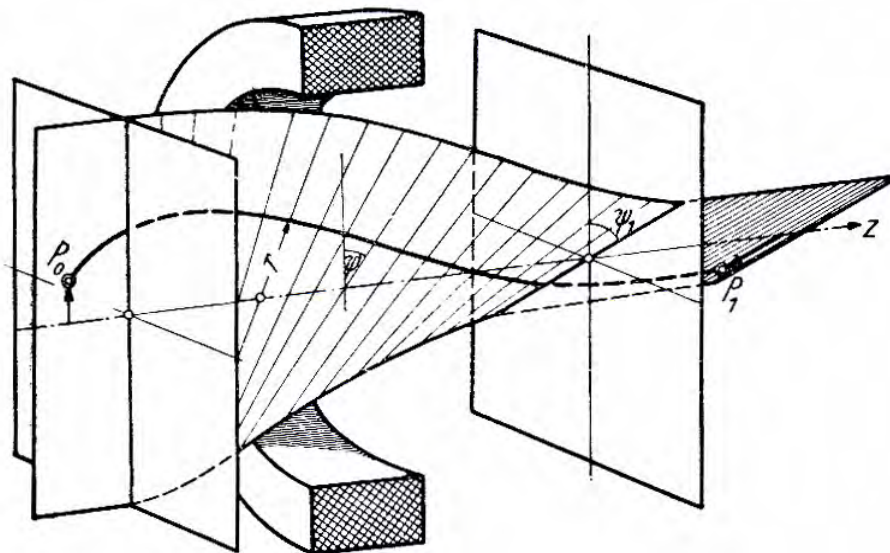


Figure 6: Electron optical imaging through a rotational symmetric magnetic field, induced by the solenoid magnet in the centre of the sketch. The electron paths evolving from point  $P_0$  lie on helicoids with variable pitch (Glaser 1952).

Quantitatively, to derive an expression for the LR, it is favourably to start with the electron velocities in the cylindrical coordinate system  $(\rho, \varphi, z)$ ,

$$v_\rho = \dot{\rho} \qquad v_\varphi = \rho \cdot \dot{\varphi} \qquad v_z = \dot{z},$$

with  $\rho$  being the radial distance of the electron path to the OA,  $\varphi$  being the azimuth angle and  $z$  the projected position on the OA, see Figure 7. This derivation follows the one in (Glaser 1952). To set up the expressions for electron movement in the radial-, azimuth- and  $z$ -direction, the Lorentz-Force (LF) has to be applied. That is, acting on an electron in the magnetic lens field  $\vec{B}$ ,

$$\mathbf{F}_L = q \cdot (\mathbf{v} \times \mathbf{B}), \quad (2.7)$$

where  $q$  is the elementary charge  $-e$  and  $\mathbf{v}$  the electron velocity.

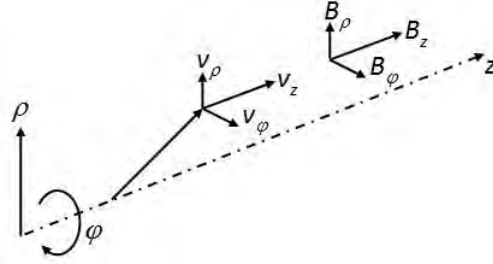


Figure 7: Drawing, showing the used cylindrical coordinate system for the electrons motion, as well as the magnetic field components.

This leads to the following expression for the radial electron motion, when additionally taking into account that a nonzero azimuth velocity introduces an outward directed centrifugal force  $\mathbf{F}_c$ ,

$$F_\rho = F_{L,\rho} + F_c = m_e \cdot \ddot{\rho} = -e \cdot \rho \cdot \dot{\varphi} \cdot B_z + m_e \cdot \rho \cdot \dot{\varphi}^2. \quad (2.8)$$

For the azimuth motion, Euler's law of angular momentum  $\frac{d\mathbf{L}}{dt} = \mathbf{M} = \rho \cdot F_\varphi$  is incorporated. Where

$L_z = m_e \cdot \rho \cdot v_\varphi = m_e \cdot \rho^2 \cdot \dot{\varphi}$  is the electrons angular momentum and  $\mathbf{M}$  represents the torque acting on the electron, being equal to the product of the electrons radial distance to the OA and the azimuthal component of the LF,  $F_\varphi = -e \cdot (\dot{z} \cdot B_\rho - \dot{\rho} \cdot B_z)$ . Thus one can write,

$$\frac{d}{dt}(m_e \cdot \rho^2 \cdot \dot{\varphi}) = e \cdot \rho \cdot \dot{\rho} \cdot B_z - e \cdot \rho \cdot \dot{z} \cdot B_\rho. \quad (2.9)$$

For the longitudinal electron motion, the LF gives,

$$F_z = e \cdot B_\rho \cdot \rho \cdot \dot{\varphi}. \quad (2.10)$$

Now, the expression (2.2) for the radial field component  $B_\rho$  is put in equations (2.9) and (2.10)

which then read,

$$\frac{d}{dt}(m_e \cdot \rho^2 \cdot \dot{\varphi}) = e \cdot \rho \cdot \dot{\rho} \cdot B_z + e \cdot \frac{\rho^2}{2} \cdot \frac{\partial B_z}{\partial z} \cdot \dot{z} = \frac{d}{dt} \left( \frac{e}{2} \cdot \rho^2 \cdot B_z \right), \quad (2.11)$$

$$F_z = -\frac{e}{2} \cdot \rho^2 \cdot \frac{\partial B_z}{\partial z} \cdot \dot{\varphi}. \quad (2.12)$$

Where in (2.11)  $\dot{z} = \frac{dz}{dt}$  was used to simplify the equation. In this form it can be directly integrated,

$$m_e \cdot \rho^2 \cdot \dot{\varphi} = \frac{e}{2} \cdot \rho^2 \cdot B_z + C, \quad (2.13)$$



and rearranged to,

$$\dot{\varphi} = \frac{e}{2 \cdot m_e} \cdot B_z + \frac{C}{m_e \cdot \rho^2}. \quad (2.14)$$

The integration constant  $C$ , represents the initial angular momentum of the electron. Normally  $C$  is chosen to be zero, such that the above formula resembles the LR,  $\dot{\varphi} = (e \cdot B_z) / (2m_e) = \omega_L$ . This holds for electron paths, whose initial velocity lies in a plane through the OA and the electrons' initial position, these are so called "Meridianstrahlen" or meridional rays, see Figure 6. This is actually only valid in a co-rotating coordinate system that resembles the same angular frequency as the electron bundle.

The more general case, where  $C \neq 0$ , describing so called "windschiefe Strahlen" or skew (shear angle) paths/rays, and their relation to electron vortices, will be treated later in sections 2.1.4 and 2.1.6.

To arrive at an expression for the azimuthal image rotation, dependent on the distance the electron "travelled" in the magnetic field, the infinitesimal time element  $dt$  has to be substituted by the z-components' using  $dt = ds / v \approx dz / v_z$ . The relation for the kinetic energy of an electron

$$\frac{m_e \cdot v_z^2}{2} = e \cdot U \quad \text{can be manipulated to calculate the electrons' velocity in z-direction } v_z = \sqrt{\frac{2e \cdot U}{m_e}}.$$

Thus the azimuth increase per path element in z-direction (z-shift) is given by,

$$\frac{d\varphi}{dz} = \sqrt{\frac{e}{8m_e U}} B_z. \quad (2.15)$$

Integrating (2.15), delivers the desired expression,

$$\varphi = \sqrt{\frac{e}{8m_e U}} \int_{z_0}^{z_1} B_z(z) dz. \quad (2.16)$$

Thus, the observed image rotates clockwise or anticlockwise, according to the magnetic field direction and the length of the electrons path travelled inside it. For a field obeying  $\int_{z_0}^{z_1} B_z(z) dz = 0$  the rotation vanishes.

This long known phenomenon of image rotation is somewhat special for electron optics in magnetic fields, but it is not limited to it, nor unique. Recently, it was also shown for photons in slow-light medium (Franke-Arnold, Gibson et al. 2011) and terahertz radiation in topological insulators (Shuvaev, Pimenov et al. 2013), being related to the Faraday effect. Nevertheless, for normal optical imaging systems and for electrostatic electron optics, this effect can be safely

neglected, as it is of the order of  $\mu\text{rad}$ . This is in stark contrast to electron microscopy, because, at common values for the acceleration voltage and magnetic flux density in the OL, the image rotation following the relation (2.16) is of the order of radians. This in fact is not only visible as image rotations, when changing the magnification or objective defocus, but has also consequences on the parallelism of the sample illumination. TEM operators should be aware, that LR in magnetic lens fields introduces deviations from parallel illumination proportional to the diameter of the illuminated area of the order of  $0.4 \text{ mrad} / \mu\text{m}$  (Christenson and Eades 1986), respectively  $0.575 \text{ mrad} / \mu\text{m}$  for the Tecnai F20 S-Twin (Eyidi, Hébert et al. 2006).

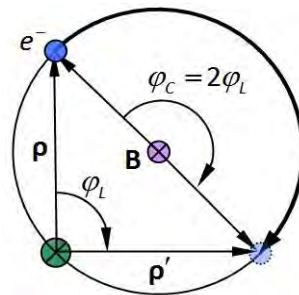


Figure 8: Sketch, showing why LR instead of cyclotron motion is observed in the TEM, with the blue circle being the electron orbiting round a magnetic field line  $\mathbf{B}$ , marked as a violet circled cross, traversing the azimuthal angle  $\varphi_c$  relative to the centre of curvature being double as large as the angle  $\varphi_L$  describing the electrons' azimuthal progression relative to the optical axis, marked as a green circled cross, from  $\rho$  to  $\rho'$ .

Here, it should be noted that electrons always exhibit cyclotron motion inside a magnetic field, being twice as fast as the above derived LR. The reason why LR is actually observed, is that the cyclotron motion occurs relative to centre of curvature depicted in Figure 8, whereas the LR is observed relative to the OA.

### 2.1.4 Electron Vortex Beams

As already mentioned in the introduction, EVB can be characterized in two ways, using the wave- or particle picture.

#### 2.1.4.1 Wave-Mechanical Description

EVB are doughnut (or ring-) shaped intensity distributions, showing a helical phase structure with a phase singularity or screw dislocation at its centre. They carry quantized OAM of  $L_z = m \cdot \hbar$ , where

$m$  denotes the so called topological charge (vortex strength) of an EVB, and  $\hbar$  is the reduced Planck's constant.  $m$  being generally an integer, but at least for optical vortices non-integer structures have been observed (Leach, Yao et al. 2004). Compared to the spin angular momentum, OAM can take any integer value, not only two. EVB also carry quantized magnetic moment of  $M = g \cdot m \cdot \mu_B$  per electron even without spin polarization, with  $\mu_B$  being the Bohr magneton ( $\mu_B = e\hbar / 2m_e$ ) and  $g=1$  the gyromagnetic ratio for classical orbital motion (Bliokh, Bliokh et al. 2007, Gallatin and McMorran 2012). In contrast to the spin angular momentum (SAM), which is always intrinsic, the OAM can be intrinsic or extrinsic, depending on whether the vortex beam shows a net transverse moment (extrinsic OAM) or not (intrinsic OAM). For example, a circular polarized laser beam can set a birefringent particle in rotation about its own axis (intrinsic SAM), whereas a particle placed at the intensity maximum of a doughnut like OVB, would rotate about the beams' axis, and not about its own (extrinsic OAM), and, on the other hand, the same particle would rotate about its own axis, if placed in the centre of the OVB (intrinsic OAM) (O'Neil 2002). For a quantitative description, it is practical to start with the canonical momentum  $\hat{\mathbf{p}} = -i\hbar\nabla$  and the OAM operator  $\hat{\mathbf{L}} = \hat{\mathbf{r}} \times \hat{\mathbf{p}}$ . The z-components of these operators are  $\hat{p}_z = -i\hbar\partial_z$  and  $\hat{L}_z = -i\hbar\partial_\phi$ , thus, their eigenmodes in cylindrical coordinates are represented by plane waves propagating in the z-direction ( $\psi \propto e^{ik_z z}$ ), for the canonical momentum operator, and so called vortex modes in the form of  $\psi_m \propto e^{im\phi}$ , for the OAM operator. The OAM expectation values are quantised and give a discrete spectrum of eigenvalues due to the  $2\pi$  periodicity of the azimuthal phase, given by,

$$\langle L_z \rangle = \frac{\langle \psi | \hat{L}_z | \psi \rangle}{\langle \psi | \psi \rangle} = \hbar \cdot m. \quad (2.17)$$

Whereas the eigenvalues of the momentum operator show a continuous-spectrum  $p_z = \hbar k_z$ . The probability distribution and -currents are defined as following,

$$I = |\psi|^2 \quad \mathbf{j} = \frac{1}{m_e} \cdot \text{Re}(\psi | \hat{\mathbf{p}} | \psi) = \frac{\hbar}{m_e} \cdot \text{Im}(\psi^* \cdot \nabla \psi). \quad (2.18)$$

For vortex beams ( $\psi_m \propto e^{i(k_z z + m\phi)}$ ), the azimuthal component of the probability current (APC) does not vanish, such that the APC reads,

$$\mathbf{j}_m(\rho) = \frac{\hbar}{m_e} \cdot \left( \frac{m}{\rho} \cdot \mathbf{e}_\phi + k_z \cdot \mathbf{e}_z \right) \cdot I_m(\rho). \quad (2.19)$$

To find an expression for the probability distribution  $I_m(\rho)$ , the Schrödinger equation with the free space Hamiltonian, given below, must be solved.

$$\hat{H}\psi = E\psi \qquad \hat{H} = \frac{\hat{\mathbf{p}}^2}{2m_e} \qquad (2.20)$$

Putting the free space Hamiltonian into the Schrödinger equation and rewriting it in cylindrical coordinates leads to,

$$-\frac{\hbar^2}{2m_e} \cdot \left[ \frac{1}{\rho} \cdot \frac{\partial}{\partial \rho} \cdot \left( \rho \cdot \frac{\partial}{\partial \rho} \right) + \frac{1}{\rho^2} \cdot \frac{\partial^2}{\partial \varphi^2} + \frac{\partial^2}{\partial z^2} \right] \cdot \psi = E \cdot \psi. \qquad (2.21)$$

It turns out that for electrons in field free space, limited by an aperture (actually diaphragm), the Schrödinger equation (2.21) yields a Bessel differential equation, which can be solved using Bessel functions of the first kind,  $J_m$ .

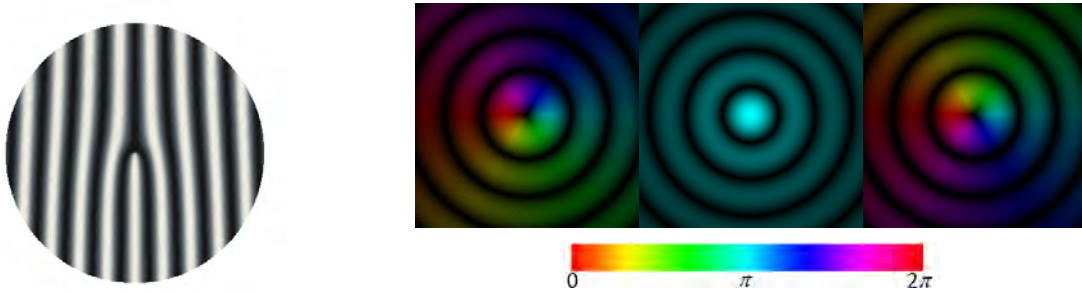


Figure 9: Left: Transmission function of the holographic mask. Right: Bessel beams showing an annular intensity distribution for the  $m = \pm 1$  states and a either right or left handed azimuthal phase ramp from 0 to  $2\pi$ , which is hue colour coded.

Bessel functions of the second kind would diverge at the aperture centre and can therefore be excluded (Schattschneider and Verbeeck 2011). Thus, axially symmetric solutions obeying (2.21) are non-diffracting Bessel beams,

$$\Psi_m^B \propto J_{|m|}(\kappa\rho) \cdot e^{i(k_z z + m\varphi)}, \qquad (2.22)$$

with  $J_{|m|}(\kappa\rho)$  standing for the radial part of the wavefunction, with  $\kappa$  being the transverse wave number, and  $e^{im\varphi}$  representing the helical phase. The intensity distribution of a focused Bessel beam is plotted in Figure 9, right. The wavefunction (2.22) is only solution to the Schrödinger equation(2.21), if the following dispersion relation is met,

$$E = \frac{\hbar^2}{2m_e} \cdot k^2 = \frac{\hbar^2}{2m_e} \cdot (k_z^2 + \kappa^2). \qquad (2.23)$$

In optics, diffracting vortex beams are described by circular symmetric Laguerre-Gaussian (LG) modes, with the field amplitude,

$$LG_{\rho,m}(\rho,\varphi,z) = \sqrt{\frac{2\rho!}{\pi(\rho+|m|)!}} \cdot \frac{1}{w(z)} \cdot \left(\frac{\sqrt{2}\rho}{w(z)}\right)^{|m|} \cdot L_{\rho}^{|m|}\left(\frac{2\rho^2}{w^2(z)}\right) \cdot e^{-\frac{\rho^2}{w^2(z)}} \cdot e^{\frac{ik \cdot \rho^2}{2R(z)}} \cdot e^{-i(2\rho+|m|+1)\arctan\left(\frac{z}{z_R}\right)} \cdot e^{im\varphi+kz}, \quad (2.24)$$

which satisfies the scalar Helmholtz - as well as the paraxial Schrödinger equation with  $\partial^2 / \partial z^2 \approx k^2 + 2ik\partial / \partial z$  and the assumption that  $k^2 - k_z^2 \ll k^2$ , meaning that the transverse wave number is small compared to the longitudinal wave number  $k_z$  (Bliokh, Schattschneider et al. 2012).

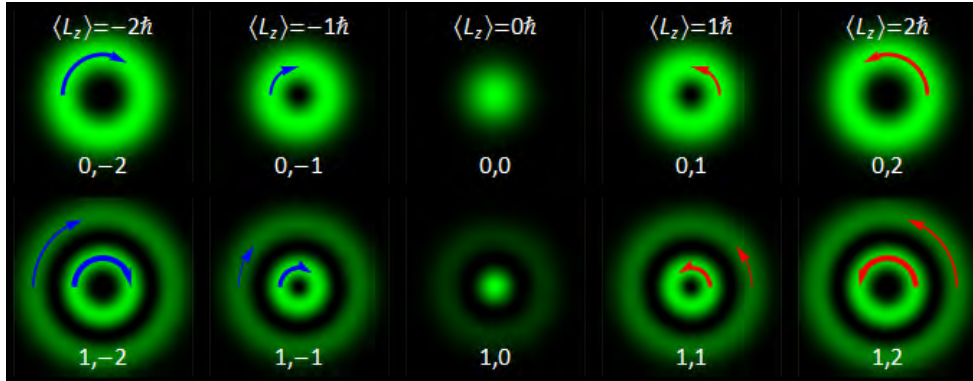


Figure 10: Calculated transverse intensity distributions of LG beams (2.24) for  $\rho = 0, 1$  and  $m = 0, \pm 1, \pm 2$ . Arrows show the direction and strength of the APC flow according to (2.19). Whereas the length and thickness of the lines increases with increasing APC and the position indicates the radius of maximum intensity. This convention is also used in the following figures. For the  $\rho = 1$  modes, the growing APC towards the centre of the intensity distributions can be seen very nicely.

This is the reason, why this solution can also be used to describe EVB (McMorran, Agrawal et al. 2011). One important advantage of LG - over Bessel beams is their transverse confinement. Because the integral  $\int I_{|m|}^B \cdot \rho \cdot d\rho$  of Bessel beams (also that of plane waves) diverges, with  $I_{|m|}^B \propto |J_{|m|}(k_{\perp} \rho)|^2$  being their intensity distribution.  $L_{\rho}^{|m|}$  denote the generalized Laguerre polynomials, where the mode index  $m$  determines the phase structure (or APC) and therefore the topological charge, see Figure 10. Whereas the positive integer  $\rho$  defines the radial structure, e.g. for  $\rho = 0, \rho + 1$  annular rings are visible, see Figure 10 and Figure 11, left.

The function  $w(z)$  is called beam width or – radius and describes the evolution of the beam radius along the  $z$ -direction as,

$$w(z) = w_0 \cdot \sqrt{1 + \left(\frac{z}{z_R}\right)^2}, \quad (2.25)$$

with  $w_0$  standing for the minimum beam radius, also waist radius. By that  $w_0$  defines the position of the focal point or beam waist ( $z = 0$ ), see Figure 11, left, upper right corner and Figure 11, right. The

beam diameter  $2w_0$  at the beam waist is called spot size.  $w(z)$  itself is commonly identified with the radial distance to the beams' centre, where the intensity dropped to  $\sim 13.5\%$  ( $1/e^2$ ) of the beams' maximum intensity. At this radial distance the beam contains approximately 86.5% of the beams total transported energy (Saleh and Teich 2007).

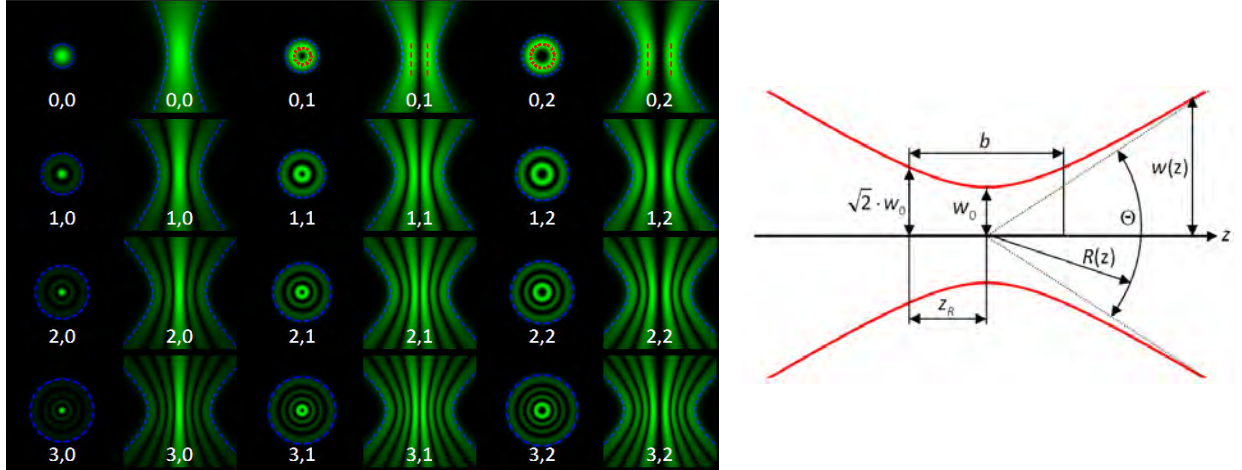


Figure 11: Left: The picture shows xy- and xz-profiles of the first 12 LG modes, according to their  $p, m$ -indices, the dashed red lines indicate the position of the maxima according to (2.28), whereas the dashed blue lines indicate the LG modes' spot size defined by (2.30), right: schematic drawing of the fundamental LG beam parameters.

Sometimes other definitions for the spot size (radius) are used, e.g. the full width at half maximum (FWHM) or the root mean square value. But, the following expressions describe the experimentally observed beam parameters best for the  $1/e^2$  value. Therefore, this definition will be used in this work unless otherwise stated.

The radius of the wavefront curvature is given by,

$$R(z) = z \cdot \left[ 1 + \left( \frac{z_R}{z} \right)^2 \right]. \quad (2.26)$$

And  $z_R$  is the very position where the beams' illuminated area doubles, and related to that the beam width increases to  $\sqrt{2} \cdot w_0$ . This parameter is called the Rayleigh range (Arlt 2003),

$$z_R = \frac{1}{2} \cdot k \cdot w_0^2. \quad (2.27)$$

$k$  represents the wave number of the electrons. The region within  $\pm z_R$  is denoted by the parameter  $b$ , which is called depth of focus or confocal parameter, see Figure 11, right. The beams curvature reaches its maximum at the Rayleigh range.

$\Theta$  is the full opening or convergence angle given as twice the semi-convergence angle  $\theta$ , that reflects the ratio between the incoming electron velocity and its transverse component. Setting the

first derivative of the amplitude of equation (2.24) to zero and solving it for the radial distance  $\rho$  gives the following relation for the radial position of the LG-beams' maximum depending on the topological charge  $m$ , and  $p = 0$  (Baumann, Kalb et al. 2009, Davis and Kaplan 2013),

$$\rho_{\max}^{p=0,m} = \sqrt{\frac{m}{2}} \cdot w(z). \quad (2.28)$$

For  $p = 1$  the radii of the LG-beams' maxima can be calculated with,

$$\begin{aligned} \rho_{\max,inner-ring}^{p=1,m} &= \sqrt{\frac{2m+3-\sqrt{8m+9}}{4}} \cdot w(z) \\ \rho_{\max,outer-ring}^{p=1,m} &= \sqrt{\frac{2m+3+\sqrt{8m+9}}{4}} \cdot w(z). \end{aligned} \quad (2.29)$$

An extended table with numerical calculated values can be found in (Padgett and Allen 1995), page 39, table 1, using  $\rho_{\max}^{p,m} = \sqrt{m/(2a)} \cdot w(z)$ , where  $a$  is the tabulated value for different  $p, m$ .

Figure 11, left, and the expressions (2.28), (2.29) show that LG-beams exhibit a complex radial structure, where increasing orders of  $m, p$  depart drastically from the pure Gaussian beam profile, therefore Phillips and his colleague introduced an alternative definition for the spot size (2.25),

$$w^{p,m}(z) = w_0 \cdot \sqrt{2p+m+1} \cdot \sqrt{1 + \left( \frac{\lambda \cdot z}{\pi w_0^2} \right)^2}, \quad (2.30)$$

with  $\lambda$  being the wavelength of the electron (Phillips and Andrews 1983). Equations (2.28) and (2.30) are visualized in Figure 11, left, as dashed red, respectively blue circles and lines.

The next to last exponent in (2.24) is called the Gouy phase, which yields an additional phase delay of the order of,

$$\Phi_G = (2p + |m| + 1) \cdot \pi, \quad (2.31)$$

to the beams propagation in close proximity of the focal point. The Gouy phase reaches  $\pm 45^\circ$  at the aforementioned Rayleigh range  $z_R$ .

It should be mentioned that, albeit LG- and Bessel beams are well working approximations to EVB in the vicinity of the focal point, they fail to describe the experimental reality above and beyond this region.

As already mentioned in the introduction, a very robust and reliable method to create EVB is to illuminate holographic masks with the electron beam (an incoming plane wave). The holographic mask represents the interference pattern of a target wavefunction, in our case the EVB  $\Psi_t = L(\rho) \cdot e^{im\varphi}$  (omitting  $e^{ik_z z}$ ), and a tilted reference wave  $\Psi_r = e^{ik_x x}$ , with  $k_x$  being a component perpendicular to the incoming wave vector  $k_z$ . The intensity distribution of this interference

pattern is given as,

$$I_{Holo} = |\Psi_t + \Psi_r|^2 = |\Psi_t|^2 + 2\text{Re}(\Psi_t \cdot \Psi_r^*) + |\Psi_r|^2 = \Pi\left(\frac{\rho}{\rho_M}\right) \cdot \left(1 + \cos\left(m \cdot \varphi - \frac{2\pi}{d} \cdot x\right)\right), \quad (2.32)$$

see Figure 10, left. The step function  $\Pi(\rho/\rho_M)$  restricts the mask to the radius  $\rho_M$  and  $d$  is its lattice constant (Verbeeck, Tian et al. 2010a, Schattschneider and Verbeeck 2011, Verbeeck, Tian et al. 2012). As the fabrication of such a continuously varying thickness structure on the nanoscale would be tedious, and, if successful, blocking too much beam intensity, it is discretised by clipping, e.g. all values above 0.5 are rescaled to one and all values below, are set to zero. This procedure leads to a binary holographic electron vortex mask, see section 3.1.1, which creates a line of EVB arranged such that all negative vortex orders are on one side and all positive ones on the other, separated by the  $m = 0$  beam. The discretisation of the mask introduces higher spatial frequencies, causing higher vortex orders than  $m = \pm 1$  to occur.

Interestingly, not only the use of such holographic vortex masks adds the ability to create EVB in a TEM, the electron beam also exhibits a skew inside magnetic lenses, as it is expressed in equation (2.14) in section 2.1.3, according to the LR. The transverse velocity increases proportional to the electrons' radial distance  $\rho$  to the OA. This phenomenon is known as rotational -, rigid-body – or forced vortex (Lugt 1979). Nevertheless, their behaviour is fundamentally different to that of holographical produced irrotational vortices, for further details, see section 2.1.6.

#### 2.1.4.2 Classical Description

The second way to look at EVB is to imagine it as an ensemble or “swarm” of (point like) electrons following a screw trajectory, exhibiting a skew according to the well known formula for angular momentum  $\mathbf{L} = m_e \cdot (\mathbf{r} \times \mathbf{v})$ , see Figure 12, right. Identifying the z-component of the angular momentum with the vortex strength  $m \cdot \hbar$  leads to an expression for the skew velocity or angular velocity,

$$v_\varphi = \frac{m \cdot \hbar}{m_e \cdot \rho}. \quad (2.33)$$

This expression shows a  $1/\rho$  dependence for the transverse velocity component. In fluid dynamics such behaviour is known as irrotational - or so called free vortices (Lugt 1979).



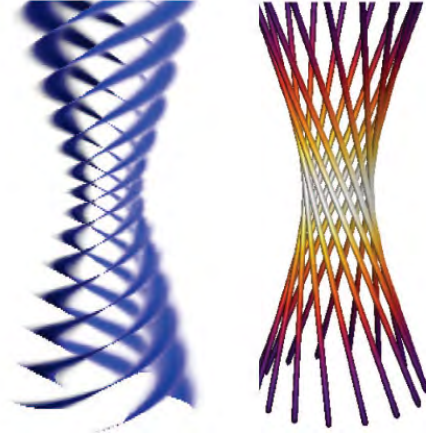


Figure 12: Graphical representation of a simulation of the wavefronts and transverse amplitude going through focus, illustrating the helical phase structure, left, and on the right side a geometric (ray) optics model constituting the EVB as a superposition of straight-line trajectories, taken from (McMorran, Agrawal et al. 2011).

The  $1/\rho$  dependence clearly diverges at the centre of the EVB, thus delivering a physical explanation for the intensity drop in this region. At a certain radius the centripetal force is balanced by the centrifugal one, resulting in a minimum achievable beam radius for electrons carrying OAM.

### 2.1.5 Theoretical Prediction of Peculiar Rotations – Landau States and LG-Beams in Uniform Magnetic Fields

Bliokh and his collaborators theoretically investigated the propagation of EVB in longitudinal magnetic fields in their 2012 Physical Review X paper “Electron Vortex Beams in a Magnetic Field: A New Twist on Landau Levels and Aharonov-Bohm States” and discovered rich, and by then unknown rotational behaviour for EVB (Bliokh, Schattschneider et al. 2012). This section should give an insight on the derivation of these findings, and what exactly they look like, also with regard to their experimental investigation.

To understand how the OAM changes in the presence of a magnetic field, the kinetic- (or covariant) momentum  $\hat{\phi} = \hat{\mathbf{p}} - e\mathbf{A}$  is plugged into the Hamiltonian(2.20), instead of the canonical one. Thus,

$$\hat{H} = \frac{\hat{\phi}^2}{2m_e} = \frac{1}{2m_e} \cdot (\hat{\mathbf{p}} - e\mathbf{A})^2 \quad (2.34)$$

With  $\mathbf{A}$  being the vector potential connected to magnetic field by the relation  $\mathbf{B} = \nabla \times \mathbf{A}$ . Besides, velocity and mechanical momentum, the kinetic momentum also defines the probability current of an electron obeying the continuity equation,

$$I = |\psi|^2 \quad \mathbf{j} = \frac{1}{m_e} \cdot \text{Re}(\psi | \hat{\phi} | \psi) = \frac{\hbar}{m_e} \cdot \text{Im}(\psi^* \nabla \psi) - \frac{e}{m_e} \cdot \mathbf{A} \cdot I. \quad (2.35)$$

In addition the OAM operator  $\hat{\mathcal{L}} = \mathbf{r} \times \hat{\mathbf{p}}$ , now, includes contributions from the vector potential  $\mathbf{A}$ , thus, its z-component can be written as  $\hat{\mathcal{L}}_z = -i\hbar\partial_\varphi - e\rho A_\varphi$ . Using the kinetic OAM spatial density  $m_e \mathbf{r} \times \mathbf{j}$ , the expectation value of the kinetic OAM can be calculated to,

$$\langle \mathcal{L}_z \rangle = \frac{\langle \psi | \hat{\mathcal{L}}_z | \psi \rangle}{\langle \psi | \psi \rangle} = \frac{m_e \cdot \int \rho \cdot j_\varphi dV}{\int I dV} \quad (2.36)$$

Note that the kinetic  $I$ ,  $\mathbf{j}$  and the OAM are invariant to gauge transformations  $\mathbf{A} \rightarrow \mathbf{A} + \nabla\chi$  and  $\psi \rightarrow \psi \cdot e^{i\frac{e\chi}{\hbar}}$ , with  $\chi(\mathbf{r})$  being an arbitrary function. Now, the external magnetic field  $\mathbf{B} = B_z \cdot \mathbf{e}_z$  in the form of the vector potential  $\mathbf{A}$  can be introduced,

$$\mathbf{A} = \frac{B_z \cdot \rho}{2} \cdot \mathbf{e}_\varphi \quad (2.37)$$

This vector potential also resembles a vortex and it is obvious that its introduction sets the kinetic OAM apart from the canonical OAM, whereas in free space they are the same. Putting this vector potential into equation (2.34) yields the Schrödinger equation as,

$$-\frac{\hbar^2}{2m_e} \cdot \left[ \frac{1}{\rho} \cdot \frac{\partial}{\partial \rho} \cdot \left( \rho \cdot \frac{\partial}{\partial \rho} \right) + \frac{1}{\rho^2} \cdot \left( \frac{\partial}{\partial \varphi} + i\sigma \cdot \frac{2\rho^2}{w_M^2} \right)^2 + \frac{\partial^2}{\partial z^2} \right] \cdot \psi = E \cdot \psi, \quad (2.38)$$

with  $\sigma = \text{sgn}B = \pm 1$ . Its' solutions are quantized Landau-states (LS) carrying well defined OAM, and they are very similar to the LG-beams mentioned in the preceding section,

$$\psi_{m,\rho}^L \propto \left( \frac{\rho}{w_M} \right)^{|m|} \cdot L_p^{|m|} \left( \frac{2\rho^2}{w_M^2} \right) \cdot e^{-\frac{\rho^2}{w_M^2}} \cdot e^{ik_z z} \cdot e^{im\varphi} \quad (2.39)$$

They are non-diffracting LG-beams, with the transverse magnetic length parameter  $w_M$  replacing the beam waist radius parameter  $w_0$ ,

$$w_M = \sqrt{\frac{2\hbar}{|e \cdot B|}} \quad (2.40)$$

Another characteristic length scale in a homogeneous magnetic field for LS is the longitudinal Larmor length  $z_M$ , it is comparable to the Rayleigh range of LG-beams,

$$z_M = \frac{2\sqrt{2E \cdot m_e}}{|e \cdot B|} \quad (2.41)$$

That means, the electron rotates azimuthally by  $90^\circ$  within  $2z_M$ . As the LS-LG modes are exact solutions of (2.38) the wave numbers fulfil the dispersion relation,

$$E = \frac{\hbar^2 k_z^2}{2m_e} - \hbar \omega_L \cdot m + \hbar |\omega_L| \cdot (2p + |m| + 1) = E_{\parallel} + \underbrace{E_z + E_G}_{E_{\perp}}. \quad (2.42)$$

In contrast to LG beams, which are only approximate eigenmodes of  $\hat{p}_z$ , with approximate eigenvalues  $p_z \approx \hbar k$ .  $E_z$  in (2.42) is the so called Zeeman energy of the canonical OAM in a magnetic field and  $E_G$  is the Gouy-phase contribution, related to the, before mentioned, Gouy Phase contributions for LG beams, see equation (2.31). The square of the absolute value of the LS (2.39) gives the intensity distribution  $I^L$ , whereas the probability current is calculated following (2.35) as,

$$I_{|m|,p}^L(\rho) \propto \left( \frac{\rho^2}{w_M^2} \right)^{|m|} \cdot \left| L_p^{|m|} \left( \frac{2\rho^2}{w_M^2} \right) \right|^2 \cdot e^{-\frac{2\rho^2}{w_M^2}}, \quad (2.43)$$

$$\mathbf{j}_{m,p}^L = \frac{\hbar}{m_e} \cdot \left[ \frac{1}{\rho} \cdot \left( m + \sigma \cdot \frac{2\rho^2}{w_M^2} \right) \cdot \mathbf{e}_{\varphi} + k_z \mathbf{e}_z \right] \cdot I_{|m|,p}^L(\rho)$$

The probability current in (2.43) is clearly different to the one in (2.19) and, thus, its expectation value is no longer the same, it resembles,

$$\langle \mathcal{L}_z \rangle = \hbar \cdot \left( m + \sigma \cdot \left\langle \frac{2\rho^2}{w_M^2} \right\rangle \right). \quad (2.44)$$

With  $\langle 2\rho^2 / w_M^2 \rangle = 2p + |m| + 1$  representing the normed squared spot size of the LS-LG-modes, such that the kinetic OAM can be given as,

$$\langle \mathcal{L}_z \rangle = \hbar \cdot (m + \sigma \cdot (2p + |m| + 1)). \quad (2.45)$$

The kinetic OAM in free space coincidences with the canonical OAM given by equation (2.17). By introducing magnetic fields, this holds no longer true. Additionally, the changes to the kinetic OAM are directly linked to the Gouy energy (2.42),(2.31) of the LS-LG-modes. Yielding peculiar rotational dynamics according to its radial structure and OAM state, see Figure 13. The introduced magnetic field acts as a magnetic correction that leads to three distinct classes of rotational states. Depending on the mutual orientation of the OAM, and the magnetic field, the APC, drawn as red and blue arrows in Figure 13, changes dramatically. For example, a parallel oriented OAM and magnetic field, such that  $\sigma \cdot m > 0$ , enhances the vortex current and preserves its direction, see Figure 13, left side, whereas an anti-parallel orientation, expressed by  $\sigma \cdot m < 0$ , decreases the vortex current and even reverses its' sign for growing radial distances, Figure 13, right side. In the centre of this "reversal" region, at the point of APC turnover, where the influence of the magnetic field (or vector potential), exhibiting rotational vortex behaviour, outweighs the holographical

created irrotational vortex current, the APC vanishes. The radial distances where this phenomenon occur, turn out to be the positions of the radial maxima of intensity, given by

$$\rho = \rho_{LZG,max}^{p=0,m} = w_M \cdot \sqrt{|m|} \text{ for } p=0 \text{ LS-LG-modes.}$$

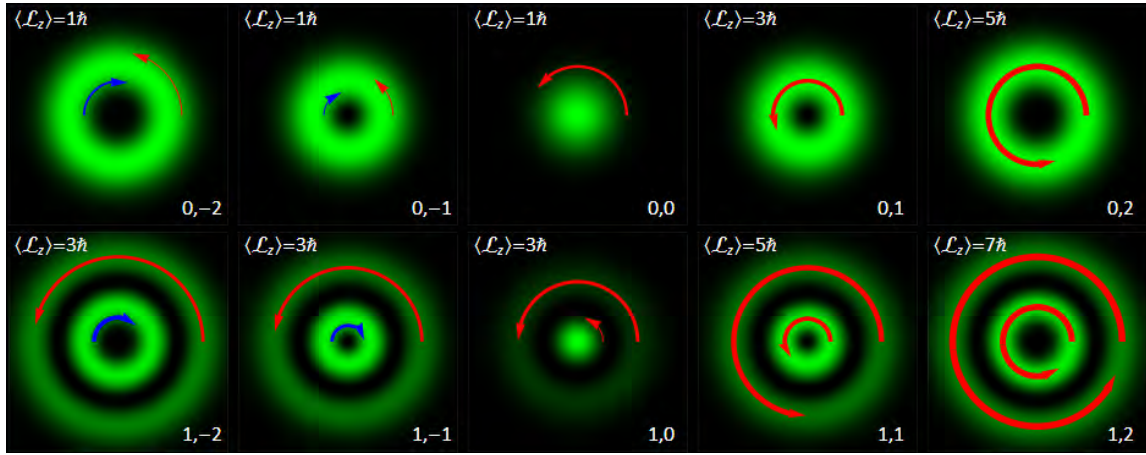


Figure 13: Simulated transverse intensity distribution and APC of LS-LG-modes in a magnetic field with  $\sigma = 1$  for different OAM states, according to (2.43). The radii of the arrows correspond to the intensity distributions' maxima, e.g.  $\rho_{LZG,max}^{p=0,m=0} = 37.3nm$  and  $\rho_{LZG,max,outer-ring}^{p=1,m=2} = 64.7nm$  for  $B = 1.89 T$ , except for the  $p = 0, m = -1, -2$  modes where the radii are  $\pm 30\%$  off the maximum for better visibility, as the APC changes sign at the maximum. The arrows show that for  $\sigma \cdot m > 0$  the APC is enhanced, due to the magnetic field, as well deprivation or even reversal of the APC occurs for  $\sigma \cdot m < 0$ , interestingly, even the  $m = 0$  modes show an APC greater than zero.

Note that the formular for the radial maxima given in Bliokhs' and co-workers Physical Review X paper from 2012 on page nine is missing a square root over  $|m|$ . The LZG (Landau-Zeeman-Gouy) indexing hints at the contributions from the Zeeman- and Gouy energies. One could say that at  $\rho_{LZG,max}^{p=0,m}$  both "vortices" are of the same "strength", above  $\rho_{LZG,max}^{p=0,m}$ , the rotational one overrules the irrotational vortex.

The question now is, how one can visualize and measure this magnetic field corrections and interactions with canonical OAM. - The idea from Bliokh and his colleagues was, that for electrons with fixed energies  $E$  and free propagation along the  $z$ -axis the longitudinal wave vector changes according to the different modes and their dispersion relation (2.42). This slight longitudinal wave vector differences should in principal be observable in their interference patterns. For paraxial electrons the  $z$ -component of the wave vector can be approximated as  $k_z \simeq k + \Delta k_z$  with  $k = \sqrt{2E \cdot m_e}$  and,

$$\Delta k_z = -[\sigma \cdot m + (2p + |m| + 1)] / z_M. \quad (2.46)$$

This represents an additional phase factor for the longitudinal beam propagation called Landau-Zeeman-Gouy phase,

$$\Phi_{LZG} = \Delta k_z \cdot z. \quad (2.47)$$

The influence of this phase can be unveiled by image rotations of “balanced” - respectively “unbalanced” superpositions of LG-modes. For a “balanced” superposition, see Figure 14, two wavefunctions with the same index  $p$  but opposite topological charges  $m$  are coherently summed up,

$$\psi^b = \psi_{-m,p}^L + \psi_{m,p}^L. \quad (2.48)$$

This superposition carries no net canonical OAM, but as there is a difference of phases given by  $\Delta\Phi_{LZG}^b = \mp m \cdot \sigma \cdot z / z_M$ , due to the Landau-Zeeman-Gouy term, a rotation of the interference pattern is expected. This difference in phases enters the azimuthal vortex phase  $\pm im \cdot \varphi$  as  $\pm im \cdot (\varphi - \sigma \cdot z / z_M)$ . Thus, the acquired rotational angle, for the electrons propagation along the  $z$ -direction, is given by,

$$\Delta\varphi = \sigma \cdot \frac{z}{z_M}, \quad (2.49)$$

which equals LR for electrons in a constant magnetic field, because  $z / z_M = |\omega_L| \cdot z / v$ , see Figure 14.

For “unbalanced” superpositions defined by the coherent sum of a wavefunction, which carries no OAM and one which does, while both exhibit the same index  $p$ ,

$$\psi^{ub} = \psi_{0,p}^L + a \cdot \psi_{m,p}^L, \quad (2.50)$$

there are two possible set ups, which were already mentioned before.

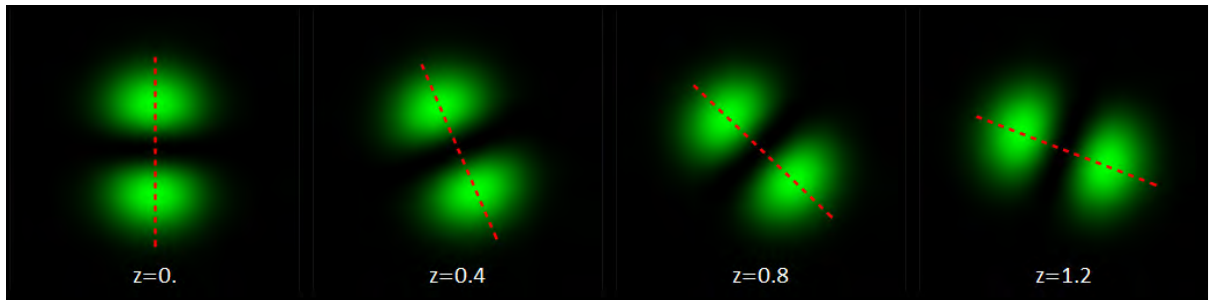


Figure 14: Plot of the probability density of a OAM - “balanced” superposition (2.48) of non-diffracting LG-modes (2.39) with  $m = \pm 1$  immersed in a magnetic field with  $\sigma = 1$  over the course of different  $z/z_M$  values. The rotational speed corresponds to LR. The distance between the two maxima equals 26.4 nm.

One where the OAM and the magnetic field is oriented parallel, which is expressed by  $\sigma \cdot m > 0$  and one with anti-parallel orientation,  $\sigma \cdot m < 0$ .

The factor  $a$  in (2.50) defines a constant amplitude. For both cases the vortex mode gains an additional phase of  $\Delta\Phi_{LZG}^{ub} = -(m \cdot \sigma + |m|) \cdot z/z_M$ . If  $\sigma \cdot m > 0$  the magnetic field rotational vortex and the irrotational vortex add up, such that double-LR or cyclotron rotation (2LR)  $\omega_c = 2|\omega_l|$ ,

$$\Delta\varphi_{LZG}^> = 2\sigma \cdot \frac{z}{z_M}, \quad (2.51)$$

should be observed, see Figure 15.

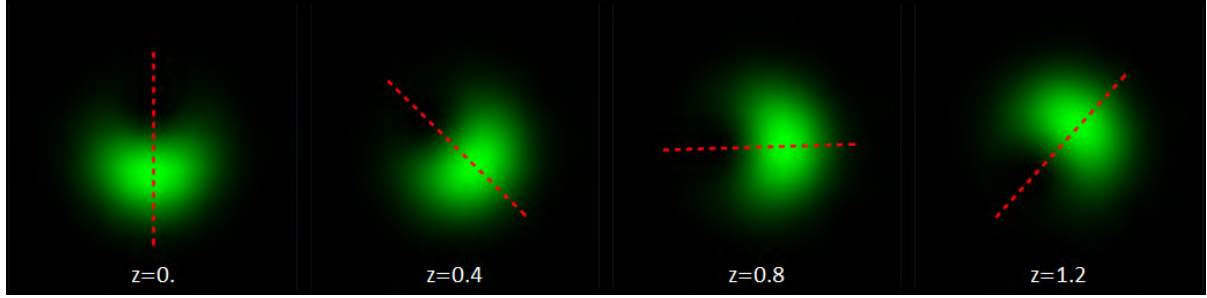


Figure 15: Plot of the probability density of an OAM - “unbalanced” superposition (2.50) with  $m = 1$  and  $a = 1$  immersed in a magnetic field with  $\sigma = 1$  over the course of different  $z/z_M$  values. The rotational speed corresponds to 2LR (2.51). The width of the intensity distribution is approximately 13 nm.

If the magnetic field is aligned anti-parallel to the OAM, obeying  $\sigma \cdot m < 0$ , the above given formula for the phase difference equals zero, which leads to the cancellation of any image rotation.

$$\Delta\varphi_{LZG}^< = 0 \quad (2.52)$$

This is visualised in Figure 16.

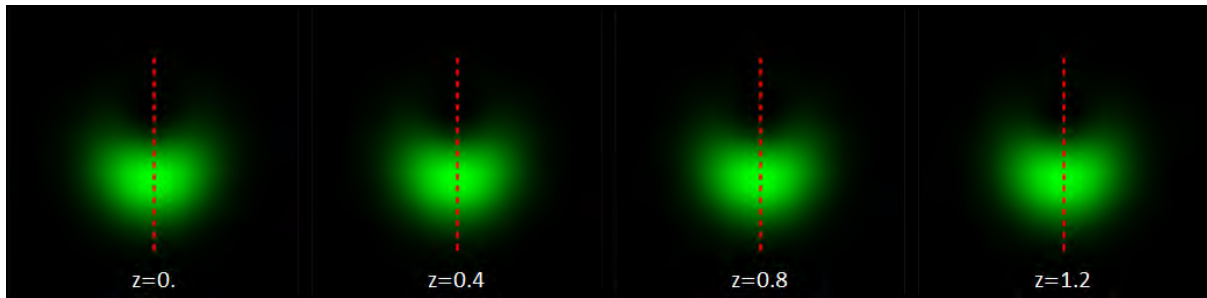


Figure 16: The same as in Figure 15, but with reversed sign of the topological charge  $m = -1$  or, alternatively, reversed B-field  $\sigma = -1$ . There is no rotation observable (2.52).

As already pointed out in section 2.1.3, according to expression (2.14), standard electron imaging theory predicts, that images formed in the magnetic lens field of a TEM, should all rotate with the same speed, being the Larmor frequency. The currently presented LS-LG-modes from Bliokh and

his colleagues pointed out that the influence of homogeneous magnetic fields on the EVB evolution shows peculiar rotational modes including LR, 2LR and zero image rotation. Thus, at the first glance, these findings seem to contradict imaging theory. But, as already hinted at in section 2.1.3 and 2.1.4, if an initial transverse velocity or skew (2.33) is assigned to an electron starting at a certain radial distance to the OA greater than zero, equation (2.14) changes its outcome from solely reproducing LR to practical any rotational speed. This in fact, is part of the basis for the following semi-classical derivation for the EVB rotation in magnetic fields.

### 2.1.6 Semi-classical Derivation of the Electron Vortex Rotation in a Magnetic Lens

#### Field:

The phenomenon of different rotational speeds of EVB can also be understood by the interaction of the already mentioned two complementary manifestations of vortices, e.g. in fluid mechanics. The rotational vortex, also known as rigid body- or forced vortex and the irrotational one, also known as potential or free vortex. Figure 17 qualitatively shows their transverse velocity component  $v_\varphi$  over the radial distance  $\rho$ . In addition superpositions for different “ $\sigma \cdot m$ ”-values to demonstrate that the predicted effect of three distinct rotational speeds,  $\omega_l, \omega_c, 0$ , is confined to a rather small region around a certain position denoted as  $w_m$ , according to Bliokhs’ and his co-workers’ derivation, are also shown. Further it illustrates their fundamental difference that is the  $1/\rho$  dependence of the azimuthal or angular velocity component compared to the linearly increasing azimuthal velocity of a rotational vortex. The label forced vortex points to the fact that an external azimuthal force has to be applied on the particles to increase their angular velocity with growing distance to the vortex centre, e.g. by the lattice of a solid, high viscose fluids or a magnetic field like the OL field. If they were free of any additional azimuthal forces the angular velocity would drop inversely to the radial distance, because of angular momentum conservation, hence justifying the designation as a free vortex, e.g. particles in an inviscid fluid or vacuum. – These two types of vortices are called irrotational, respectively rotational because of their vanishing (at least everywhere outside the centre) and non-vanishing vorticity, that is,  $\boldsymbol{\omega}_{vorticity} = \nabla \times \mathbf{v}$ . This is a measure indicating the local rate of rotation of, for instance particles in a fluid medium. Thus, being twice the rate of angular rotation of the fluid for rotational vortices,  $\boldsymbol{\omega}_{vorticity} = 2 \cdot \boldsymbol{\omega}_{ang.rot.}$ , and  $\boldsymbol{\omega}_{vorticity} = 0$  for irrotational ones. This behaviour can be illustrated by putting small wooden sticks on the surface of a fluid inside a rotating cup. The sticks will rotate with the same angular frequency as the cup, around the centre of the cup, as well about their own axis, such that they are

always aligned perpendicular to the line connecting their centre with the centre of rotation, thus, giving twice the angular frequency for the vorticity. Complementary to that, the wooden sticks will not change their orientation in the cup, when the fluid is set in rotation with a revolving shaft in the middle of the cup, because the sticks' rotation gets exactly cancelled by the decrease of its azimuthal velocity departing from the shaft; see the insets of Figure 17. Apart from the local or microscopic measure for rotation described before, there is another quantity called circulation,

$$\Gamma = \oint_C \mathbf{v} \cdot d\mathbf{l} = \iint_S \boldsymbol{\omega}_{\text{vorticity}} \cdot d\mathbf{A},$$

specifying the vortex rotation or its "strength" on a macroscopic scale.

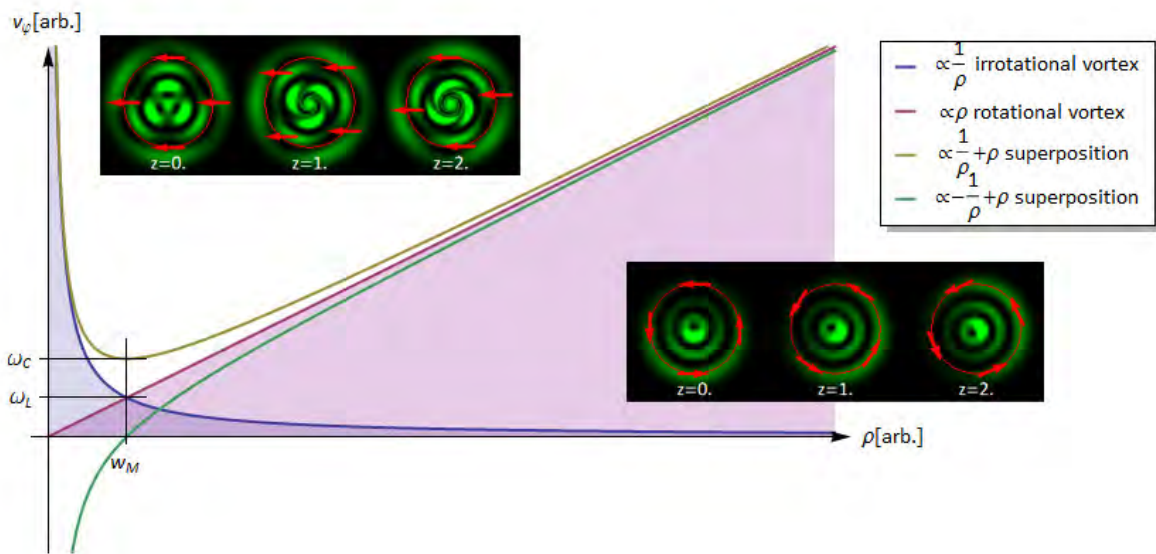


Figure 17: Shows the azimuthal velocity components  $v_\phi$  for pure rotational- (purple line) and irrotational vortices (blue line). The rotational vortex resembles the azimuthal velocity of an electron carrying no initial OAM inside the magnetic OL field. The irrotational vortex resembles the azimuthal velocity of an electron carrying initial OAM propagating through vacuum. Also their superposition with a positive, respectively negative irrotational vortex (beige and green lines) is shown, illustrating that there is a broad spectrum of possible rotational velocities. The region where the three distinct rotational frequencies,  $\omega_L, \omega_c, 0$ , appear, is labelled  $w_M$ , representing the magnetic beam waist. The insets depict the two fundamental vortex modes for different  $z/z_M$  values as an unbalanced LG-mode superposition with a modified azimuthal phase for the irrotational vortex (upper inset). The arrows indicate the "wooden stick" put into the classical flow of particles.

For irrotational vortices,  $\Gamma = 0$ , for any contour not containing the vortex centre and constant if it does. Hence the azimuthal velocity is given by  $v_\phi = \Gamma / (2\pi \cdot \rho)$  and in this way the angular momentum per unit mass turns out to be constant,  $\rho \cdot v_\phi = \Gamma / (2\pi) = \text{const}$ , pointing to angular momentum conservation (Lugt 1979, Cole 2006).



The angular velocity of an irrotational vortex would diverge at its centre, intuitively that situation is clearly unphysical, so the most simple approximation to model “real” vortical flows, is to combine the irrotational vortex with a rotational at its centre, which is labelled Rankine vortex. Here, the angular velocity at the centre is zero, it then linearly increases to a maximum and from there on it decreases inversely proportional to the radial distance. This behaviour is common for fluid vortex flows, but has also been observed for OVB (Grover A. Swartzlander and Hernandez-Aranda 2007). There, it is has been assigned to the finite source size. For EVB this effect may also appears, but it should not be confused with the superposition done in Figure 17, which is the basis for the following derivation of EVB rotational behaviour in magnetic fields.

Now, the connection to the situation in the TEM can be given by starting with the formula for the angle of rotation of an electron inside the column,

$$\varphi(t) = \omega \cdot \Delta t \quad (2.53)$$

where  $\omega$  represents the angular frequency and  $\Delta t$  the time increment. One can replace the time increment by the relation  $\Delta t = \Delta z / v_{\parallel}$ , which transforms the time increment into the experimental accessible z-shift  $\Delta z$  at a given forward velocity  $v_{\parallel}$  of the electron, such that,

$$\varphi(z) = \omega \cdot \frac{\Delta z}{v_{\parallel}} \Rightarrow \omega(z) = \frac{\varphi \cdot v_{\parallel}}{\Delta z} \quad (2.54)$$

Thus, resolving angular frequencies by measuring distances and angles of rotation. Generally, all electrons deflected by the magnetic lens field exhibit LR according to the equation (2.14) in section 2.1.3. If electrons gather additional angular momentum by, e.g. traversing the holographic phase mask described in section 2.1.4, it has to be superimposed on the electron LR. Therefore, the total electron vortex angular frequency will contain contributions from the standard image rotation (Larmor-Frequency), and the additionally acquired rotational speed gained from the interaction with the holographic mask. Thus, the total electron vortex angular frequency can be written as,

$$\omega = \omega_l + \omega_m \quad (2.55)$$

where  $\omega_m$  denotes the contributions from the electron vortex mask. Assuming the electron is a point like particle with the mass  $m_e$  and revolving around the OA at the radius  $\rho$ , the z-component of the angular momentum is given by,

$$L_z = m_e \cdot \rho^2 \cdot \omega \quad (2.56)$$

As the angular momentum gain of one electron passing the holographic phase mask is known and quantified as  $L_z = m \cdot \hbar$ , where  $m$  stands for the topological charge, the angular frequency  $\omega_m$  can be written as,

$$\omega_m = \frac{m \cdot \hbar}{m_e \cdot \rho^2} \quad (2.57)$$

The total angular frequency now reads,

$$\omega = \omega_l + \omega_m = \frac{e \cdot B_z}{2m_e} + \frac{m \cdot \hbar}{m_e \cdot \rho^2} \quad (2.58)$$

Plugging this into equation (2.53) and replacing the time increment by the relation  $\Delta t = \Delta z / v_{\parallel}$ , yields,

$$\varphi_m(z) = \left( \frac{e \cdot B_z}{2m_e} + \frac{m \cdot \hbar}{m_e \cdot \rho^2} \right) \cdot \frac{\Delta z}{v_{\parallel}} \quad (2.59)$$

As the magnetic OL field induces LR, it also generates an inward directed radial force  $F_{\rho}$  according to (2.8) that converges or focuses the electron beam in the front focal plane of the OL with the semi-convergence angle  $\theta$ . Therefore  $\rho$  has to be replaced by the function  $\rho(z) = z \cdot \tan \theta$ . This assumption may hold at least for regions off the Rayleigh-range (2.27).  $\Delta z$  can be turned into an integral over  $z$ .

Concerning the magnetic field strength distribution, it was already argued in section 2.1.2, and will also be quantitatively proved in sections 4.1.1. and 4.1.2 by measurements of the OL field, that it is reasonable to assume a constant magnetic field over the experimental accessible  $z$ -shift range. These considerations lead finally to the following expression for the azimuthal angle of rotation of an EVB over the  $z$ -shift,

$$\varphi_m(z) = \int_{z_1}^{z_2} \left( \frac{e \cdot B_z}{2m_e} + \frac{m \cdot \hbar}{m_e \cdot (z \cdot \tan \theta)^2} \right) \cdot \frac{dz}{v_{\parallel}} = \frac{1}{m_e \cdot v_{\parallel}} \cdot \left[ \frac{e \cdot B_z}{2} \cdot (z_2 - z_1) + \frac{m \cdot \hbar}{\tan^2 \theta} \cdot \left( \frac{1}{z_1} - \frac{1}{z_2} \right) \right] \quad (2.60)$$

where the value  $z_2$  stands for the  $z$ -shift and  $z_1$  denotes the position of the observation plane. In Figure 18, the above formula is plotted for different values of  $m$ . There it can be seen that due to the convergent character of EVB in the microscope, which was not explicitly included in Bliokhs' derivation, a broad variety of different azimuthal velocities, indicated as the curves acclivity in Figure 18. It is the LR which dominates the electrons' evolution along the OA for all OAM states for over- and underfocus positions. The three distinct rotational frequencies,  $\omega_l, \omega_c, 0$ , show up, but only restricted to a small region around the  $z$ -shift position where the convergent electron beams' radius is of the order of the magnetic beam waist  $w_M$ , introduced by Bliokh and co-workers. There, the two complement vortex effects enhance or completely cancel each other out. This in fact poses an experimental challenge as the rotational angle increments are very low. Approaching the Rayleigh-range and the beam waist region, marked with the semi transparent red rectangle in

Figure 18, the model predicts strongly accelerated rotation. This fast rotation can be understood as a result of angular momentum conservation. As the electron approached smaller radii, its angular velocity increases with  $1/\rho$ . Additionally the influence of the rotational vortex imposed by the OL diminishes.

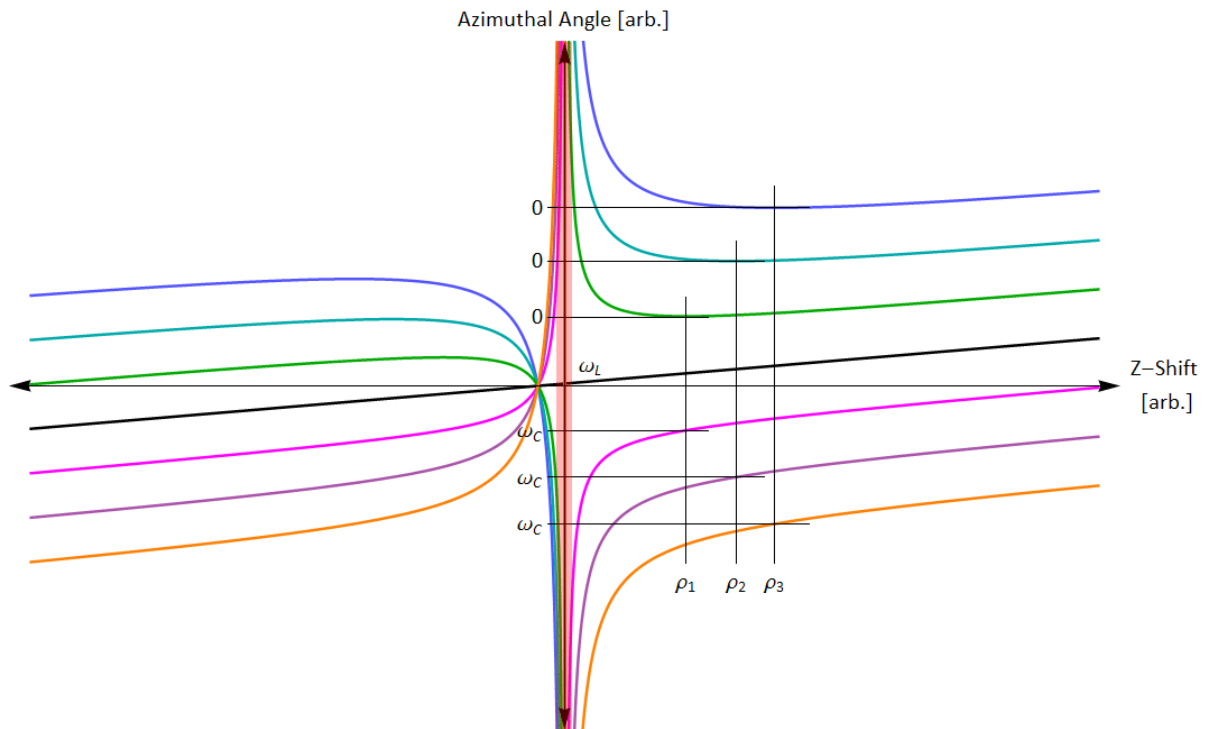


Figure 18: Diagram, showing the azimuthal angle of rotation over the z-shift of seven convergent (vortex) electrons moving through a constant magnetic field with different values of  $m$ . The assignment is  $m = 0$ , black line,  $m = +1, +2$  and  $+3$ , pink, purple and orange line,  $m = -1, -2$  and  $-3$ , green, cyan and blue line. The axial position where the electrons' rotational and irrotational vortex character superimpose, such that three distinct rotational frequencies,  $\omega_L, \omega_c, 0$ , appear, are marked with  $\rho_{1,2,3}$  according to (2.28). For z-shift values within the Raleigh-range (red transparent rectangle) the model diverges and is clearly not physical. Note that (2.60) resembles the azimuthal angle of a line standing perpendicular to the cutting line of the EVB and therefore the  $180^\circ$  Gouy-Phase flip over at the focus is not visible in the plot.

With increasing orders of  $m$  the EVB radii increase, as well as the positions where both vortex phenomena cancel themselves, move further away from the focal point. This results in increased offset azimuthal angles for higher orders of  $m$ .

Another argument to vindicate this semi-classical derivation has been put forward in 1927 by Paul Ehrenfest, who stated that the quantum mechanical expectation values of the electrons' position, as well as its momentum, must obey the classical equations of motion. Such that,

$$\frac{d\langle \mathbf{r} \rangle}{dt} = \frac{\langle \hat{\rho} \rangle}{m_e}, \quad \frac{d\langle \hat{\rho} \rangle}{dt} = \frac{e}{m_e} \cdot \langle \hat{\rho} \rangle \times \mathbf{B}, \quad (2.61)$$

with  $\langle \mathbf{r} \rangle = \langle \Psi | \hat{\mathbf{r}} | \Psi \rangle / \langle \Psi | \Psi \rangle$  being the expectation value of the position, and  $\langle \hat{\rho} \rangle = \langle \Psi | \hat{\rho} | \Psi \rangle / \langle \Psi | \Psi \rangle$  the expectation value of the electrons' kinetic momentum  $\hat{\rho} = \hat{\mathbf{p}} - e\mathbf{A}$  (Ehrenfest 1927). Thus, the centroid motion of the electrons probability density can be described by classical laws. This has important consequences for the convergence angle that will be used to fit the semi-classical model to the experimental data. For half-moon like intensity distributions the centroid convergence angle can be calculated to  $4 / (3\pi) \cdot \theta$ ,  $(0.42 \cdot \theta)$ .

## 2.2 Spin-to-Orbit Conversion – The Electron STOC-Process

In the preceding sections the focus was laid on holographic creation of vortex beams carrying OAM, here, a completely different approach using angular momentum conservation, to convert the SAM of photons, respectively, electrons, into OAM, and vice versa, will be introduced (Marrucci, Manzo et al. 2006, Karimi, Marrucci et al. 2012b, Grillo 2013, Grillo, Marrucci et al. 2013, Karimi, Grillo et al. 2013). This so called STOC-process, well established in optics, also works the other way round, thus, the question arises, if it could be transferred to high energy particle physics, e.g. electron optics. This would be beneficial because spin polarized electron sources for TEM are not commercially available, and at the same time they would enable magnetization studies on the nanoscale in spintronic- and high-density storage devices (Kuwahara, Ichihashi et al. 2004).

Exactly this question was addressed by Karimi and his collaborators in their 2012 Physical Review Letters paper “Spin-to-Orbital Angular Momentum Conversion and Spin-Polarization Filtering in Electron Beams”, as well as in following publications. Thus, this work will be the basis for the following introduction to this topic (Karimi, Marrucci et al. 2012b).

### 2.2.1 Electron Spin - Polarization

In 1922 Walther Gerlach and Otto Stern experimentally observed that a beam of silver atoms possessing no orbital angular momentum, as their outermost electron is an  $s^1$ -electron, spreads up in two distinct parts after the passage of an inhomogeneous magnetic field. Classically, at least for a point like electron model, one would expect the particle beam to resemble a continuous distribution with one maximum at the centre (Gerlach and Stern 1922). This work inspired Uhlenbeck and Goudsmit a few years later to propose a new degree of freedom for the electron, associated to this observed additional angular momentum and magnetic moment, an “inner rotation” or intrinsic angular momentum, called electron spin (ES) (Uhlenbeck and Goudsmit 1925). This new property behaves quite similar as the orbital angular momentum, but its associated magnetic momentum is twice that of the one associated to the orbital angular momentum. This is called anomalous magnetic moment or electron g-factor, denoted as  $g_e$ . More recently, the anomalous factor 2 is no longer referred to as anomalous, but its slight deviation from being exactly 2 is so. The spin quantum number is named  $s$ , it is equal  $\frac{1}{2}$  for fermions, like the electron and its absolute value is given by  $|\mathbf{s}| = \sqrt{s \cdot (s+1)} = \sqrt{3/4} \cdot \hbar$ , whereas its projection onto the  $z$ -

direction is called magnetic spin quantum number  $m_s$ , with the two eigenvalues  $s_z = \pm\hbar/2$ . The experimentally measurable spin magnetic moment is given by  $\mu_z = g_e \cdot \mu_B \cdot s_z / \hbar \approx \mu_B$ . This magnetic moment behaves like a tiny magnetic dipole and the force acting on it in a magnetic field is given by,

$$\mathbf{F} = \nabla(\boldsymbol{\mu} \cdot \mathbf{B}), \quad (2.62)$$

(Demtröder 2005b). The device used in the Stern-Gerlach experiment is producing a spin polarized particle beam. This actually does not work for electrons because of their much stronger interaction with magnetic fields, mediated through their charge. Nevertheless, there are proposals to overcome this limitation (Gallup, Batelaan et al. 2001). An important measure to characterize the efficiency of a spin polarisation device is the degree of spin polarisation which is defined as,

$$P = \frac{N_u - N_D}{N_u + N_D}, \quad (2.63)$$

with  $N_u$  and  $N_D$  being the number of particles with spin-up or parallel alignment to the measured axis, respectively spin-down or anti-parallel alignment. And in so indicating the particle beams' deviation from a uniform spin distribution. Giving  $P = 0$  for a totally unpolarised beam and  $P = 1$  for a perfectly polarized beam. For example, already working polarization techniques for electron beams like Mott-scattering on heavy atoms, where the spin-orbit interaction is yielding different scattering cross sections depending on the incident electrons' spin, reaches spin polarisation values up to 30 %, photoionisation of unpolarized atoms up to 80 % and GaAs photocathodes up to 70 %, but with much higher beam intensities (Berndt 2005). Up to now, there is only one TEM in the world, capable of producing and detecting spin polarized electrons (Kuwahara, Ichihashi et al. 2004).

### 2.2.2 STOC-Process for Electrons

In 2006, while studying dye-induced total optical torque enhancement on spherical liquid crystal droplets, the question arose, why radial dye-doped spherical droplets, contrary to homogenous dye-doped ones, did not rotate (Manzo, Paparo et al. 2006). Further investigations led the team around Manzo and Marrucci quite quickly to the finding that there are two ways to exchange optical angular momentum with matter. Spin-only transfer is mediated by anisotropic media, e.g. normal birefringent wave plates, trapped microscopic particles and liquid crystals. An independent OAM coupling to solids is mediated by inhomogeneous isotropic transparent media. Now one

would expect that when combining these two effects in anisotropic inhomogeneous media, the SAM and OAM still remain separately controllable. But this is not the case, for certain conditions the change of SAM, also changes the photon beams' OAM. Further more, there are geometries where no torque at all is transferred to the media, meaning that the reversal of the SAM is fully balanced by the introduction of OAM and vice versa. The above mentioned geometries are represented by so called q-plates, which are in fact slabs of a birefringent material with a phase retardation of  $\pi$ , e.g. a  $\lambda/2$  plate and a transverse optical axis pattern with a topological defect at the centre, see Figure 19. The transverse pattern describing the q-plate is given by,

$$\alpha(\rho, \varphi) = q \cdot \varphi + \alpha_0(\rho), \quad (2.64)$$

with  $\rho, \varphi$  being the radial distance to the centre and the azimuthal angle, respectively.  $q$  is the number of rotations of the optical axis on a path circling once around the centre, it also stands for the amount of topological charge enclosed, it must be integer or semi-integer and  $\alpha_0(\rho)$  represents the initial optical axis orientation, see Figure 19, left, for some different  $q$ ,  $\alpha_0(\rho)$  examples and Figure 19, right for the used coordinate system.

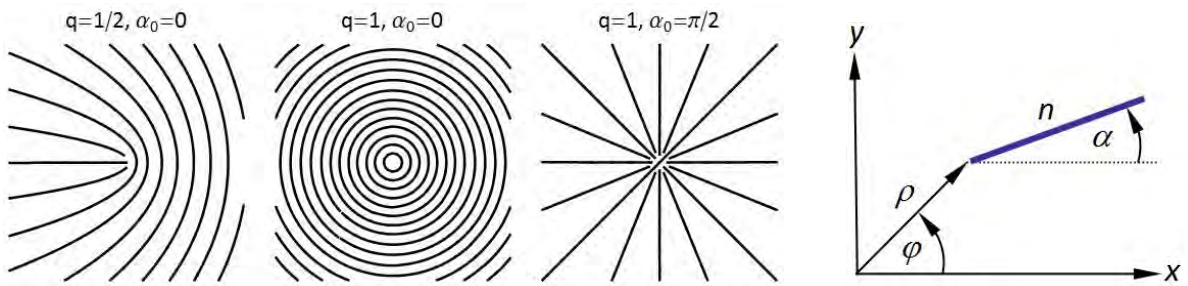


Figure 19: Left: q-plate patterns for different values of  $\alpha_0$  and  $q$ , showing the topological defect at the centre. Right: coordinate system for the transverse optical axis pattern.

If left handed or spin parallel photons with no OAM ( $L_z = +\hbar$ ,  $m=0$ ) are sent through a  $q=1$  and  $\alpha_0=0$  q-plate, their SAM reverses sign and gets “redistributed” to an OAM of  $L_z = +2\hbar$ , while the overall angular momentum remained the same,  $\Delta L_z = 0$ . No torque was exchanged with the q-plate and by that explaining the aforementioned puzzle of non rotating liquid crystal droplets. For the general photon angular balance, see Table 1. Note that, according to Table 1, set ups involving  $q \neq 0$ ,  $\Delta L_z = \pm(q-1) \cdot \hbar \neq 0$ , will exert a torque on the q-plate device, such that their STOC efficiency will simultaneously drop.

Here it should be mentioned that after Marucci's discovery of the STOC process in inhomogeneous anisotropic media, other techniques were discovered to transfer OAM to SAM and vice versa,

incorporating strongly focused beams and semiconductor micro cavities (Zhao, Edgar et al. 2007, Manni, Lagoudakis et al. 2011). Also a thorough theory coping with these different origins of STOC was introduced (Bliokh, Ostrovskaya et al. 2011).

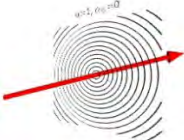
Angular momentum	Input state		Output state
SAM	$L_z = \pm \hbar$		$L_z = \mp \hbar$
OAM	$L_z = m \cdot \hbar$		$L_z = m \cdot \hbar \pm 2q \cdot \hbar$
SAM+OAM	$L_z = \pm \hbar$		$L_z = [m \pm (2q - 1)] \cdot \hbar$

Table 1: Shows the general photon angular momentum balance for the STOC process.

Now, the proposal of Karimi and his colleagues is, that this STOC process works not only for photons in inhomogeneous anisotropic media, but may also work with electrons in magnetic fields. For that, one has to replace the birefringence media by a transverse magnetic field and the inhomogeneous q-plate pattern by inhomogeneous fields possessing a topological defect, e.g. a quadrupole field.

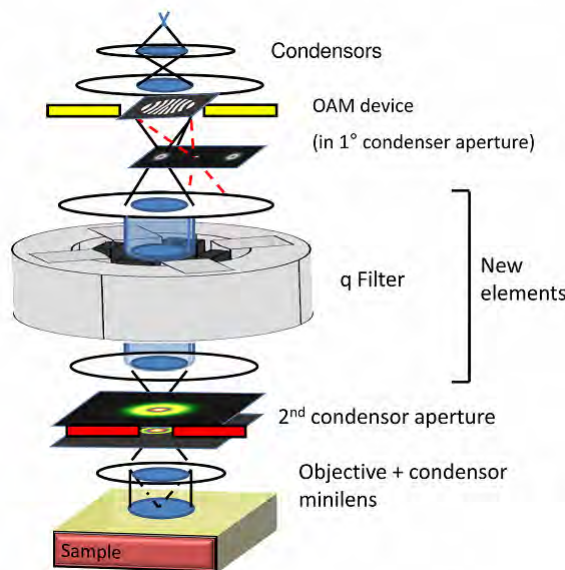


Figure 20: Proposed integration scheme of an electron STOC device (q-filter) into a TEM column. An incident electron beam should be converted to an EVB using a holographic vortex mask. One vortex order is selected and sent through an additional condenser lens. It then enters the space-variant Wien filter and undergoes spin precession. Afterwards the parallel beam is focused again by the “second” condenser lens. In the C2 aperture plane the desired spin polarisation should show up as a spatial separation of the two spin states, thus ready to be “selected” with the C2 aperture by blocking the outer ring of electrons. The filtered spin polarized portion of the electron beam then enters the OL and illuminates the sample (Karimi, Marrucci et al. 2012b), supplementary material.



That combination acts on the ES such that it precesses by  $180^\circ$  and concomitantly imprints OAM to the electron or if an EVB is used as input, ES polarisation should arise.

In contrast to photons, electrons carry charge and by that, magnetic- and electric fields induces large forces on it, approximately 3 to 8 orders of magnitude larger. This effect would overrule the effect of equation (2.62). The solution Karimi and his team propose, is to combine electric- and magnetic fields in a Wien filter like manner, to compensate the Lorentz force.

The quadrupole setup ( $q = -1$ ) is chosen because there are no field sources needed at the OA. Figure 20 shows how this q-plate device for electrons could be integrated in a TEM. The asserted spin polarisation degree is as high as 97.5%. In more recent publications from Karimi, Grillo, Marucci and co-workers this value was strongly reduced (Grillo, Marrucci et al. 2013, Karimi, Grillo et al. 2013).

### 3 Methods

In the first part of the following chapter, it will be described how the TEM is alternatively used as an electron optical workbench to find out more about the electron vortices' rotational behaviour in the magnetic objective lens field. In the second part, there will be a short introduction to the main features of the numerical simulation of the proposed spin polarizing STOC-device.

#### 3.1 Vortex Rotation Experiments

Up to now, there has been plenty of experimental work done to determine Gouy-phase rotations and associated phenomena of OVB (Arlt 2003, Hamazaki, Mineta et al. 2006, Baumann, Kalb et al. 2009, Löffler, Exter et al. 2011). Even in macroscopic super-fluidic helium systems, vortex rotations showed up (Varmchuk and Gordon 1979).

For electrons, the experimental landscape is much sparser populated, for example only the propagation dynamics in the Gouy-phase regime, that is the close vicinity of the focal point, where rapidly changing azimuthal angles of rotation occur, has been studied recently (Guzzinati, Schattschneider et al. 2013, McMorrán, Pierce et al. 2013). With Bliokhs' and co-workers' predictions of peculiar rotations in mind, the experimental test of the rotational behaviour of EVB in magnetic fields far off the Rayleigh range, and with that far off the Gouy-phase regime, is still outstanding. The crucial thing about that are the dimensions. The effects of LS-LG modes are orders of magnitude smaller than the Gouy-phase rotations. For instance the expected image rotation angles over the z-shift range are  $\sim 3^\circ/100 \mu\text{m}$  compared to  $\sim 1800^\circ/100 \mu\text{m}$  for the Gouy-phase region.

On the one hand this clearly shows that these two very different effects can experimentally be well separated, but on the other hand, it also involves detecting LS-LG modes is far more challenging.

Nevertheless, a TEM offers sufficient conditions to observe the rotations, as it is shown infra.

##### 3.1.1 Experimental Parameters

All experiments were carried out on a FEI Tecnai F20 field emission gun (FEG) TEM located at the TU-Vienna 8<sup>th</sup> floor. The experiment on image rotations of a Cu-grid was carried out on a Tecnai G20 LAB<sub>6</sub> (lanthan hexaboride thermionic electron gun) TEM at the same location. In the course of this work, the electron gun of the F20 was replaced by an X-FEG, which is a state of the art field emission electron gun, delivering more beam current, at higher spatial coherence. The acceleration voltage

was set to 200 kV in all experiments. Different magnifications were used but they were mostly of the order of 86000 x. Also different spot sizes were tried out; the best results were achieved with spot size 10, certainly due to its high spatial coherence. Both of the microscopes are equipped with a Super-Twin OL exhibiting a magnetic field strength of 1.89 T, when turned to eucentric focus position, which was around 95.8 % of the objective excitation. This field value will be vindicated in section 4.1.1.

The diameter of the holographic vortex mask was 21  $\mu\text{m}$ , see Figure 21, which led to a convergence semi angle  $\theta = 1.16$  mrad. An overview scanning electron microscope (SEM) picture of the holographic vortex mask used for the present work is shown in Figure 21, on the left side, and on the right side, its cross-section can be seen. The chosen diameter was a compromise between gaining enough intensity even in higher vortex orders and a relatively low convergence angle. This enlarges the z-shift region where the diffracting vortex beam approximates the non diffracting LS-LG mode with a beam waist  $w_M$ .

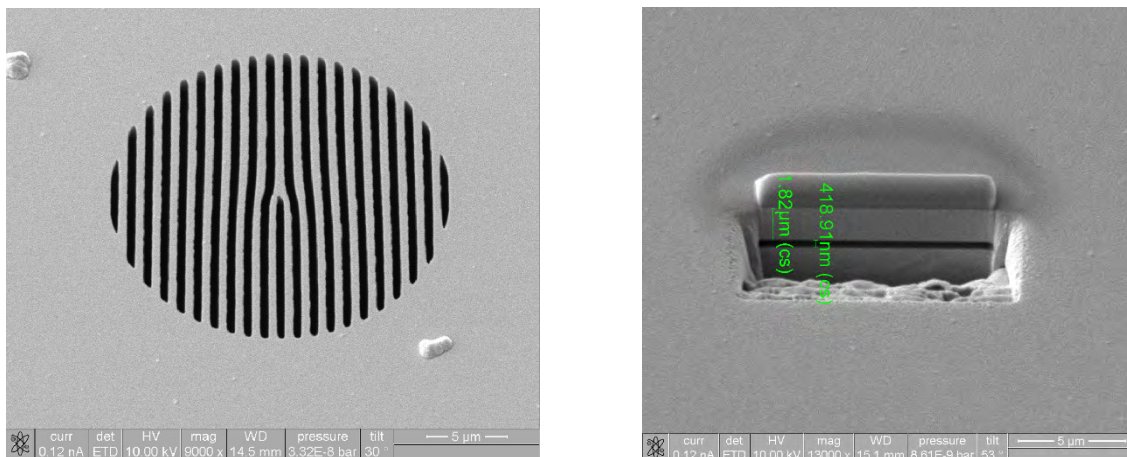


Figure 21: Left: SEM image of the holographic electron vortex mask with a diameter of 21  $\mu\text{m}$  Ag/Pd on 400 nm  $\text{Si}_3\text{N}_4$ , Right: FIB prepared cross section of the mask showing a 1.8  $\mu\text{m}$  thick layer of Gold-Palladium (Au/Pd) on a 400 nm Silicon-Nitride ( $\text{Si}_3\text{N}_4$ ) support.

The holographic mask, exhibiting the characteristic fork like structure in its centre, was produced by cutting a 1  $\mu\text{m}$  period grating into a 1.8  $\mu\text{m}$  thick Gold-Palladium layer, sputtered on a 400 nm thick Silicon-Nitride support, using a focused ion beam machine. The grating period was chosen as small as possible to gain high separation angles between the different vortex orders. This is crucial because higher separation angles provide the possibility to choose higher defocus values without overlapping vortex orders, which in turn improves the angle acquisition accuracy. In principal the grating period could be reduced even further, e.g. down to 50 nm, to the expense of mask stability and a high

portion of undiffracted electrons in the zero order beam (McMorran, Agrawal et al. 2011). This can be explained by the fact, that the minimum aspect ratio of FIB milled structures is of the order of 1:3, meaning that 25 nm grating bars giving a grating period of 50 nm cannot be thicker than 75 nm. Such thin films are easily penetrated by 200 keV electrons. For comparison, the 1.8  $\mu\text{m}$  thick grating bars of the holographic mask in Figure 21, block roughly 95 % of the incident electrons, this would result in only 15 % blocking for a 75 nm thick membrane, using Beer-Lambert absorption law. Even though being a fairly conservative estimate, experimentally, it would be problematic, as the zero order beams' intensity would be disproportionally high and by that reducing the possible image recording times significantly. As a result the observation of angular rotations of higher vortex orders would get worse.

The holographic vortex mask in Figure 21 was then placed into the second condenser lens (C2) aperture holder of the F20 FEG TEM, to produce EVB in the observation plane of its OL. The focused EVB show up aligned along a line, where the central spot carries no OAM. It resembles a Gaussian intensity distribution with a beam waist radius of 1 nm quite well. The "diffraction orders" on both sides of the central beam do carry topological charge  $m$  and show the characteristic intensity drop at their centre. Their radii of maximum intensity are described by the formula (2.28). Depending on the position relative to the central beam they carry positive or negative OAM starting with  $m = \pm 1, \pm 3, \pm 5 \dots$ . The odd "spacing" is due to the masks' geometry. The separation angle between the central beam and the first vortex order is given by 2.4  $\mu\text{rad}$  or 24 nm, respectively 5  $\mu\text{rad}$  (50 nm) for succeeding higher orders. All positive, respectively negative orders gather on either side of the central  $m = 0$  beam.

#### 3.1.2 Experimental Setup

Observing azimuthal rotations of a radial symmetric object is impossible, therefore Bliokh and his co-workers suggested to create EVB superpositions, which are breaking the radial symmetry, see Figure 15 and Figure 16, to make them visible.

From a classical point of view, a straightforward way to achieve this beam shape, is to block half of the incoming EVB intensity by a knife-edge, see Figure 22. This technique is originally borrowed from the optics community, see for example (Arlt 2003, Cui, Wang et al. 2012), and has already been used for EVB to detect the rapid Gouy-phase rotations (Guzzinati, Schattschneider et al. 2013).

Surely, one could think of other approaches directly creating the desired balanced and unbalanced EVB superpositions, but for one, the EVB created by the holographic mask in the C2 aperture plane

are also used for other experiments, like electron magnetic dichroism, and for the other, attempts doing so, indicate that it is not possible to resolve faint LS-LG mode rotations (McMorran, Pierce et al. 2013).

Figure 22, shows a sketch of the experimental setup used to observe EVB dynamics in magnetic fields. First, the electron beam hits the above described holographic vortex mask, shown in grey on the upper side of Figure 22, such that the electrons are diffracted into different diffraction orders each of which lie on a horizontal line in the front focal plane of the OL. In principal it should be possible to use other holographic mask designs, where the different vortex orders lie on a vertical line at different  $z$ -positions, but as their production is even more challenging than the fork like structure, only those were used in this experiment (Verbeeck, Tian et al. 2012).

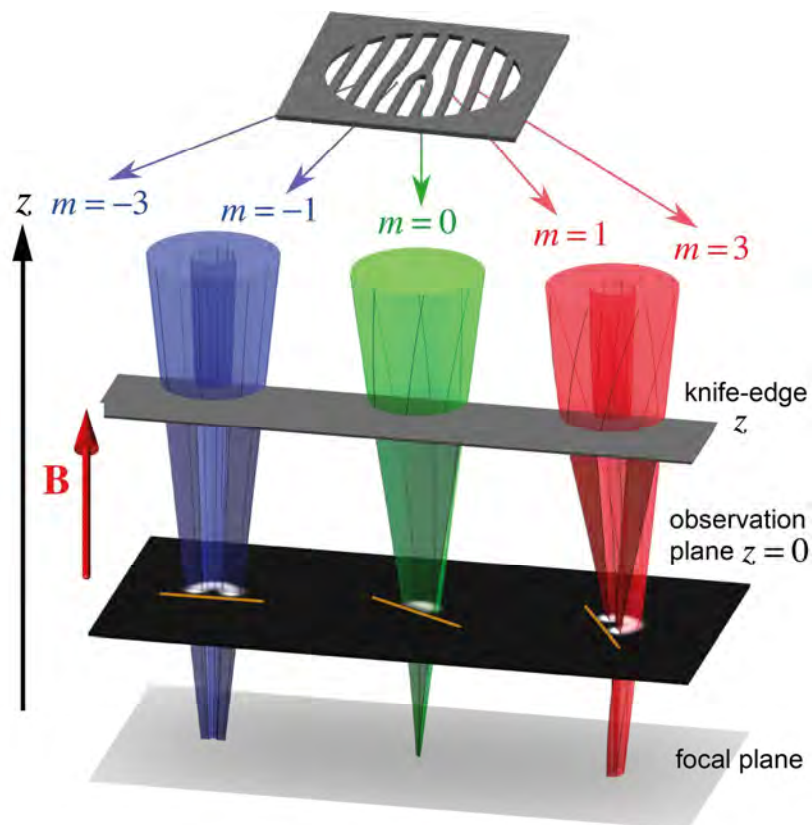


Figure 22: Sketch of the experimental setup (not to scale). One half of each incoming convergent EVB order (blue, green, red) is blocked by a sharp KE (grey). The KE is then  $z$ -shifted from approximately  $-350\ \mu\text{m}$  to  $+350\ \mu\text{m}$  in order to see a variation of the azimuthal cutting angle (orange line) in the observation plane (black) at  $z = 0\ \mu\text{m}$ . The distance  $z_f$  between the observation plane and the focal plane is chosen to lie in the range between  $2.5$  to  $11.5\ \mu\text{m}$ .

After the electron beam has passed the holographic vortex mask, it is incident on a knife-edge (KE) at the  $z$ -shift position  $z$ . It is inserted in the sample holder, such that its edge is aligned approximately

parallel to the 2.5 to 11.5  $\mu\text{m}$  defocused line of vortices. The angle  $\varphi_{KE}$  of how to put the KE into the sample holder is given by the empirical relation  $\varphi_{KE} = 90^\circ - \varphi_{OL} - \varphi_{VL}$ , where  $\varphi_{OL}$  is the offset angle between the “real” azimuth of the KE in the sample holder, when looking at the beam facing side of the KE, and its actual appearance in the microscope, according to Figure 23. It turned out that this angle is approximately  $50^\circ$  when working at the eucentric focus. The subscript of  $\varphi_{OL}$  hints at the circumstance that the image rotation of the projective lens system is compensated, such that only the OL magnetic field contributes to the observed image rotation, e.g. of the vortex line.  $\varphi_{VL}$  represents the observed azimuthal angle of the line of EVB relative to the horizontal line in the TEM micrograph, Figure 23. See, Figure 22, for the EVB line in the observation plane. And Figure 24, to see, how that relates to the KE positioning. A single tilt holder was used in nearly all experiments, because the upper face of the KE was pretty close to the eucentric height ( $z = +15 \mu\text{m}$ ), such that the z-shift series could be taken with nearly symmetrical ranges from  $z \approx \pm 350 \mu\text{m}$ . For example the double-tilt-rotation holders’ offset to the eucentric height was  $z = +150 \mu\text{m}$ .

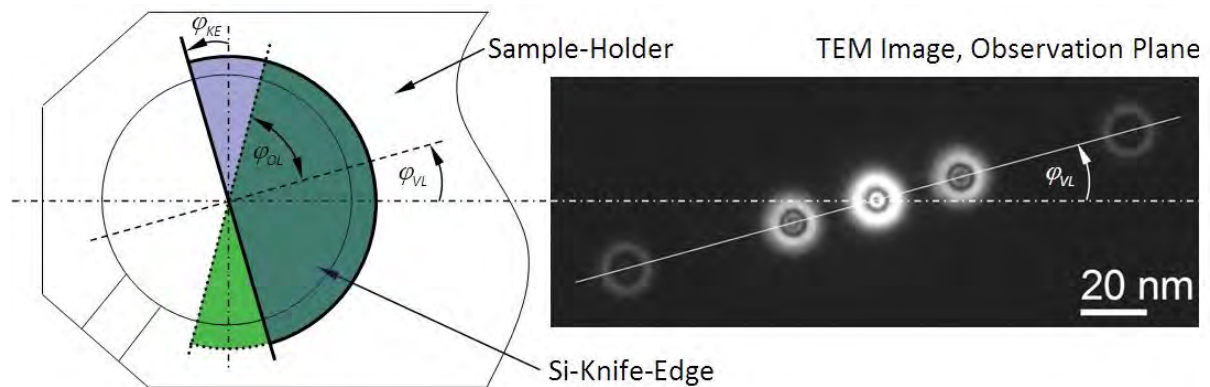


Figure 23: Left: The sketch shows schematically, how to align the KE in the TEM sample holder. The purple shaded KE belongs to its position, when looking at the back (far side of the beam) of the sample holder; the greenish KE represents its position, when turning the sample holder upside down, such that the beam facing side is now up. Right: Shows the connection between the TEM image and the positioning of the edge in the sample holder.

Now, that the electron beam is partially blocked, its radial symmetry is broken. Thus depending on the distance to the focal position  $z_f$ , it resembles an intensity distribution close to a semi-circle for  $z$ -values above  $\sim 30 \mu\text{m}$  and a half-moon for lower  $z$ -values. As this semi-circle electron beam or shadow image of the KE propagates down the column, its interaction with the magnetic OL field, indicated as a red arrow in Figure 22, induces an azimuthal rotation. This rotation adds up until the EVB reach the observation plane approximately 2.5 to 11.5  $\mu\text{m}$  above or below the focal position. There, the azimuthal angles can be measured for each vortex order as they are all well separated in

this plane, see Figure 22 or Figure 23, right. A sound working distance between the observation plane and the focal position turned out to be  $z_f = \pm 5 \mu\text{m}$ . For lower  $z_f$  values the size of the EVB renders accurate azimuthal angle measurements of the order of half a degree impossible. In contrast to that, the strong Gouy-phase influence, visible via high rotation angle offsets, poses no problems, as they can simply be subtracted. On the other side, for higher  $z_f$  values, e.g. roughly greater than  $12 \mu\text{m}$ , especially the first vortex orders begin to overlap, such that the tails of their half moon like intensity distribution can not be easily distinguished, and in so, making an angle measurement also very challenging. When the KE is placed directly in the observation plane, all cutting angles should be equal to  $\varphi_{VL}$  as the propagation distance and thus, the acquired azimuthal angle increase is zero.

After imaging the electron distribution in the observation plane, it converges further down the column, reaching the upper Rayleigh range, approximately  $1 \mu\text{m}$  above the focal position and the focal position itself, where the single diffraction orders reach their minimal radial extent. From then on the beam diverges to the lower Rayleigh range, propagating further down the column. As will be shown in the following sections, e.g. Figure 40, the electron beam undergoes a rotation of nearly  $180^\circ$  traversing the beam waist region.

One important aspect of the chosen experimental setup is, that in the course of one experiment no changes on the illuminating-, projecting- as well as imaging lens system are applied. This guarantees that all electrons are exposed to stable conditions and “see” the same magnetic field, such that no overall image rotation occurs. For instance,  $\varphi_{VL}$  does not change, no sudden offsets angles are introduced due to varying  $z_f$  values, as well as the LS parameter  $w_M$  also stays as it is.

#### 3.1.3 Electron Beam Cutting

When trying to observe fast Gouy-phase rotations of photonic beams, exhibiting waist radii of roughly  $1 \mu\text{m}$ , cutting is a rather trivial straight forward matter. But when arriving at nanometre beam sizes and rotation angles differences of half a degree are of interest, the situation changes completely.

The surface roughness of the cutting edge becomes a crucial parameter, just as the cutting procedure by itself, as will be argued in the following.

When the size of the object to cut gets of the order of the surface irregularities, the introduced angle deviations from this surface get significantly larger than the expected rotation angles, as can be schematically seen in Figure 24. Thereby, not only shifting the beam relative to the KE, see Figure 24,

left, or, more relevantly for the experiment, shifting the KE relative to the beam, would introduce errors, but also converging the beam down to the size of a few nanometres for z-shift values slightly above the observation plane, poses a source of angle measurement errors, see Figure 24, right. Note, that the LS are expected to occur at beam radii of  $w_M = 37.2$  nm.

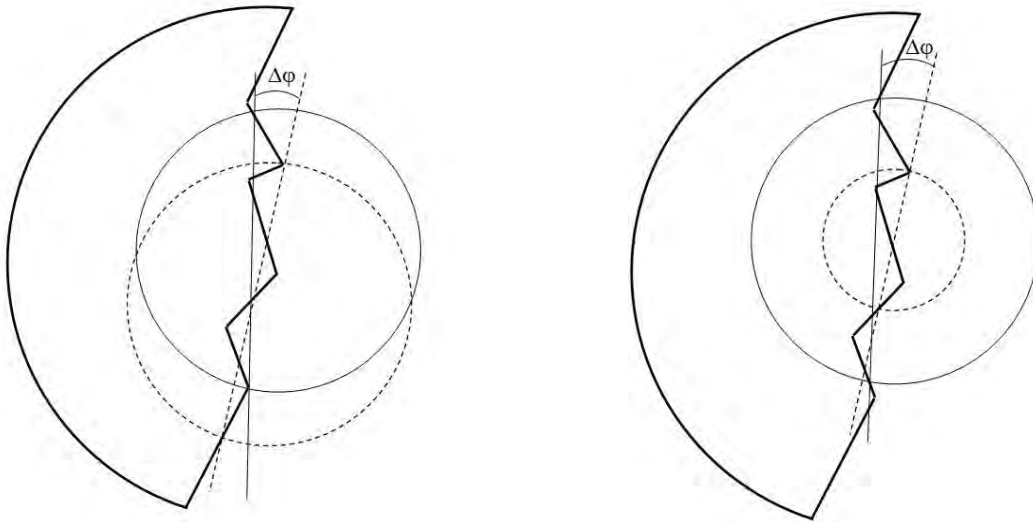


Figure 24: Schematic drawing to illustrate azimuthal angle errors introduced by, left: beam or stage drift and right: different z-shift heights. Thick line object represents the cutting edge, thin line circles represent the incoming beam and thin lines correspond to the measured azimuthal cutting angle.

Looking at the surface roughness of mechanical milling or polishing techniques like honing and lapping, which are of the order of a few tens of nanometres (peak-to-peak surface roughness,  $R_z \approx 25$  nm) proves that Figure 24 is not far off the scale (Schmitt-Measurement-Systems 2000, Mitutoyo 2008). Even when using FIB processed surfaces, the introduced irregularities cannot be made smoother than  $R_z \approx 5$  nm, due to drifting, occurring at least when milling micrometer scale objects, which would be necessary for these experiments (Steiger-Thirfield 2013). Besides, the commonly used semi-conducting wafer material silicon (Si) seems to improve the situation strongly. Here, the average surface roughness of polished single crystal wafers is approximately a third of a nanometre and  $R_z \approx 0.4$  nm (Teichert, MacKay et al. 1995, Schmitt-Measurement-Systems 2000).

Using a simple model for the estimation of the introduced angle errors in the form of  $\varphi_{KE-error} = \arctan((R_z / 2) / \rho(z))$ , where  $R_z$  represents the peak-to-peak surface roughness, clearly shows, that only the silicon wafer provides the needed smoothness to keep the angular deviation below half a degree over the z-shift range of interest (approximately 30 to 350  $\mu\text{m}$ ), see Figure 25. So the use of a Si-wafer as a KE addresses both issues equally well, if a sufficiently large region on such a Si-KE can be found. KE- or beam shift, as well as decreasing beam sizes for lower z-shift values would



not significantly infer the measured azimuthal angles. Now that the right material is found the question arises, how to prepare it for the EVB cutting experiments without damaging the smooth surface and at the same time producing a knife like structure. – A very crude, but simple mean to realize that is to break a Si-wafer along a low indexed crystallographic plane, such that the smooth breaking edge can be directly used to cut the EVB, without the need for any further processing.

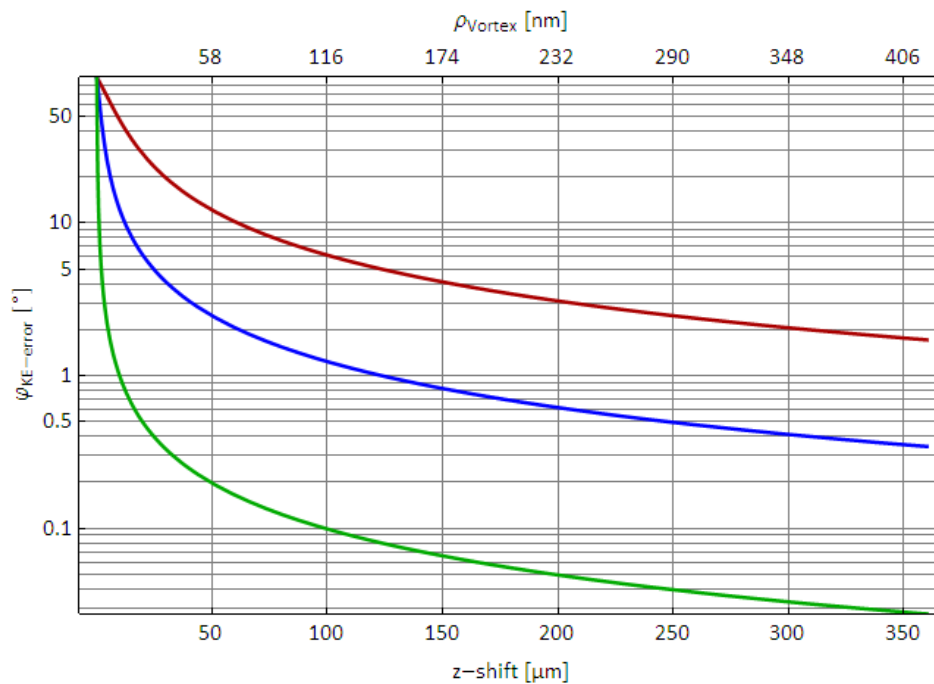


Figure 25: Angle error estimation over the z-shift and vortex radius for different surface roughnesses. Red: Mechanical surface processing,  $R_z \approx 25$  nm, blue: FIB milling:  $R_z \approx 5$  nm and green: polished Si-Wafer,  $R_z \approx 0.4$  nm.

Si crystallises in a diamond cubic crystal structure with a lattice spacing: 0.54 nm (O'Mara 1990) and standard Si-wafers are delivered in  $\langle 100 \rangle$ ,  $\langle 110 \rangle$  or  $\langle 111 \rangle$  direction. When taking a Si-wafer oriented in  $\langle 100 \rangle$  direction, the breaking edge should create an acute angle  $\Phi_{KE} = 54.7^\circ$  with the wafer surface. In principle this would resemble a nice cutting edge, but as illustrated in Figure 26, left, higher angles would be favourable, as the cutting of the electron beam would take place more rapidly, and in so leading to better pronounced EVB cutting edges, Figure 26, right. Tilting of the sample holder would be one possibility to enhance  $\Phi_{KE}$  but proper horizontal cutting of all EVB orders would be problematic.

Another option is to use  $\langle 111 \rangle$  grown Si-wafers, their crystal structure is tilted by  $54.7^\circ$ . Because of that, the breaking should occur along the  $(\bar{1}11)$ ,  $(\bar{1}\bar{1}\bar{1})$  or  $(11\bar{1})$ -plane creating an angle of  $\Phi_{KE} = 70.5^\circ$  with the wafer surface (Oosterbroek, Berenschot et al. 2000).

The Si-KE was produced gluing a 10 by 10 mm piece of a standard  $\langle 111 \rangle$ -Si-wafer of 300  $\mu\text{m}$  thickness onto a glass slide using hot wax. The glass slide had been glued onto the metal support of a Gatan ultrasonic drill before. Then under permanent dropping of a mixture of Silicon-Carbide-particles (SiC) and water a few 3 mm in diameter Si-wafer disks were bored out.

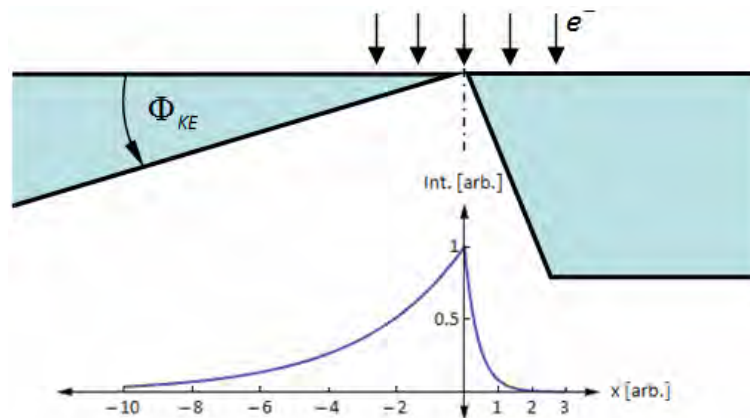


Figure 26: Schematic sketch showing the influence of the breaking edge angle  $\Phi_{KE}$  on the intensity drop of the incident electron beam and thus cutting quality of the KE.

Afterwards these were washed with water, acetone and finally with methanol placed in the ultrasonic bath for about a minute, to get rid of the SiC-particles and boring debris. The methanol, respectively ethanol washing in the ultrasonic bath is necessary to get rid of the acetone residues.



Figure 27: Left: Side view SEM picture of the Si-KE. The red arrow shows the FIB milled region, where the determination of the KE angle took place. At the same time this is the region where the experiments were conducted. Right: SEM picture showing the thickness of the cutting edge, as well as two different regions on the breaking edge face.

### 3 Methods

---

The next step was to break the 3 mm Si-disks into pieces, quite similar as it is done with floor tiles, by placing half of a disk onto a 1 mm thick glass object slide and holding this side firmly down with a pair of tweezers. At the same time force was applied to the free standing other side, such that it breaks roughly along the object slide edge.

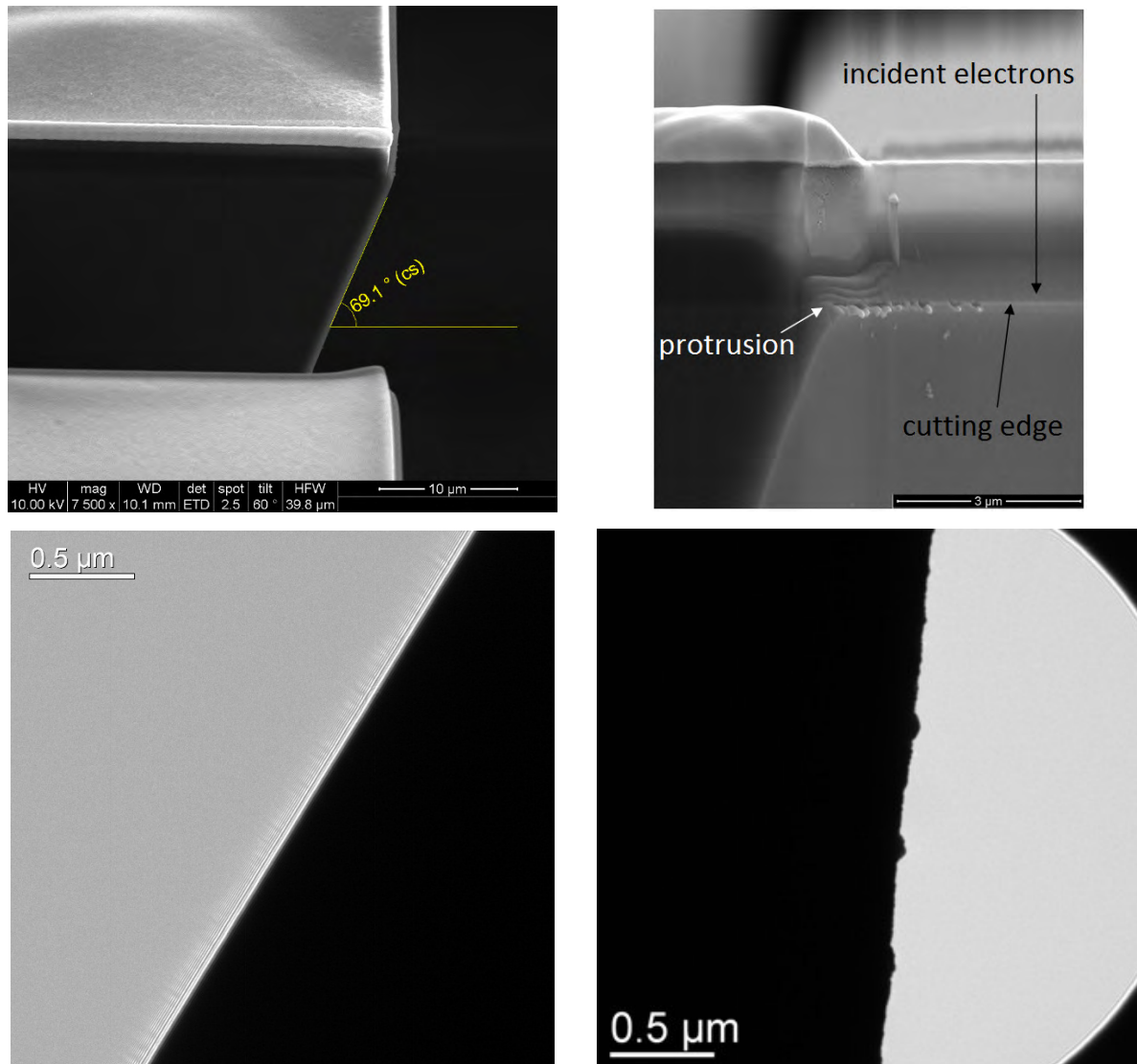


Figure 28: Upper panel: left: SEM side view of the Si-KE region marked with a red arrow in Figure 27, left, showing the angle of bevel being 69.1°, right: SEM close-up side view of the Si-KE showing a protrusion of 2.3 μm proving that the crystalline Si-wafer is acting as a KE not the Silicon-Dioxide (SiO<sub>2</sub>) cover layer. Lower panel: Comparison between a Si-KE left and right a 100 μm TEM aperture that was also used to cut the EVB. The TEM images clearly reveal the superior smoothness (measured  $R_z < 0.9$  nm) of the Si-KE relative to the 100 μm aperture (measured  $R_z < 40$  nm).

Then a Si-wafer fragment appropriate in size and cutting edge proportions was selected under a light microscope. And finally the above mentioned washing procedure was repeated with that fragment.

An SEM overview picture of the Si-fragment that was used as KE throughout the experiments is shown in Figure 27, left. Figure 27, right, depicts the frontal view of the breaking edge. A 120  $\mu\text{m}$  broad region can be seen that exhibits no obvious features that would influence the EVB on their way passing by and partially through the KE.

The following 180  $\mu\text{m}$  do show a landscape full of crests, which are actually also not interfering with the electron beam because of their backward displacement. Keep in mind that the convergence angle is of the order of one mrad or  $0.06^\circ$ . This circumstance was also checked in the SEM by tilting the Si-KE until rough structures protruded the smooth edge; these were most likely the crests visible in the lower part of the KE in Figure 27, right. The tilt angle was clearly smaller than the measured bevel angle in Figure 28, upper panel, left, but of the order of a few degrees and with that still two orders larger than the above mentioned convergence angle.

In early stages, also Cr sputtered glass slides, as well as an Ag/Pd layer on the broken Si-wafer fragment were tested, but all this trials did not come close to the smoothness of the non coated Si-KE, given in Figure 27 and Figure 28.

FIB milling was used to cut a 25  $\mu\text{m}$  deep groove into the KE in order to determine the geometry of the Si-KE, see Figure 27. As shown in Figure 28, upper panel, left,  $\Phi_{KE}^{mea} = 69.1^\circ$  fits well to the expected value  $\Phi_{KE} = 70.5^\circ$ . Figure 28, upper panel, left, also reveals a more complex cutting edge topology, which is also shown in more detail in Figure 28, upper panel, right. There, a surface layer covering the bulk material of the wafer of a thickness of 2.35  $\mu\text{m}$  is visible. An energy dispersive x-ray (EDX) analysis identified the layer as  $\text{SiO}_2$ . This, most likely amorphous, layer would not show the same breaking edge smoothness as crystalline Si. But, the same picture also reveals that the bulk material forms a nose like protrusion of 2.3  $\mu\text{m}$  width. The protrusion dimensions were determined on another micrograph not shown here. Taking into account that the radius of the EVB at z-shifts of  $\pm 350 \mu\text{m}$  is about 400 nm and by that only the very first part of the 2.3  $\mu\text{m}$  protrusion is irradiated by the electron beam, this shows that the Si-wafer fragment, indeed broke in a way, such it can be used as a KE. This was further confirmed in the TEM, see Figure 28, lower panel, there, the Si-KE was compared to a standard 100  $\mu\text{m}$  TEM aperture. The TEM image clearly shows the superior smoothness of the manually cleaved monocrystalline Si-wafer, with a measured  $R_z < 0.9 \text{ nm}$  as opposed to the aperture, which exhibits a peak to peak surface roughness of  $R_z < 40 \text{ nm}$ . The depicted Si-KE was then used throughout the most experiments. The 100  $\mu\text{m}$  TEM aperture was also tried out as a KE, but did not perform well.

Charging of the Si-KE posed no problem as for one, the electron beam currents were relatively low due to high spot sizes used, and for the other, Si-wafer material is nominally n-, or p-doped, such that

impinging electrons could be carried away. The EDX analysis mentioned above also revealed that traces of phosphorous are present in the Si-KE indicating n-doping.

#### **3.1.4 Experimental Procedure – Cutting the Line of Electron Vortices Step by Step**

Here, a step by step description of the sequence acquiring the vortex rotation data on the TEM will be given.

- Before the Si-KE can be put into the single tilt holder, the angle  $\varphi_{VL}$  has to be determined. Assuming the microscope has been aligned sufficiently well to create EVB by inserting the holographic vortex aperture; one can take an image of the row of vortices and measure their angle to the horizontal line. Actually the OL excitation has to be roughly set to the value used later on in the experiment itself; in many experiments the eucentric focus excitation was used.
- Now the Si-KE has to be put correctly into the single tilt holder, using the sketch and formula given in the preceding section.  $\varphi_{OL}$  has to be determined before, as it will be different depending on the type of TEM and OL lens used. This can be done by measuring the difference angle between the KE inserted into the holder, for example aligned parallel to the tilting axes, and its image under parallel illumination.
- Now, the single tilt holder with the Si-KE can be inserted into the TEM.
- Then the Si-KE has to be found and brought to eucentric height.
- The Si-KE will not exhibit perfect smoothness along the whole breaking edge, therefore a region has to be identified, where it is sufficiently smooth on a length scale of a few micrometers.
- As soon as this place has been found, a thorough beam and OL alignment should be done. Also the Si-KE eucentric height should be checked again, and if ok, the z-shift value can be set to zero, as this will be the observation plane. The click box “z-shift is relative” at the stage control window should be marked and the stage position can be saved.
- Here, the holographic vortex mask has to be inserted (again). The Si-KE should be moved out of the beam.
- The magnification can now be chosen such that the desired vortex orders are visible, at least  $m = \pm 1, \pm 3$ .
- At this point, it can be easily checked if the Si-KE alignment is correct by strongly defocusing the EVB with the C2 excitation and moving the Si-KE back into the beam. If the negative and positive vortex orders disappear at approximately the same rate, the Si-KE alignment in the sample holder is ok, if not, it has to be corrected and retried, until it cuts all visible vortex beam orders evenly.

- Then the C2 defocus can be reduced, such that the EVB show the appropriate size, the OL must not be changed here and for the following steps. Concerning the size of the different EVB orders, they should be as large as possible but at the same time they should not overlap with each other.
- The next step is moving the Si-KE into the EVB, until half of them is blocked, it could be useful to cut a little bit less than half of the EVB, because then a very sharp reference feature in the  $m = 0$  order shows up, which can be used as a guide to the eye for further cutting at different z-shift values. No matter if this guide to the eye is used or not, it is crucial that for all different z-shift value cuts, the intensity distributions look similar, apart from their azimuthal rotation and diffraction effects at low z-shift values. It should be avoided to cut, once, more than half of the beams and for another z value less than a half. And in principle cutting the EVB at  $z = 0$  is problematic, as the KE is not perfectly electron intransparent right from the beginning, see Figure 26, Figure 27 and Figure 28, such that the theoretical expected equal azimuthal cutting angle for all vortex orders is hard to observe.
- Now, the first experimental image can be recorded. The EVB should be aligned such that the same amounts of positive and negative vortex orders are centred on the CCD. As the intensity drops rapidly with increasing  $m$ , binning was used to get enough signal from higher vortex orders at reasonable recording times. However, to be still able to resolve faint rotations the pixel size should be approximately 0.15 nm or better, for vortices of 12 nm diameter in the observation plane. The explanation for this upper bound value will be given in the next section.
- Then the Si-KE should be moved out of the beam again. It is important to minimise beam on Si-KE time at least when working at z-shift values smaller than 100  $\mu\text{m}$ , because of KE contamination. To further minimize the contamination probability, the washing procedure mentioned in the preceding section with the additional use of a Helium-plasma-cleaner should be repeated before the experiment.
- As for now, the stage can be moved to the next z-shift value by typing the desired z value in the stage control panel. To observe azimuthal rotation dynamics of LS-LG modes, first the z-value spacing should be as minimal as possible, and second this minimal spacing should be used at and around the z-shift region, where the EVB spread in size to the mode dependent radial maxima of Landau-LG modes, described in section 2.1.5. The minimal z-value spacing used was 10  $\mu\text{m}$ , which leads to expected angular changes of the order of half a degree, which is roughly the lower detection limit. For a semi-convergence angle of 1.16 mrad the z-shift region where the LZG-phase effects are expected is approximately 30 to 80  $\mu\text{m}$  for lower vortex orders. Far off that region, the z-value spacing can be elevated, e.g. 25 to 50  $\mu\text{m}$ .

- Step 11 to 14 have to be repeated until the maximum z-shift range of the stage is reached, e.g. for the TF20  $\pm 375 \mu\text{m}$ .
- After the whole z-shift series has been recorded, the defocus value of the observation plane has to be determined. This can be done by utilizing the fact that the azimuthal rotation angle of cut vortices is normal to the line of vortices when positioning the KE at the focal point. By that z-shifting the KE until this condition is met gives the defocus value of the observation plane which was set to  $z = 0$  prior to the experiment.

#### 3.1.5 Azimuthal Angle Determination

In this section the azimuthal angle determination of the acquired data in the experiments described above will be governed in detail.

Therefore, it is instructive to start with a short introduction to the image analysis software provided from Gatan called “Digital Micrograph 3” (DM3) Version: 3.9.5.

Figure 29 gives an impression of the graphical user interface, which is basically divided into two main parts, the working area, where the experimental data is displayed and analysed and the toolbars and control menus on the left and upper side of the display. The two main image adjustment features that were used for the vortex rotation analysis were the gamma- and contrast control. The angle measurement itself was done using the readout values of drawn lines in the lower left corner. DM3 uses an own image file format called “.dm3”, which stores the electron counts in an array of 16 bit greyscale values with metadata including microscope and image information, in contrast to standard image formats like “.jpeg” or “.bmp”. Except DM3 and the image processing and analysis program “ImageJ” other image manipulation software cannot handle this format (UniblueSystems 2013). The gamma-controller changes the  $\gamma$ -value, such that the input picture data  $I_{in}$  is manipulated according to the power law  $I_{out} = I_{in}^\gamma$ , where  $I_{out}$  stands for the output image data. The intensity range is given by  $0 \leq I_{in,out} \leq 1$ . Depending on the  $\gamma$ -value, one speaks of gamma compression, for  $\gamma < 1$  and gamma expansion for  $\gamma > 1$ . Gamma compression enhances the appearance of low image intensities, whereas gamma expansion strongly damps them, such that high intensity areas in the image are pronounced; see the examples given in Figure 29 in the working area. Note that the DM3 gamma-controller scales the  $\gamma$ -value from zero to one, where “0.5” means  $\gamma = 1$ , “0” represents large gamma expansion  $\gamma \gg 1$  and “1” stands for strong gamma compression  $\gamma \ll 1$ . Contrast is defined as the intensity difference in an image as a whole or in juxtaposing regions by the expression  $(I_{max} - I_{min}) / (I_{max} + I_{min})$ , where  $I_{max}$  and  $I_{min}$  represent the global or local intensity maximum,

respectively minimum. The presence of contrast is fundamental in detecting objects and interaction. High contrast images appear crispy and brilliant, as against, low contrast images look dull and weak, rendering accurate (angle) measurements impossible; see the example given in Figure 29.

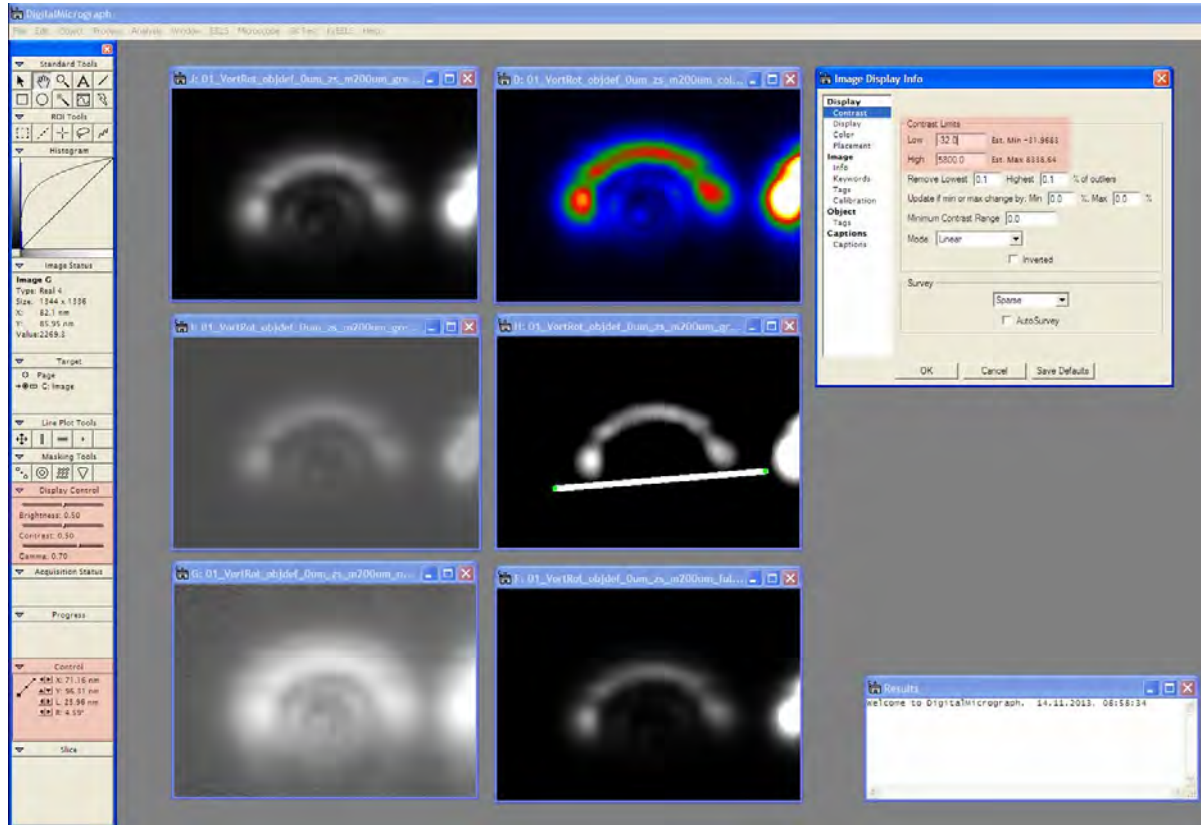


Figure 29: Shows a screenshot of the image analysis software DM3. The “Display Control”-panel with gamma and contrast controllers, the “Control”-panel with line coordinates and rotation angle output and the “Image Display Info”-Window with contrast adjustment boxes are highlighted. The working area shows experimental data of a single cut-vortex order, in different conditions: upper left image, raw as recorded, upper right, different colour scaling, middle left, low contrast, middle right, high contrast, lower left gamma compression and lower right gamma expansion.

DM3 offers a few possibilities to adjust and enhance contrast, as for example the contrast controller in the toolbox area and the “Image Display Info Window”, with contrast adjustment boxes, where the contrast limits can be chosen. Another possibility is to use different colour scaling to enhance contrast. These “instruments” were actually essential to gain the necessary angular resolution to resolve EVB azimuthal rotations. In Figure 30 three different contrast levels of a single vortex order are given for two different z-values, to show that initially not or hardly distinguishable changes of the azimuthal rotation angle become “visible” when using a colour scale or even better strong gamma expansion and contrast level adjustment to enhance the contrast. The last-mentioned method drops the resolvable angle below a degree, by converting smooth indefinite greyscale cutting edges into



sharp clearly defined edges, e.g. the azimuthal angles for the two 25  $\mu\text{m}$  separated vortices in Figure 30 differ by  $\sim 0.8^\circ$ .

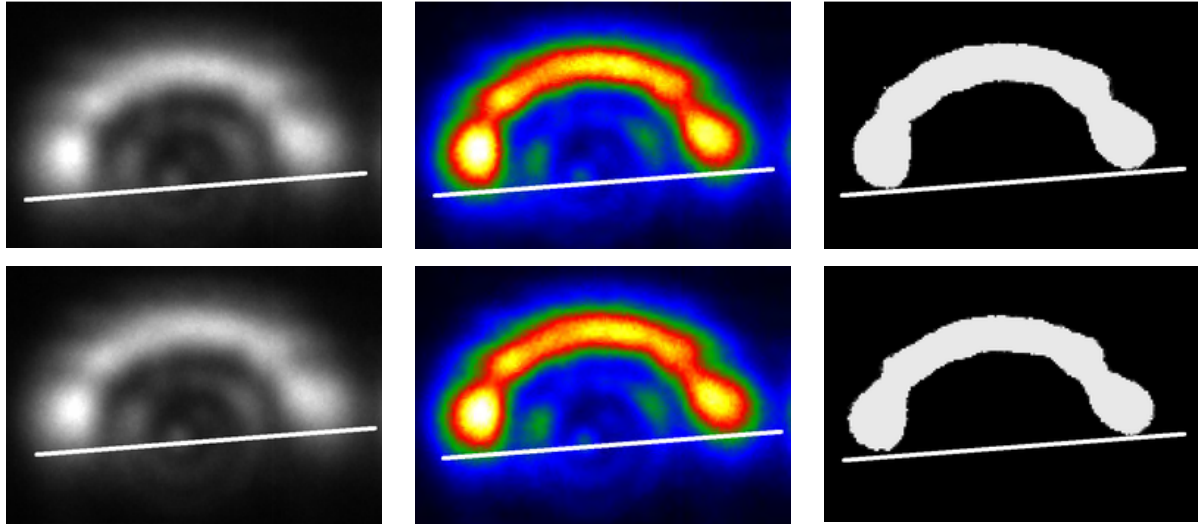


Figure 30: Compares three different contrast levels of a single vortex order to give an impression of the angle determination limits. The upper row image has been taken at  $z = -200 \mu\text{m}$  and the lower row one at  $z = -225 \mu\text{m}$ . The first column depicts the cut vortices as they were recorded in greyscale contrast. The cutting edges are blurred out and make angle determination difficult; the achievable angular resolution is of the order of a few degrees. Colour scale contrast in the second column improves the situation, down to single degree resolution. But only strong gamma expansion and contrast adoption in the last column gives a kind of “binary-coded” image, which provides sharp distinction of azimuth angles below a degree, such that the expected (clockwise) rotation of about  $0.8^\circ$  gets clearly visible.

This procedure literally takes single data slices on specific intensity levels out of the image data, see Figure 31. An issue arises when comparing different experimental images of one series, there the intensity varies due to the  $z$ -position of the KE and the degree of cutting the EVB, see Figure 31.

The black plane intersects a single vortex order at a certain intensity which results in a distinct structure and azimuthal rotation angle, doing the same for longer exposure times or a slightly different degree of cutting at the same  $z$ -value, this would lead to a different image slice structure and more importantly, to a different azimuthal rotation angle because the slopes of the cutting edge onsets differ. This is possibly due to Fresnel-diffraction or other electron-KE interaction effects, which are beyond the scope of this work. In order to avoid this effect, it is crucial to shift the contrast limits to a value where the image “slices” show similar structure and features, see Figure 30, last column and Figure 31.

As the azimuthal angle of rotation is determined by laying straight lines alongside the cutting-edges onsets, the radial distance where these lines “touch” the edge onset must not vary between different

z-value measurements. This is mentioned here, because typically the half-moon-like cut vortex orders are arranged in onion-like “layers” due to diffraction, with one “layer” being the most intense; see Figure 30, first and second column, and the inset in Figure 32.

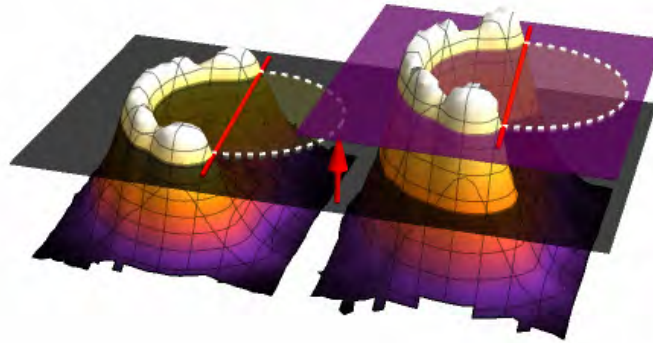


Figure 31: Two intensity distributions of cut EVB with different maximum intensities are shown in 3-dimensional representation, which should graphically explain the two most important parameters for azimuthal angle determination by laying straight lines alongside the cutting-edges. The black plane represents the contrast limiting level, which in combination with strong gamma expansion, cuts out a definite “intensity-slice”, in order to adjust to varying intensities of EVB, the contrast limit has to be adjusted, indicated by the lifted purple plane, which is the first parameter. The second one is the chosen radius where the line touches the cutting-edge onsets. Due to the strong radial dependence of the azimuthal rotations, it is crucial to compare only same radii, as indicated by the white dashed circles.

Typically this “layer” was analysed, but in principle every visible layer could be taken, as long only same “layers” are compared for different z-values. Electron beams carrying initial angular momentum or topological charge exhibit strong radial dependence of the azimuthal rotation angle, according to equation (2.14), as a result the “layers” are rotated against each other by an angle, typically much larger than the expected LR, thus introducing errors when mixed up.

To quantify the angular resolution limits of this visual judgement method, Figure 32 shows an enlarged view of a single electron vortex order with single pixels filled red, according to a certain intensity threshold. There, two yellow straight lines indicate the angular spread of a single pixel on the right side of the half-moon like cut vortex, when starting at the left side of it. The diameter of the shown measured vortex order is about 12 nm, which is just like the pixel size of  $p_s = 0.15$  nm a typical value for the experiments done. These two lines are easily separable by eye and create an angle of  $\Delta\varphi_{\text{pixel}} = 0.7^\circ$ . Further on, the well separable orange bisector creating an angle of  $0.35^\circ$  with its yellow “neighbours” is shown, indicating an angular resolution limit at least as low as  $0.35^\circ$  for a single pixel. Expanding this to multiple pixels or in other words optically integrating over a range of

different radii (about 3 to 5 pixel), as it is normally done for extended half-moon like intensity distributions, the lower limit of resolvable angles by eye can be given to be  $\Delta\varphi_{\min} = 0.15^\circ$ , at least when guided by high contrast edges, as it is the case with the high contrast images given in Figure 30, in the last column. The minimum selectable angle difference in DM3 for annotations like the straight line is as low as  $0.01^\circ$ .

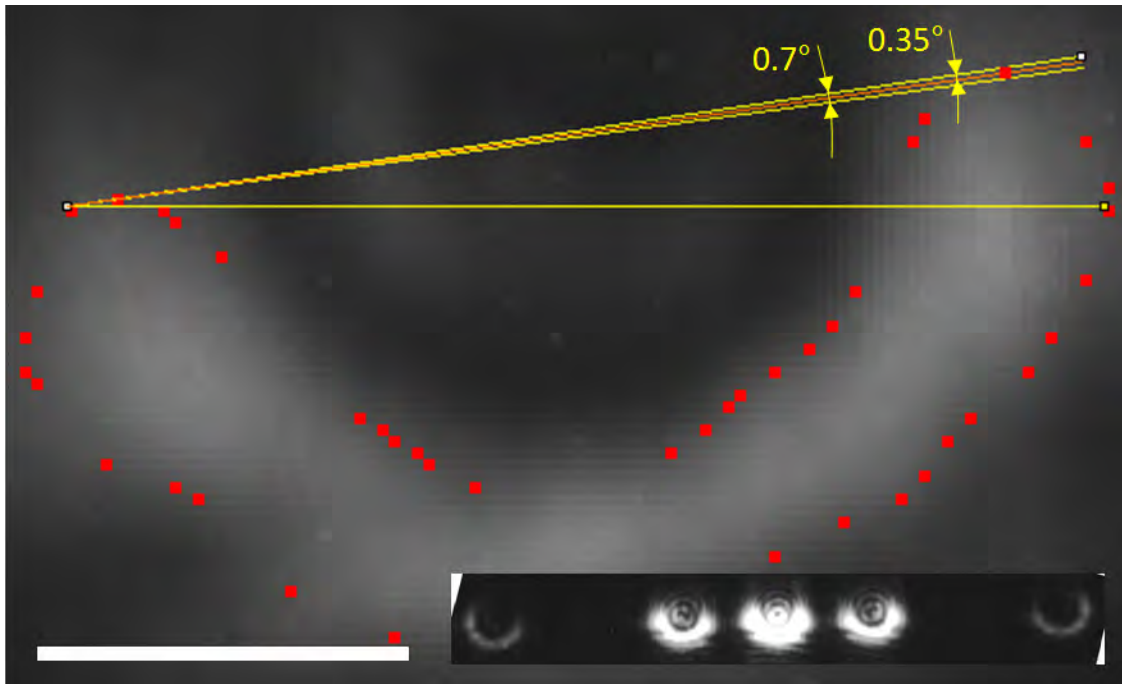


Figure 32: Depicts the angular spread of a single pixel and its bisector for a typical measurement by showing an enlarged view of a single cut-vortex, with some pixels filled red according to a certain intensity threshold value. The bisector is well separable by eye, indicating that the minimal readable azimuthal angle difference is lower than  $0.35^\circ$ . The inset shows the whole recorded image. The scale bar equals 5 nm. The pixel size is 0.15 nm.

Above, it was pointed out that a pixel size of 0.15 nm is sufficient to achieve an angle resolution well below  $0.35^\circ$ , a smaller pixel size would not significantly enhance the angular resolution. As a rule of thumb, the pixel size should be of the order of  $(2\rho_{EVB} \cdot \pi) / 240$ , with  $\rho_{EVB}$  being the radius of a single vortex order as shown in Figure 30, Figure 31 and Figure 32.

With a minimal azimuthal angle resolution of  $\Delta\varphi_{\min} = 0.15^\circ$  and an electron angular velocity in the magnetic OL field of  $\Delta\varphi / \Delta z = 0.0328 \text{ deg} / \mu\text{m}$ , the minimum z-value increment of the Si-KE to detect this rotation is roughly 5  $\mu\text{m}$ . Taking into account that the introduced error of the contrast limit adjusting procedure mentioned above also adds an error, which is estimated to be of the order of  $\Delta\varphi_{\min}$ , it is reasonable to choose the lowest difference between successive z-shift values equal or greater than 10  $\mu\text{m}$ . Using the colour scale contrast method the angle determination resolution is

worse, as well as the error through (wrong or missing) intensity adoption is larger. The minimal distance between successive z-shift values cannot be smaller than 25 to 50  $\mu\text{m}$ .

Note, that the measurement of azimuthal angles as low as  $0.15^\circ$  by visual inspection corresponds to a skew angle of the incident electrons of the order of  $\theta_{skew} = \arctan((2\rho_{EVB} \cdot \sin(\varphi(\Delta z)) / \Delta z) \approx 6.9 \mu\text{rad}$  for  $\rho_{EVB} = 6\text{nm}$ , see Figure 33. These angles are comparable to the electron beam deflection of electric fields inside a thin specimen of the order of some  $\text{meV/nm}$ , which are measured using a sophisticated STEM technique, called differential phase contrast (Lohr, Schregle et al. 2012).

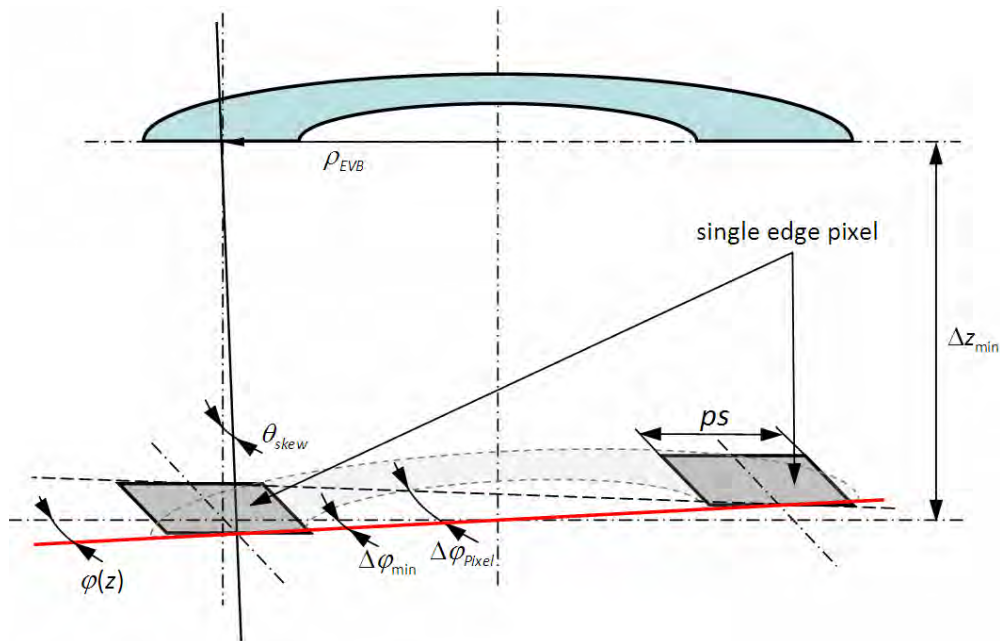


Figure 33: Sketch, showing the geometrical setup to determine the skew angle and minimum z-shift value increment.

With the above given procedure to determine azimuthal rotation angles, it should in principal be possible to resolve Larmor-, cyclotron- or no rotation behaviour of the EVB. As the determined azimuthal rotation angle varies depending on the chosen contrast limit, these results will only be valid relative to each other, not in an absolute sense. For that the two maxima at the beginning of the half-moon shapes, visible in Figure 30, middle column and Figure 31, could be taken as absolute cutting angles, but due to slight over- and undercutting at different z-shift values, not all images of a series exhibit those characteristic peaks, and in so, this absolute measure is sometimes misleading or even lost, leading to much higher error bars for the absolute value.

In addition, the angle determination error introduced by the stage z-shift positioning should be treated here. The relative z-shift or -height indication error is approximately three percent (Tiemeijer 2012). For low z-values this error is negligible, as the introduced angular deviation would be smaller

than  $\pm 0.01^\circ$  for Larmor- and  $\pm 0.02^\circ$  for cyclotron rotation. At higher  $z$ -values (about  $100\ \mu\text{m}$ ) this error becomes higher and introduces angular deviations of the order of  $\pm 0.1^\circ$  for Larmor- and  $\pm 0.2^\circ$  for cyclotron rotation.

Further, an azimuthal rotation of the Si-KE can be excluded due to the mechanical way of achieving the  $z$ -shift lifting action by tilting the whole sample holder. This changes the Si-KE cutting- or bevel angle by approximately  $0.09^\circ$ , which is negligible compared to the bevel angle of the KE of  $70^\circ$ . Lateral drift is also negligible, as it is of the order of  $1\ \text{nm/minute}$  with a standard holder (FEI-Company-Datasheet 2007).

#### **3.1.6 Numerical Simulation of the Vortex Rotation Experiment**

To deepen our understanding of the EVB propagation within the magnetic OL field, and to complement the findings of the semi classical analytical derivation in section 2.1.6, as well as the quantum mechanical wave propagation results (Floss 2013), a numerical ray tracing code was written to “rebuild” the vortex rotation experiment described above. Here, only a short general description of the program will be given with the basic equations of motion, initial conditions, such as the spatial distributions of electrons and their velocities, as well as the assignment of OAM and the actual mimicking of the experimental setup. For a more detailed description of the ray tracing program, see the authors project work on electron scattering on magnetic dipoles (Schachinger 2012).

The ray tracing code was realised in “Wolfram Mathematica 8”, version: 8.0.1.0, a software tool for mathematical computation. The underlying model was that of a point-like electrically charged particle, carrying a charge  $e$  and a mass  $m_e$ , which moves inside the magnetic OL field, a “Glaser-Glockenfeld” given by (2.1), obeying the LF (2.7). Consequentially, the second order ordinary differential equation of electron motion inside the magnetic field was numerically solved incorporating the built in function “NDSolve”, which uses, amongst others, Runge-Kutta algorithms to solve the given problem.

The electron ensemble, typically a few hundred, initially starts at the C2 aperture  $11\ \text{mm}$  above the centre of the bell-shaped OL field, reproducing the camera length of the condenser system. The electrons are randomly and homogeneously distributed over a circle  $8.4\ \mu\text{m}$  in diameter, coming close to the homogenous illumination of the holographic vortex mask described in section 3.1.1. The reduced illumination diameter was necessary to adapt the convergence angle of the particle beam to the one measured in the TEM. If this is a result of missing or wrong assumptions on the magnetic field distribution inside the TEM or is related to the centroid motion of the electron, according to the Ehrenfest theorem, cited in section 2.1.6, is an open question.

At an acceleration voltage of 200 kV the electron velocity in forward direction equals 0.695 times  $c$ . The EVB OAM was introduced by assigning each electron a azimuthal velocity according to equation (2.33). At the same time it is important to cancel the influence of the OL field at the initial electron position, as this would imprint much higher non-quantized OAM values to the electrons (Beck and Mills 1973). This is done by calculating the angular velocity at the starting position, at the radius of each electron with  $v_\varphi = \rho \cdot \dot{\varphi}$ , where  $\dot{\varphi}$  is given by the LR formula (2.14) for  $C = 0$ .

Realistic parameters for the OL “Glockenfeld” had to be estimated as the manufacturer did not publish them, due to intellectual property reasons. The estimation is based on personal communications with Josef Zweck and Peter Tiemeijer (Tiemeijer 2013, Zweck 2013), who could provide the maximum field strength, and on the calculation of the Glaser field FWHM given in section 2.1.2. These values were  $B_0 = 1.89$  T for the maximum field intensity at the centre of the OL field and a FWHM of  $2d = 6.02$  mm.

The simulation code calculates all electron trajectories, one after the other, and saves the whole trajectory  $(x, y, z)$ -coordinates and velocities  $(v_x, v_y, v_z)$  as lists, accessible via an interpolating function parameterised over the time  $t$ . Inserting the electron blocking KE can be simulated by selecting those trajectories, which did not “hit” the KE over their course through the OL. “Hitting” means that, at least one point of the electron trajectory lies within a predefined region of the size and position of the real KE, e.g. half of a cylinder with a radius of 25  $\mu\text{m}$  and a thickness of 2 to 10  $\mu\text{m}$ , positioned between  $z = \pm 500$   $\mu\text{m}$ . The experiment itself is then replicated by changing the  $z$ -shift value of the KE in the desired range and repeating the “hit”- or not “hit”-selection algorithm for each new KE  $z$ -shift value. To be able to compare the simulated data with the experiment, the electron positions, for electrons which did not “hit” the KE, were plotted in the observation plane for each  $z$ -shift value. Afterwards, an algorithm automatically determines the position of the edges of the cut vortices’ half-moon shape and calculates the azimuthal angle. The result is then plotted over the  $z$ -shift value of the KE.

### 3.2 Numerical Simulation of the proposed STOC-Device

As already mentioned in Karimis' and colleagues 2012 Physical Review Letters paper, the analytical solution to the full Pauli equation, describing the temporal evolution of the electron wavefunction including the spin-magnetic field interaction in the non-relativistic regime, cannot be found. As a result, there are two ways to describe the electron beams' propagation in such non-uniform field geometries like the quadrupole Wien filter (Karimi, Marrucci et al. 2012b). Classical dynamics suffice the given problem, such that either using a power expansion in  $\rho$  (Scheinfein 1989) or numerical ray tracing can be used.

For the time being, the latter option was chosen for two reasons. The proposal could be tested with no additional approximations, except the fringe fields, and the author had already build up a numerical ray tracing program, dealing with quite similar problems (Schachinger 2012).

Again for the general description of the ray tracing program the authors' 2012 project work can be studied, here, only the necessary adoptions to this code will be given.

Initially, all electrons are randomly distributed on a 20  $\mu\text{m}$  thick ring, with a mean radius of 100  $\mu\text{m}$  at  $z$  equals zero. Then the electrons propagate along the positive  $z$ -direction with a forward velocity of 0.55 times  $c$ , according to an acceleration voltage of 100 kV. To create an input EVB with quantised OAM the same assignment for the transverse velocity components as in the preceding section was used. After travelling 20 cm in  $z$ -direction, the electrons enter the quadrupole Wien filter, which has a length of  $\sim 1$  m. An elegant description of the quadrupole fields inside the Wien filter utilizes the  $q$ -plate expression (2.64) with  $q = -1$ , such that the magnetic field can be written as,

$$\mathbf{B}(\rho, \varphi, z) = B_0(\rho) \cdot \begin{pmatrix} \cos(\alpha(\varphi)) \\ \sin(\alpha(\varphi)) \\ 0 \end{pmatrix}, \quad (3.1)$$

with  $B_0(\rho) = B_0 \cdot \rho^{-q}$ . The electrical field shows identical structure, except that it is rotated by  $90^\circ$  with respect to the magnetic field. The field strength parameters  $B_0$  and  $E_0$  were chosen such that the field strengths  $|\mathbf{B}(\rho = 100\mu\text{m}, \varphi, z)| = 3.5\text{mT}$  and  $|\mathbf{E}(\rho = 100\mu\text{m}, \varphi, z)| = 575\text{kV} / \text{m}$  were met at a radius of 100  $\mu\text{m}$  inside the quadrupole Wien filter. Right after the passage of the simulated filtering device the electron positions, as well as their directions, were plotted as a real space map and as a reciprocal space map.

So far, only the ideal solely transverse quadrupole field inside the filter was given. In reality the electrodes and coils generating the electric, respectively, magnetic fields do create (longitudinal)

fringe fields at the entrance and exit of the proposed device. A simple approximation that was used by Karimi and co-workers to handle these fringe fields was the sharp-cut-off-fringe-fields (SCOFF) model. This model assumes that the transverse velocity components of the entering electrons remain constant and zero  $v_x = v_y = 0$  and that the fringe fields abruptly terminate. Such sharp rise of the potential exerts a strong force to the electrons in longitudinal direction, changing their z-direction velocity by,

$$v_z(x, y) = v_0 - \frac{e}{m_e \cdot v_0} \cdot \Phi(x, y) = v_0 - \frac{e}{m_e} \cdot A_z(x, y), \quad (3.2)$$

where  $v_0$  represents the initial electron forward velocity,  $\Phi(x, y)$  the electrode potential- and  $A_z(x, y)$  the vector potential distribution given by  $\Phi(x, y) = E_0(\rho(x, y)) \cdot (x \cdot \sin(\alpha) - y \cdot \cos(\alpha))$  and  $A(x, y) = B_0(\rho(x, y)) \cdot (0, 0, y \cdot \cos(\alpha) - x \cdot \sin(\alpha))$  (Karimi, Marrucci et al. 2012c).

In order to include the ES in the simulation, the equations of motion had to be extended by the force acting on a magnetic dipole given in expression (2.62), such that the whole force acting on the electrons now reads,

$$F = F_L + F_s = e \cdot (\mathbf{E} + \mathbf{v} \times \mathbf{B}) + \nabla(\boldsymbol{\mu} \cdot \mathbf{B}). \quad (3.3)$$

The temporal ES evolution was added to the simulation code by using the precession equation,

$$\frac{d\boldsymbol{\mu}}{dt} = \frac{g_e \cdot |e|}{2m_e} \cdot \mathbf{B} \times \boldsymbol{\mu}. \quad (3.4)$$



## 4 Results

### 4.1 Vortex Rotation Results

In this section the results of the various EVB rotation experiments will be presented. Before giving details on the EVB experiments itself, results of image rotation experiments with a copper (Cu)-grid and the parallel illuminated Si-KE will be shown.

#### 4.1.1 Image Rotation of a Cu-Grid on the Tecnai G20 LaB<sub>6</sub> TEM

A copper (Cu) grid with 450 nm spacing, actually used for calibration purposes, was inserted in the LaB<sub>6</sub> TEM to observe its rotation in the OL field, when moved from  $z = -500 \mu\text{m}$  to  $z = +200 \mu\text{m}$ , see Figure 34 for an excerpt of one measured series. For such a high range of  $z$ -shift values the image rotation becomes well visible, as indicated by the red arrows. It can be seen that by lifting the Cu-grid up the column, its image starts to rotate in the counter-clockwise (CC) direction, thus indicating that the electrons winding down the OL field in CC direction. With the left-hand-rule for electron motion in magnetic fields stemming from the LF (2.7) and formula (2.2) defining the direction of the radial field component of the OL, one can deduce that the  $z$ -component of the OL field  $B_z$  points up the column.

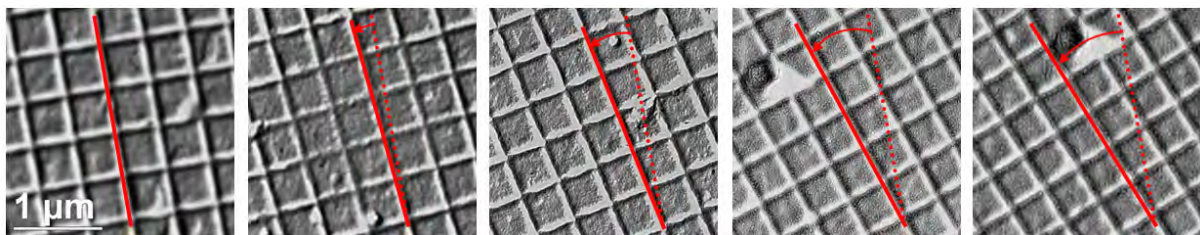


Figure 34: TEM images of a  $z$ -shift series of a Cu-grid at 92.8 % OL excitation and 48.5 % C2 excitation representing “parallel” illumination. The  $z$ -shift values range from  $-500 \mu\text{m}$  outermost left to  $+200 \mu\text{m}$ , at the outermost right side; the steps were  $-300 \mu\text{m}$ ,  $-100 \mu\text{m}$ ,  $+100 \mu\text{m}$ ,  $z = 0$  was defined as the eucentric height. CC rotation is well observable and indicates that  $B_z$  points up the column.

When measuring the azimuthal angles of this rotation  $\varphi$  for different  $z$ -values, it turns out that they increase linearly. Assuming that this image rotation is caused by the LF, it is possible to associate its slope  $\Delta\varphi/\Delta z$  not only to a magnetic field direction, but also to a magnetic field strength by

transforming equations (2.14) and (2.59) for LR to,

$$B_z(\varphi, \Delta z, v_{\parallel}) = \frac{\pi \cdot m_e \cdot v_{\parallel} \cdot \varphi \cdot \gamma}{90 \cdot e \cdot \Delta z}. \quad (4.1)$$

This expression for the z-component of the magnetic field inside the OL, depends on the relativistic forward velocity of the electron given by  $v_{\parallel} = c \cdot \sqrt{1 - 1/(1 + (e \cdot U/m_e c^2)^2)}$ , the travelled distance in z-direction between two successive measurements  $\Delta z = z_1 - z_2$  and finally on the azimuthal rotation angle of the Cu-grid  $\varphi$ , given in degree.  $\gamma = 1/\sqrt{1 - (v_{\parallel}/c)^2}$  is the Lorentz factor. Now, one can calculate the magnetic field in the region at and around the eucentic height of the OL by employing this formula. The azimuthal rotation angle in Figure 34 shows an estimated slope of  $(3.13 \pm 0.09)^\circ/100 \mu\text{m}$ , thus  $B_z = (1.80 \pm 0.05) \text{ T}$ .

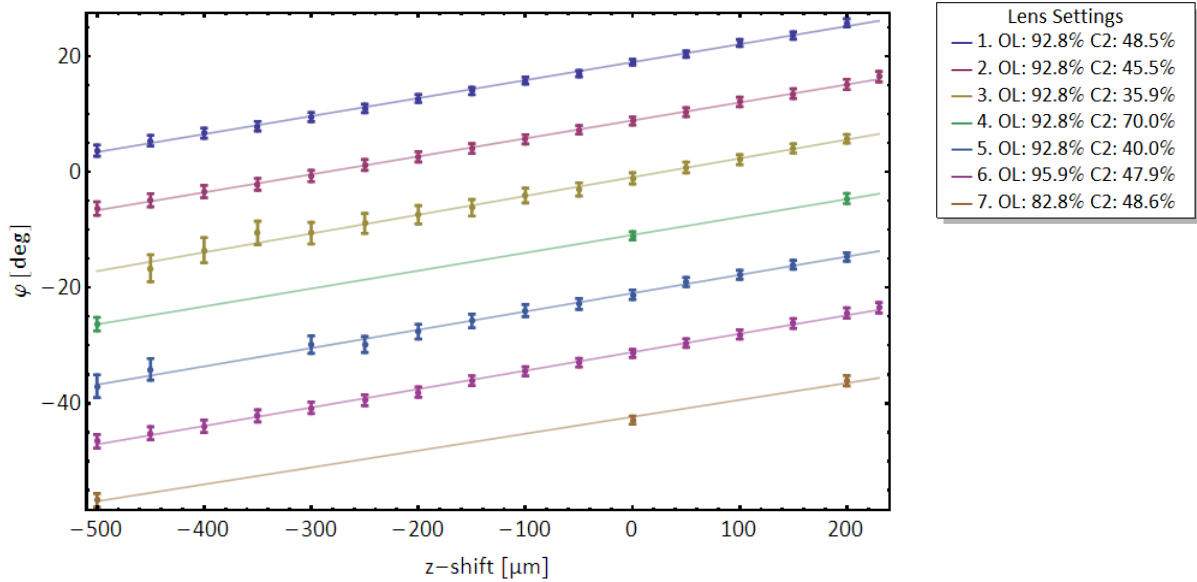


Figure 35: Shows the measured azimuthal rotation angle data of the Cu-grid z-shift series for different OL- and C2 excitations. The error bars depict the estimated reading error plus z-shift indication error of the stage. The offset was chosen arbitrarily for better visibility.

This experiment was repeated for different lens settings, to learn more about the influence of the second condenser lens on the image rotation, respectively the OL field, see Figure 35 for the whole data set. For example the first lens setting represents parallel illumination, the second 5.6 mrad convergent and over-focused illumination, the third -500  $\mu\text{m}$  under-focusing, the fourth strong over-focusing, the fifth -350  $\mu\text{m}$  under focusing, the sixth and seventh condition represent parallel illumination for higher, respectively lower OL excitation. It should be noted that the Cu-Grid was turned around between the first and second z-shift series, explaining the over-focus condition

despite the lower C2 value. Figure 35 qualitatively already shows, that there is little difference between the seven different lens settings as they are all nearly parallel. Even the last two conditions' slopes do not deviate visibly.

Nr.	Lens setting	$\bar{s}$ [°/100 $\mu$ m]	$\pm\Delta s$ [°/100 $\mu$ m]	$B_z$ [T]	$\pm\Delta B_z$ [T]	$\pm\Delta(s, B_z)$ [%]	$R^2$
1	OL: 92.8% C2: 48.5%	3,13	0,09	1,80	0,05	2,9	0,9982
2	OL: 92.8% C2: 45.5%	3,12	0,11	1,79	0,06	3,4	0,9993
3	OL: 92.8% C2: 35.9%	3,25	0,18	1,87	0,10	5,6	0,9955
4	OL: 92.8% C2: 70.0%	3,10	0,21	1,78	0,12	6,7	0,9998
5	OL: 92.8% C2: 40.0%	3,17	0,16	1,83	0,09	5,1	0,9961
6	OL: 95.9% C2: 47.9%	3,21	0,11	1,85	0,06	3,3	0,9984
7	OL: 82.8% C2: 48.6%	2,94	0,21	1,69	0,12	7,1	0,9959

Table 2: Lists the estimated slopes and OL field strengths with absolute and relative standard errors, as well as the  $R^2$  value for various lens settings gained from Cu-grid z-shift series image rotation measurements.  $\bar{s}$  denotes the estimated slope,  $\pm\Delta s$  the standard error,  $B_z$  the estimated OL-field,  $\pm\Delta B_z$  the standard error of the estimated OL-field and  $\pm\Delta(s, B_z)$  the relative standard error of the estimated OL-field and slope.

The quantitative analysis given in Table 2, and visualized in Figure 36, reproduces that first impression. That is, the estimated slopes  $\bar{s}$  for 92.8 % OL excitation do vary around a mean value of 3.15 °/100 $\mu$ m, given by the red line in Figure 36, by 1.9 %, but at the same time the standard errors for the estimated slopes range from 2.9 to 7.1 %. Such that there is no clear sign for a significant difference between the different C2 excitations. For the linear model fitting routine the reading errors in the range 0.5 to 0.7 °/100 $\mu$ m plus the estimated additional z-shift indication error were used as weighting factors. Even though a trend to faster, respectively lower rotational speeds is observable for higher, respectively lower OL excitations it cannot be clearly distinguished from the former mentioned, due to the “broad” error region. Nevertheless Josef Zweck reported that the magnetic field of a Tecnai TEM located in Eindhoven, NI, operated at 200kV and an OL excitation of 92.77% was measured to be 1.87 T (Zweck 2013). Additionally, Peter Tiemeijer, working at FEI, gave a simulated value for the T20 S-Twin OL of 1.89 T, at the sample, at eucentric height (Tiemeijer 2013). Assuming that the manufacturer did not change the lens design significantly this value fits reasonable well to the values gained herein, e.g. the mean magnetic field value of the five measurements taken at 92.8 % OL excitation is (1.82 $\pm$ 0.04) T. Also, the value of 1.87 T lies within the measurement uncertainty of three z-shift series, with a comparable OL-excitation and just slightly above it, of the other two. And in so, being a strong hint that the measured image rotation is due to the LF and can be coined LR.

In other words the influence of the OL/C2 excitation is negligibly when it comes to compare it with double Larmor- or cyclotron angular frequencies. Also the high  $R^2$ -value in Table 2, being 1 for data

perfectly fitting to a linear model exhibiting a certain slope, points out that assuming a quasi homogenous magnetic field  $B_z$  along the accessible z-shift region is reasonable.

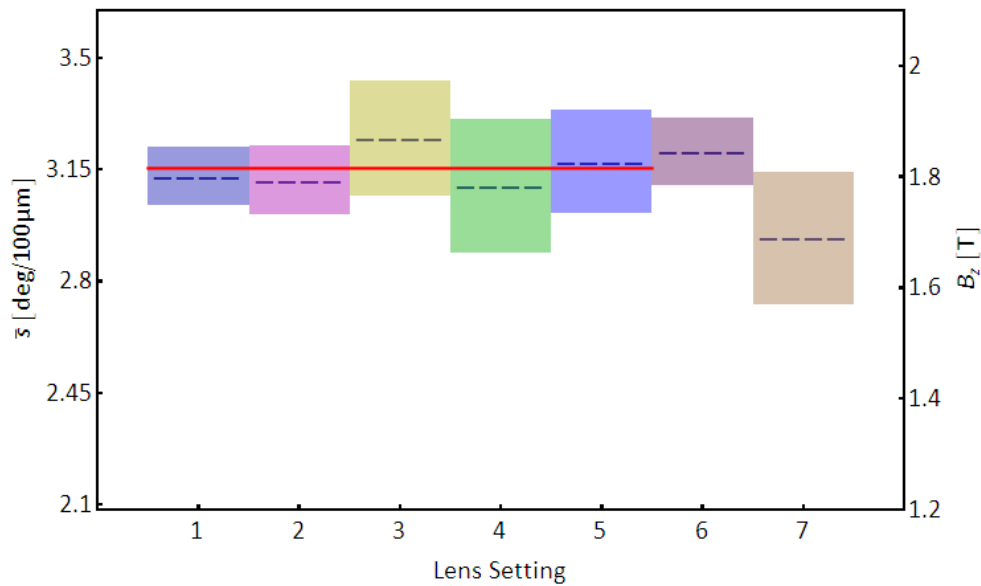


Figure 36: Visualisation of the estimated slopes  $\bar{s}$  and OL fields  $B_z$  with their standard errors, shown as colour shaded boxes, given in Table 2. The red line starting at lens setting one, ending at five, represents the mean of those estimated values and amounts to  $B_z = (1.815 \pm 0.035)$  T.

With an improved calibration of this method it could be used as a kind of magnetic field probe in the TEM with an accuracy better than 2.9 %.

#### 4.1.2 Image Rotation of a Silicon-Knife-Edge on the Tecnai F20 FEG TEM

The results of the preceding section have shown LR for non-vortex beams in the OL field, as well as that it is quasi independent of C2 excitation. As the vortex rotation experiments could only be done on a FEG equipped TEM, due to its high spatial coherence, the above given experiment, had to be repeated on this machine, in order to determine the rotational speeds of non-vortex beams for the OL excitations used in the vortex rotation experiments. And on the other hand, using the vortex cutting Si-KE under (nearly) parallel illumination, with its superior broken edge smoothness, could provide more reliable slopes and magnetic field data to compare with the measured and simulated field values from Eindhoven. This assumption proofed to be right as can be qualitatively seen in Figure 37. The azimuthal angle determination could be done with higher accuracy.

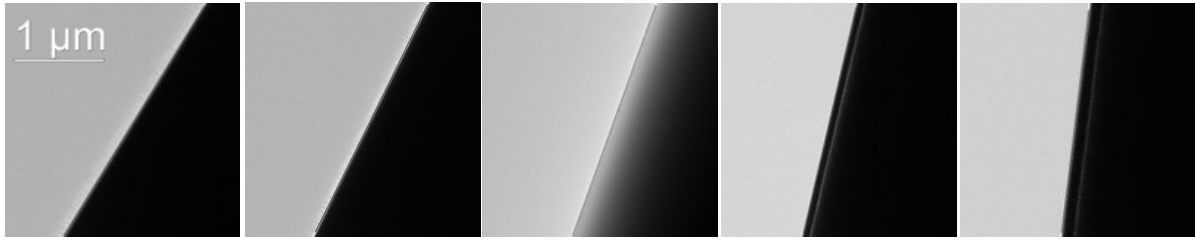


Figure 37: TEM image series of the Si-KE rotation experiment at 95.8% OL excitation and approximately parallel illumination, taken at z-shift values (from left to right) -370, -200, 0, +200, +380  $\mu\text{m}$ ,  $z = 0$  was defined as the eucentric height. CC rotation is well observable. Due to the smooth edge, accurate angle determination is possible.

The reading error was estimated to be as low as  $\pm 0.1^\circ$ , which was overruled by the stage z-shift positioning error for z-values greater than 100  $\mu\text{m}$ . Also the same CC rotation was observed, indicating the magnetic field points upward.

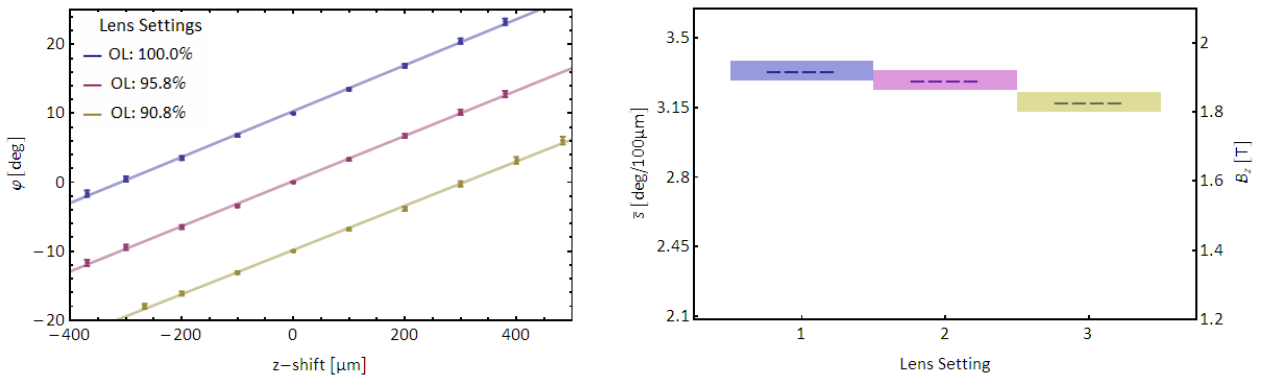


Figure 38: Left: Diagram shows the measured azimuthal rotation angle data of the Si-KE z-shift series for different OL excitations. The error bars depict the estimated reading error plus z-shift indication error of the stage. The offset was chosen arbitrarily for better visibility. The azimuthal angle  $\varphi$  plot range is much lower than in Figure 35, explaining the much higher slopes. Right: Visualisation of the estimated slopes  $\bar{s}$  and OL fields  $B_z$  with their standard errors, shown as colour shaded boxes, given in Table 3.

In Figure 38, the quantitative results of three z-shift series for OL excitation at the eucentric height, 100  $\mu\text{m}$  beyond and 85  $\mu\text{m}$  above are given. Even though the stage z-shift positioning error grows three times larger than the reading error, for z-values greater than 300  $\mu\text{m}$ , the smallest OL excitation can be well discriminated by the two larger ones, Figure 38, right. This is because the error bands could be reduced to a relative standard error of 1.5 to 1.6 %, see Table 3. The measured slope at the eucentric position at 95.8 % OL excitation of  $(3.29 \pm 0.05)^\circ/100\mu\text{m}$  indicates a higher magnetic field in the OL of  $(1.89 \pm 0.03)$  T, compared to that of the Cu-grid measurements, thus being exactly the simulated value of 1.89 T given above. It should be noted, that due to a different mechanical

mounting height of the stage in the FEG TEM, the OL-excitation for the eucentric height is 3 % higher. It is not known to the author, if the simulation used the lower or the higher OL excitation value as a eucentric focus value. Nevertheless, also the magnetic field value for 90.8% OL excitation of  $(1.83 \pm 0.03)$  T lies slightly above the mean value for the five Cu-grid measurements taken at 92.8 % OL excitation of  $(1.82 \pm 0.04)$  T, and with that pointing in the same direction.

Nr.	Lens setting	$\bar{s}$ [°/100 $\mu\text{m}$ ]	$\pm\Delta s$ [°/100 $\mu\text{m}$ ]	$B_z$ [T]	$\pm\Delta B_z$ [T]	$\pm\Delta(s, B_z)$ [%]	$R^2$
1	OL: 100.0%	3,33	0,05	1,92	0,03	1,5	0,9986
2	OL: 95.8%	3,29	0,05	1,89	0,03	1,5	0,9991
3	OL: 90.8%	3,18	0,05	1,83	0,03	1,6	0,9987

Table 3: Lists the estimated slopes and OL field strengths with absolute and relative standard errors, as well as the  $R^2$  value for three OL settings, acquired in z-shift series experiments with a Si-KE.

To sum it up, the use of the Si-KE improves the LR measurements significantly and provides better agreement between theory and measured magnetic field values. Additionally, LR at eucentric focus exhibits a slope of  $(3.29 \pm 0.05)$  °/100 $\mu\text{m}$ , such that cyclotron motion should be seen at 6.58 °/100 $\mu\text{m}$ . Concerning the possible use as a magnetic field probe, it would deliver data with 1.5 % accuracy, if the stage error for higher z-shift values could be compensated, the magnetic field determination with this method would deliver field data with 0.5 % accuracy, due to the reading error alone.

### 4.1.3 Measurements of the Vortex Rotation

Now, the holographic vortex mask is moved into the electron beam at the C2 aperture plane, creating EVB in the front-focal plane of the OL. These EVB are cut in half by a Si-KE placed in the specimen holder. The Si-KE is lifted from roughly -375  $\mu\text{m}$  to +375  $\mu\text{m}$ , just as it was described, in more detail, in the methods section. The complete set of images of such an experiment is shown in Figure 39 to Figure 41, in successive steps of 25  $\mu\text{m}$ , represented by each depicted row. This series shows five diffraction (vortex) orders, exhibiting topological charges with  $m = -3, -1, 0, +1, +3$ , aligned along the horizontal line. This imaginary horizontal line is, at the same time, approximately the azimuthal cutting angle of the Si-KE. Thus, looking at the first row(s) of Figure 39 gives the decisive impression that positive vortex orders did not or only slightly move, whereas the negative ones show a strong deviation of the horizontal cutting line as if their rotation went on faster than the one of the central  $m = 0$  beam.



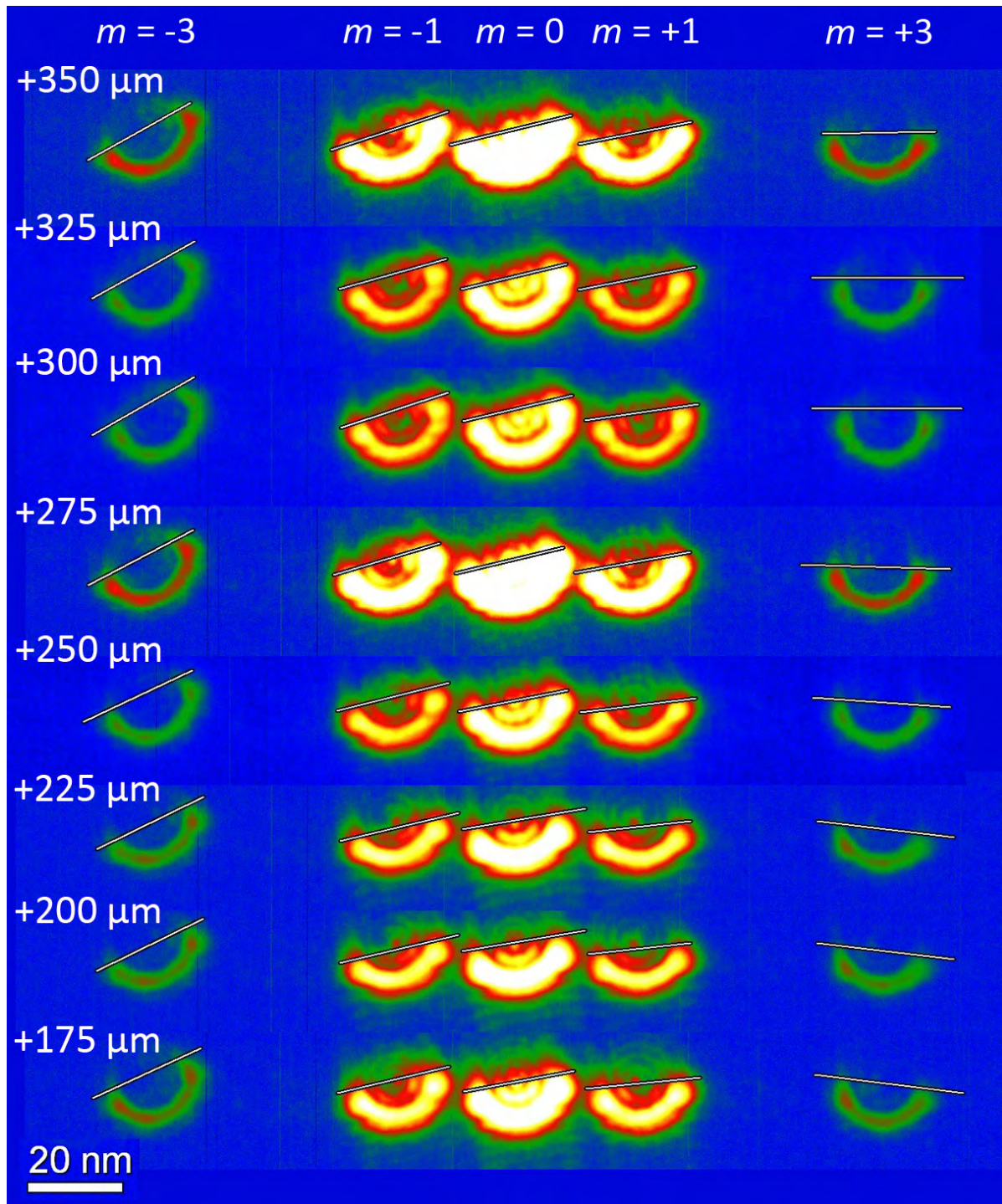


Figure 39: Images of EVB rotation, part one (+ 350  $\mu\text{m}$  to + 175  $\mu\text{m}$ ) of a full z-shift series. The whole series ranges from + 350  $\mu\text{m}$  to - 375  $\mu\text{m}$ . Topological charges  $m = 0, \pm 1, \pm 3$  are visible. The colour scale was used to enhance the image contrast. The observation plane was placed  $z_f = \sim 5 \mu\text{m}$  beneath the focused row of vortices (C2 over-focus). Note that the indicated z-values are the distances to the observation plane, not to the focus; this is the same for all following figures. The annotation lines indicate the measured azimuthal angle  $\varphi$ . Some vortex orders in part two, at low z-shift values, are not annotated, because they showed no cutting edge or were oversaturated.



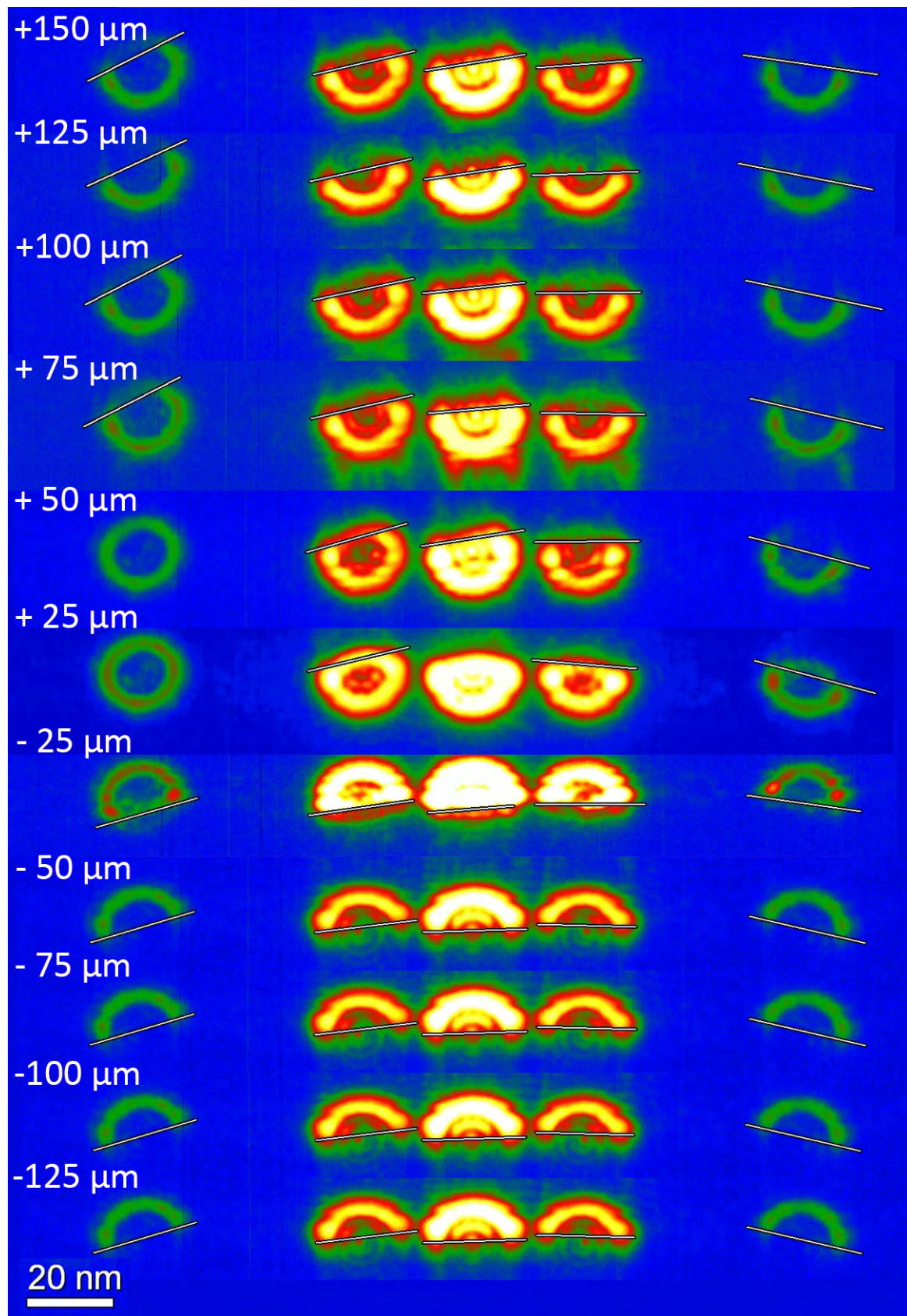


Figure 40: Part two of the same z-shift series ranging from + 150  $\mu\text{m}$  to - 125  $\mu\text{m}$ , with a 180° flip over between  $\pm 25 \mu\text{m}$ .



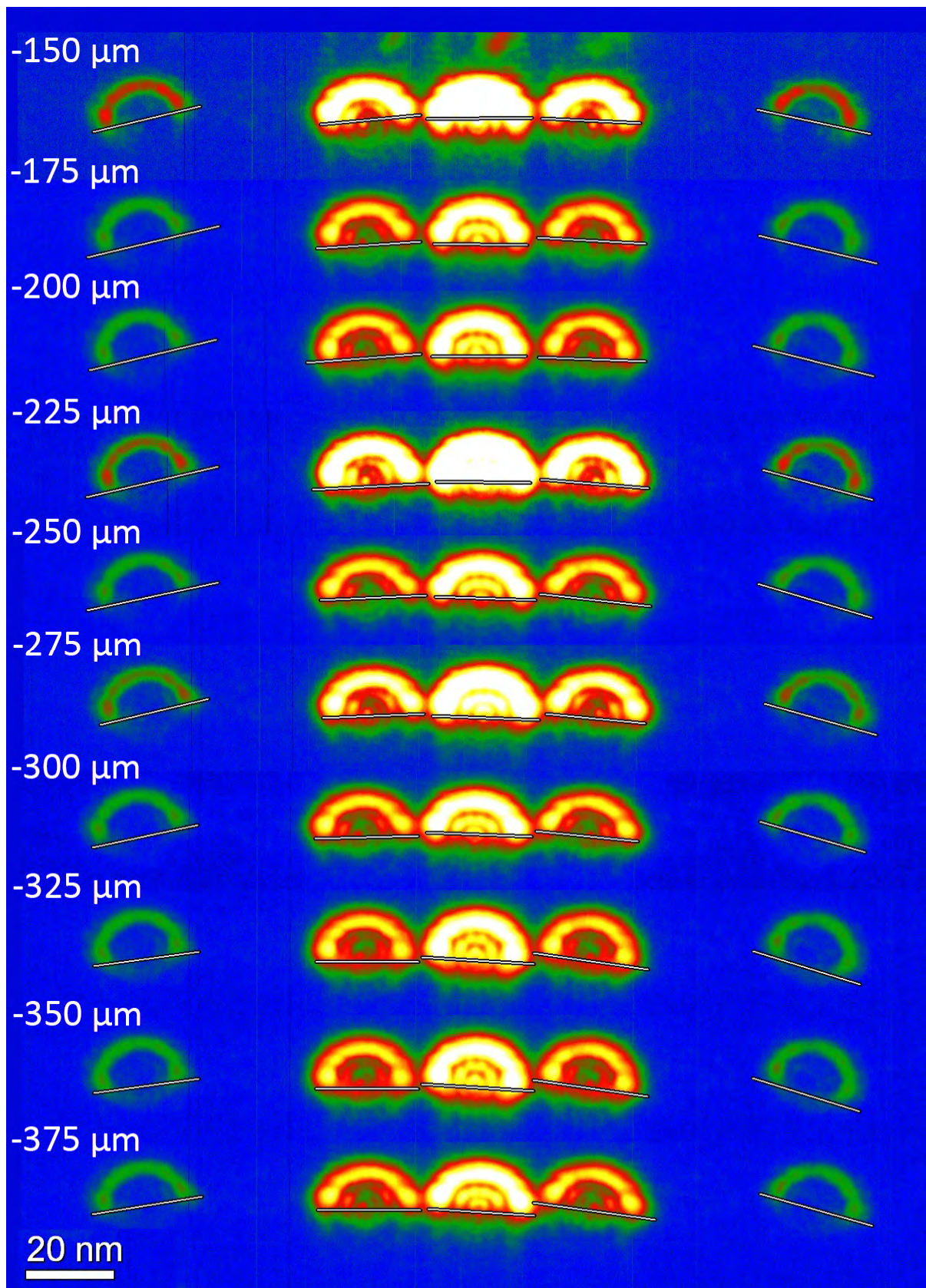


Figure 41: Part three of the same z-shift series ranging from - 150  $\mu\text{m}$  to - 375  $\mu\text{m}$ .

In fact taking into account the following rows quickly proves this simple picture wrong. The descending KE reveals rotational dynamics for all vortex orders. Moreover, the Cu-grid- as well as the Si-KE rotation results suggest that the magnetic field heads up; putting this together with the theoretical prediction in section 2.1.5, stating cyclotron rotation for  $\sigma \cdot m > 0$  and zero rotation for EVB obeying  $\sigma \cdot m < 0$ , with  $\sigma$  being the direction of the magnetic field, would lead to a contradiction. Qualitatively one can state that, the azimuthal angles of all vortex orders decrease with the same seemingly constant slope and thus, behave quite like the Cu-grid and the Si-KE shifted through the magnetic OL field.

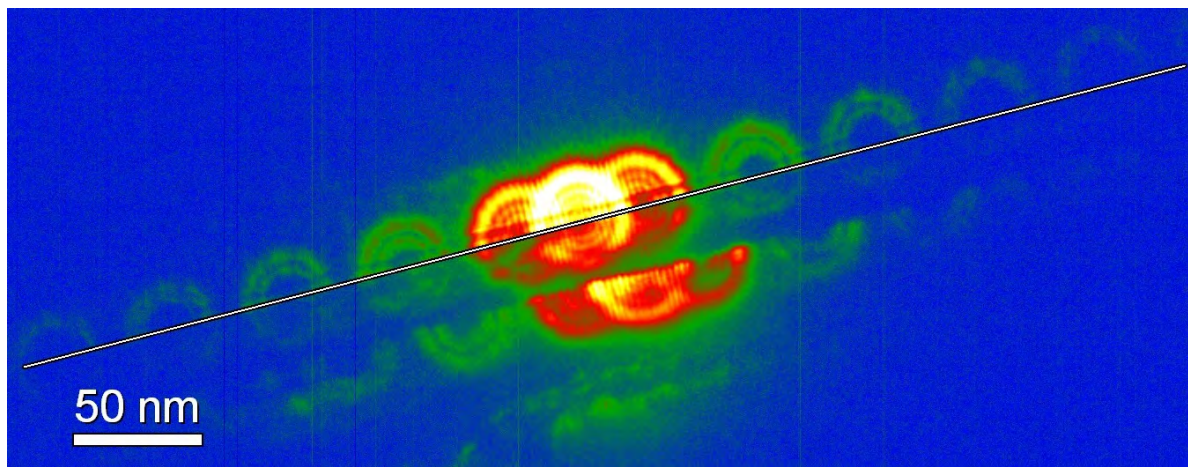


Figure 42: The experimental image at a z-shift height of  $0 \mu\text{m}$  and a C2 over-focus value  $z_f$  of  $11 \mu\text{m}$  clearly shows, that all vortices, up to topological charge  $m = \pm 9$ , are cut at the same azimuthal angle, that is zero, relative to the Si-KE. The line represents the Si-KE. The additional features, looking like a mirror image of the cut EVB, in the lower area of the image, are possible due to the semi-transparency of the Si-KE at the first few nanometers and show a second EVB cutting approximately  $20 \mu\text{m}$  below the actual observation plane.

Before more detailed quantitative results to the above shown experiment are given, two things should be noted before. First the Si-KE was inserted coming from the bottom of the images, but as the observation plane lied beyond the focus, an azimuthal rotation angle shift by  $180^\circ$  occurred for z-shift values greater than  $+5 \mu\text{m}$ , see Figure 40. This shifting angle is kind of automatically subtracted, when taking the angles of the annotation lines as they are given by DM3. With that the  $180^\circ$  shift will not show up in the following diagrams. Additionally, this strongly improves the visibility of the curves' slopes.

And the second thing is, that except the region in very close vicinity of the focal point, which was already investigated and described by others (Guzzinati, Schattschneider et al. 2013), one point was missing in the above z-shift series, namely the image of the observation plane at  $z = 0 \mu\text{m}$ . The reason



for that is the experimental difficulty to cut nanometre objects with a KE that is partly electron transparent at the first few nanometres. This is true especially for smaller observation plane defocus values, because of the associated smaller size of EVB. Nevertheless, Figure 42 shows an image of this point, from a different experiment with high defocus values, proving the assumption that in the observation plane, all vortex orders must be cut equal at the KE angle.

Now, coming to the quantitative results of Figure 39 to Figure 41, given in Figure 43, affirms the impression that all EVB orders rotate with a comparable azimuthal velocity for a gross of the experimental accessible z-shift region.

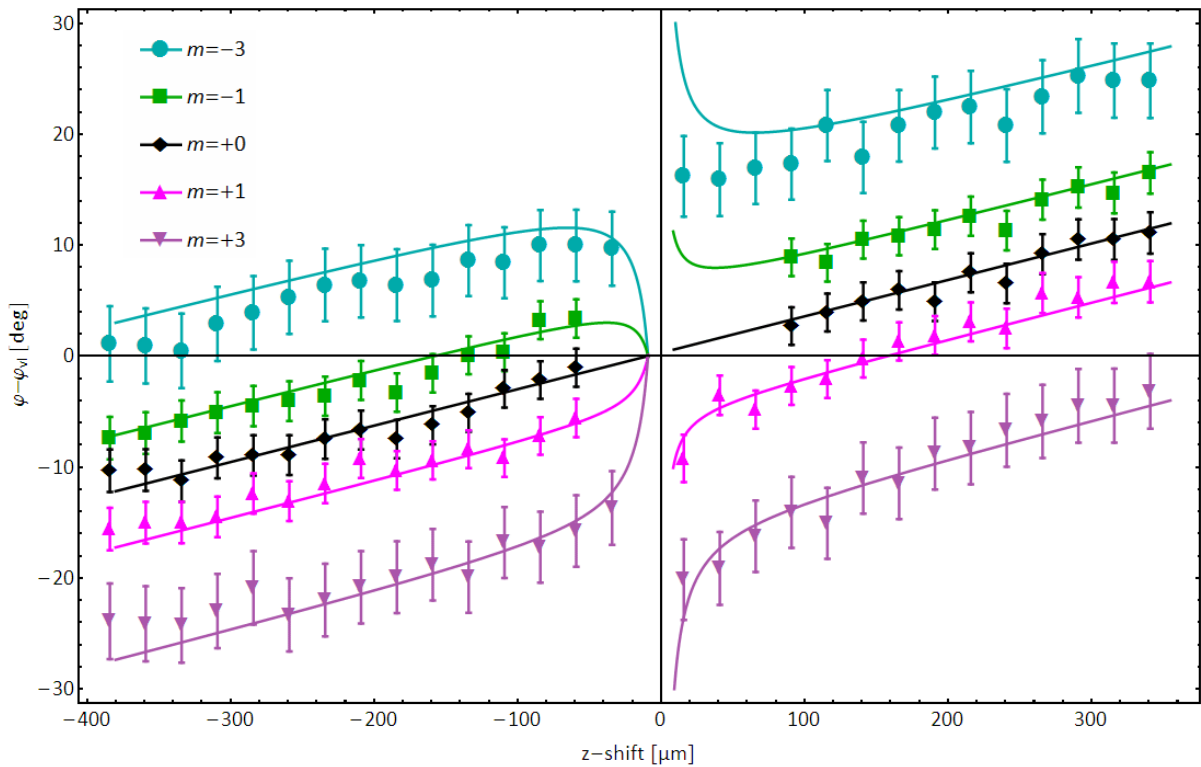


Figure 43: Diagram, showing the experimentally observed azimuthal rotation angles of EVB over the Si-KE z-shift position for the experiment shown in Figure 39 to Figure 41. Note that the origin was placed in the focal plane. The data hints at additional rotational dynamics beyond LR, in the vicinity of the focus at  $z = 0$ .  $z_f \sim -6 \mu\text{m}$ . The error bars are estimated upon the Si-KE roughness-, stage positioning-, reading- and intensity adoption errors. Even so in the following figures. The different diffraction orders carry topological charges  $m = 0, \pm 1, \pm 3$ . The solid lines represent the semi-classical model described in section 2.1.6, using the magnetic field strength  $B_z = 1.89 \text{ T}$ . The other parameters were  $z_f = -9 \mu\text{m}$  and  $\theta = 0.7 \text{ mrad}$ . The discrepancy between the  $z_f$  values is due to condenser-OL operation mode. The reduced convergence angle of the semi-classical model describes the centroid motion of the electrons.

The direction of this overall rotation is the same as the one observed in section 4.1.1 and 4.1.2.

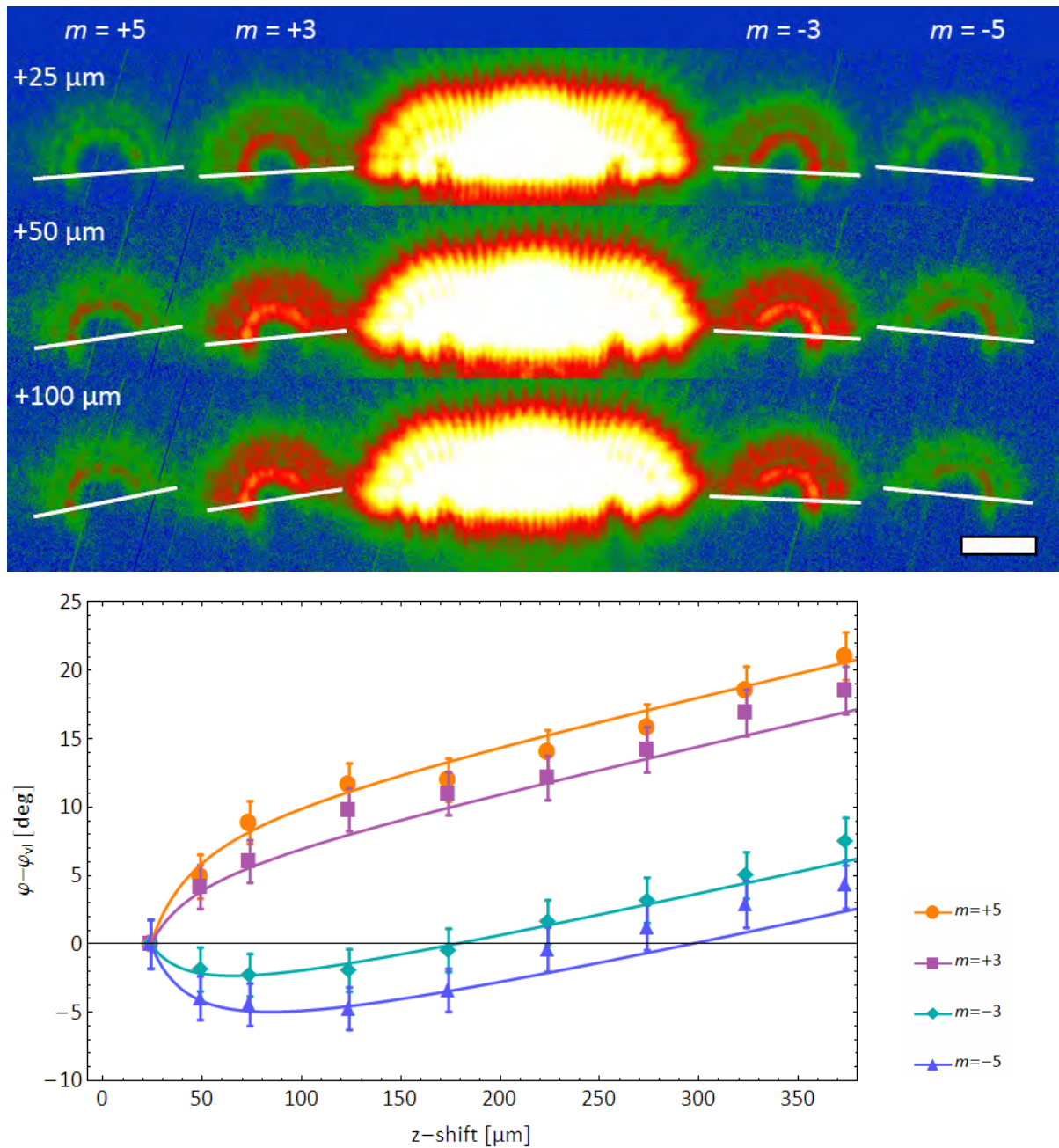


Figure 44: Upper row: Excerpt of a z-shift series showing the z-shift region where the peculiar rotations are expected to occur, with topological charges  $m = 0, \pm 1, \pm 3, \pm 5$  visible in the observation plane, which was  $z_f = \sim 10 \mu\text{m}$ , above the focused row of vortices. Note that the outer rings of the EVB orders were analysed, and that a difference between the angular evolution of positive and negative topological charge can be tracked down by eye. The z-shift values are given in the pictures. The scale bar is 20 nm. Lower row: Shows the data points for the above given experiment for positive z-values. Also indicating two distinct regions of rotational dynamics. The model was fitted using the same parameters as in Figure 43 except  $z_f = +24 \mu\text{m}$ .

The semi-classical model, equation (2.60), represented as solid thick lines in Figure 43 reproduces the data quite good, when adjusting the convergence angle to the centroid motion, according to the

Ehrenfest theorem. The best fit is acquired with  $\theta = 0.7$  mrad, this value leads to a ratio between the measured- and fitted semi-classical  $\theta$  of 0.6.

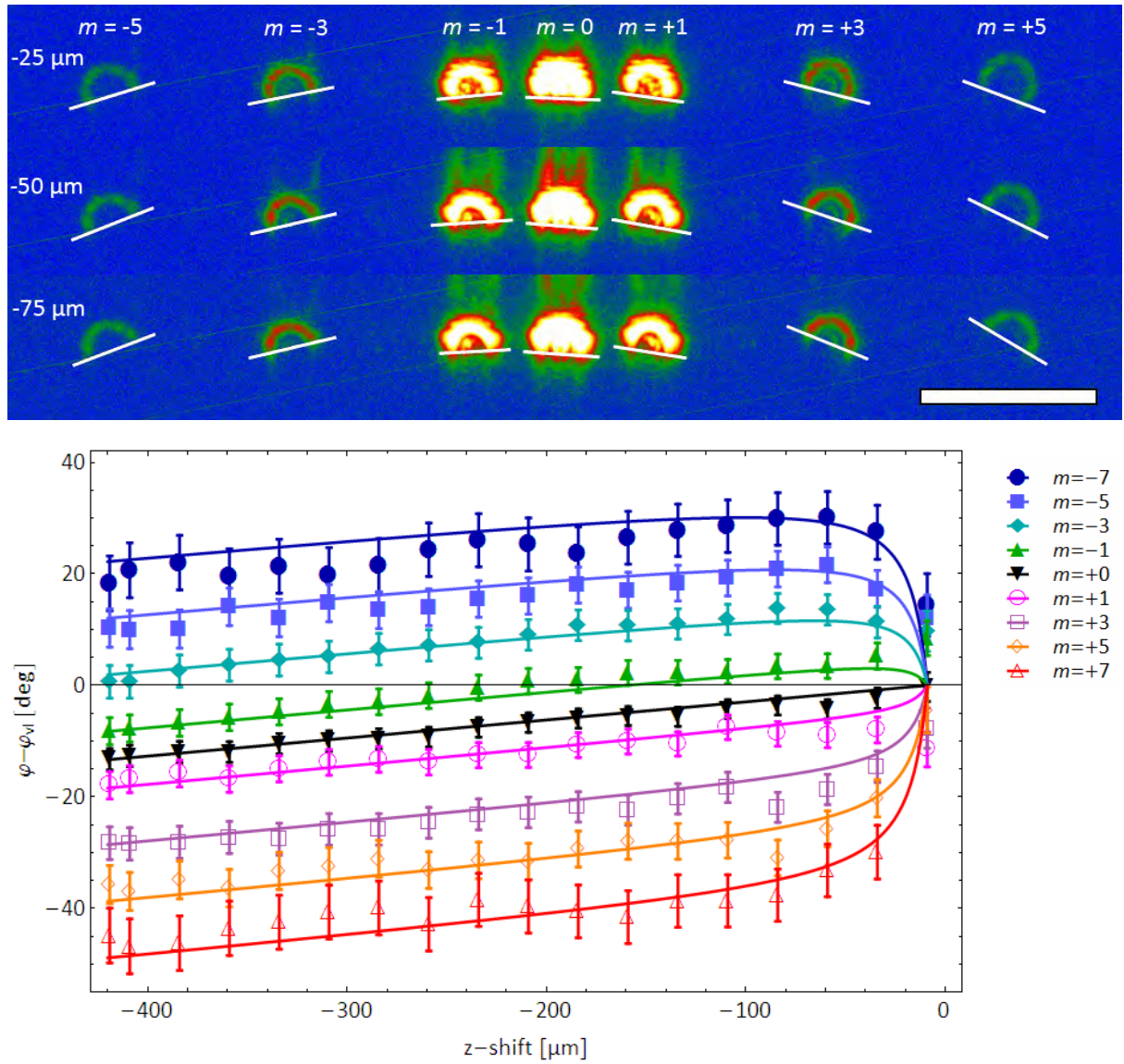


Figure 45: Upper row: Z-shift series of a vortex rotation experiment, with topological charges  $m = 0, \pm 1, \pm 3, \pm 5$  visible in the observation plane,  $z_f \sim 4.5 \mu\text{m}$ . EVB rotational dynamics can be discriminated by eye, for  $m = \pm 3$  and  $\pm 5$ , exhibiting the predicted LS behaviour. The scale bar is 50 nm. The lower row: Gives the full set of data points for the upper images. The model parameters where  $z_f = -9 \mu\text{m}$  and a reduced OL-excitation  $B_z = 1.87 \text{ T}$ , because the OL was strongly under-focused. LR is clearly resolvable for z-values beyond  $-100 \mu\text{m}$ , above that the slopes seem to decrease for negative orders and increase for positive ones, except for  $m = \pm 1$ .

This value is higher than the theoretical one, being 0.42, indicating that the centroid of the electron distribution is shifted outwards. The difference between the given  $z_f$  value, to the one used in the semi-classical model is due to the condenser-OL operation mode.

Table 4 gives the measured magnitude of rotational speed or slopes  $\bar{s}$  plus the estimated absolute and relative standard error for the z-shift region above +130  $\mu\text{m}$  and beyond -130  $\mu\text{m}$  showing that the expected LR of 3.3  $^\circ/100\mu\text{m}$  is quite well reproduced within the error margin, not only for the  $m=0$  order, but for all vortex orders. The error estimation included, Si-KE roughness, stage positioning, as well as reading- and intensity adoption errors. A Si-KE roughness value of  $R_z = 0.4 \text{ nm}$  was used. The relative stage positioning error was set to 3 %. The reading error for the colour scale contrast analysis method, which was used for the experiment given in Figure 43, amounted to  $\pm 0.5^\circ$  for lower vortex orders and  $\pm 1^\circ$  for  $m = \pm 3$ . The estimated intensity adoption error was  $2^\circ$  for  $m = \pm 3$  and  $1^\circ$  for the other vortex orders. The aforementioned statements, except the amounts of reading- and intensity adaption errors, are equally true for different experimental conditions, like higher and opposite C2 defocus values  $z_f$ , as for example, in the experiment given in Figure 44 and Table 5 and different OL-excitation in the experiment given in Figure 45 and Table 6.

$m$	Estimated slope $\bar{s}$ [ $^\circ/100\mu\text{m}$ ]	Standard error $\pm\Delta s$ [ $^\circ/100\mu\text{m}$ ]	Relative Standard error $\pm\Delta s$ [%]
-3	3.56	0.29	8.1
-1	3.37	0.16	4.7
0	3.2	0.16	4.9
1	3.18	0.16	5
3	2.93	0.29	9.8

Table 4: Lists the estimated slopes with absolute and relative standard errors for the experiment shown in Figure 39 to Figure 41 and Figure 43 and z-shift regions above +130  $\mu\text{m}$  and beyond -130  $\mu\text{m}$ .

Also, note that for the electron mass  $m_e$  in the semi-classical model, the relativistic expression including the gamma factor was used, the other parameters for that model can be found in the caption of Figure 43, Figure 44 and Figure 45. A systematic offset between positive and negative z-values, which is due to the angle determination procedure and the flip over by  $180^\circ$  at the focus has been corrected; it was of the order of  $2^\circ$ .

$m$	Estimated slope $\bar{s}$ [ $^\circ/100\mu\text{m}$ ]	Standard error $\pm\Delta s$ [ $^\circ/100\mu\text{m}$ ]	Relative Standard error $\pm\Delta s$ [%]
-5	2.74	0.54	19.6
-3	2.94	0.43	14.5
3	3.65	0.43	11.7
5	3.89	0.54	13.8

Table 5: Lists the estimated slopes with absolute and relative standard errors for the experiment shown in Figure 44 and z-shift regions  $|z| > 130 \mu\text{m}$ .

The reading error for the experiment given in Figure 44 amounted to  $\pm 1.5^\circ$  for vortex orders  $m = \pm 5$  and  $\pm 1^\circ$  for EVB carrying the topological charge  $m = \pm 3$ . Whereas the estimated intensity adaption

error was  $3^\circ$  for  $m = \pm 5$  and  $2.5^\circ$  for  $m = \pm 3$  EVB orders. Coming to the experiment given in Figure 45, the reading error for the experiment amounted to  $\pm 1.5^\circ$  for vortex orders  $m = \pm 7$  and  $\pm 1^\circ$  for  $m = \pm 5$  and  $0.5^\circ$  for the rest EVB orders. And the estimated intensity adaption error was  $3^\circ$  for  $m = \pm 7$  and  $2^\circ$  for  $m = \pm 5, \pm 3$ ,  $1^\circ$  for  $m = \pm 1$  and  $0.5^\circ$  for  $m = 0$ .

$m$	Estimated slope $\bar{s}$ [ $^\circ/100\mu\text{m}$ ]	Standard error $\pm\Delta s$ [ $^\circ/100\mu\text{m}$ ]	Relative Standard error $\pm\Delta s$ [%]
-5	2.85	1.13	39.8
-3	3.95	0.96	24.3
-1	4.03	0.79	19.6
0	2.99	0.62	20.7
1	2.71	0.79	29.1
3	2.76	0.96	34.9
5	2.93	1.13	38.7

Table 6: Lists the estimated slopes with absolute and relative standard errors for the experiment shown in Figure 45 and z-shift regions  $|z| > 130 \mu\text{m}$ .

In these experiments, so far, only weak trends indicate a deviation of the LR for z-shift values  $|z| < 100 \mu\text{m}$ . Besides, more complex rotational dynamics could hardly be verified in this region, partly due to a lack of data points.

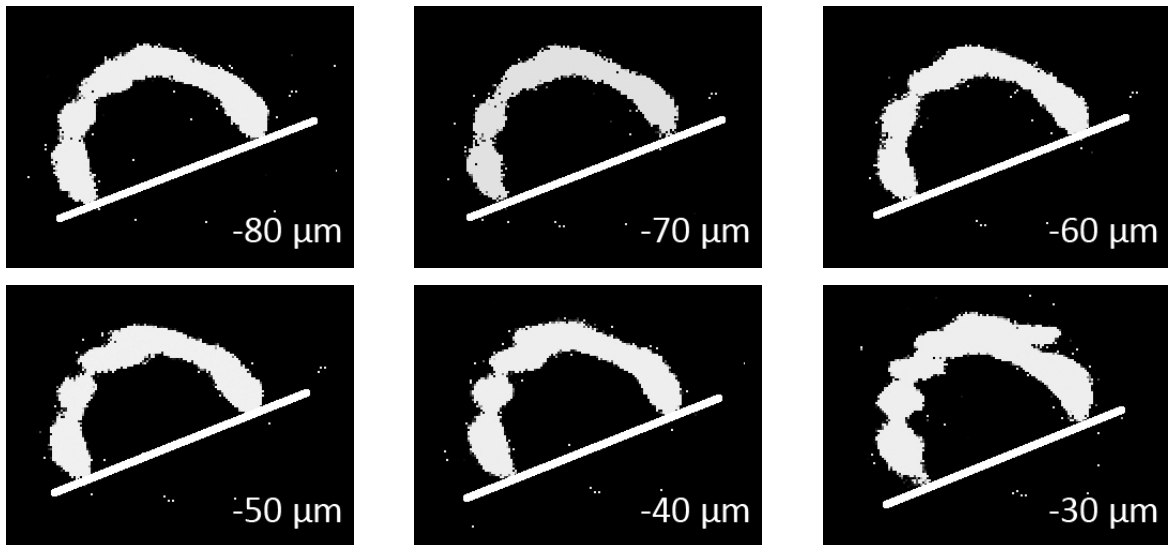


Figure 46: Images of a single vortex order, with topological charge  $m = -3$ , visualizing the still standing EVB LS for  $\sigma \cdot m < 0$ . Strong gamma expansion was used for contrast enhancement. The intensity level was adopted in each picture such that the thickness and structural features are approximately the same.

To the time, when the experiments in Figure 43, Figure 44 and Figure 45 were done, the author was not aware of the relations between rotational- and irrotational vortices described in the semi-



classical derivation section 2.1.6. As a result the experimental focus was laid on acquiring data points at as high as possible z-shift values. This is in contrast to the desired situation, where it is crucial to collect data points at and around the z-shift values corresponding to the magnetic beam waist  $w_m$ .

With this progression in understanding the ongoing process, two additional experiments were undertaken to probe the predicted LS more thoroughly, at the same time the gamma expansion analysis method was applied. The pictorial result of one of these two experiments is shown in Figure 46 and Figure 47. Figure 46 depicts a z-shift series ranging from  $-80$  to  $-30 \mu\text{m}$  of the  $m = -3$  EVB exhibiting no observable azimuthal angle deviation, whereas the single  $m = +3$  EVB in Figure 47 clearly shows rotational dynamics.

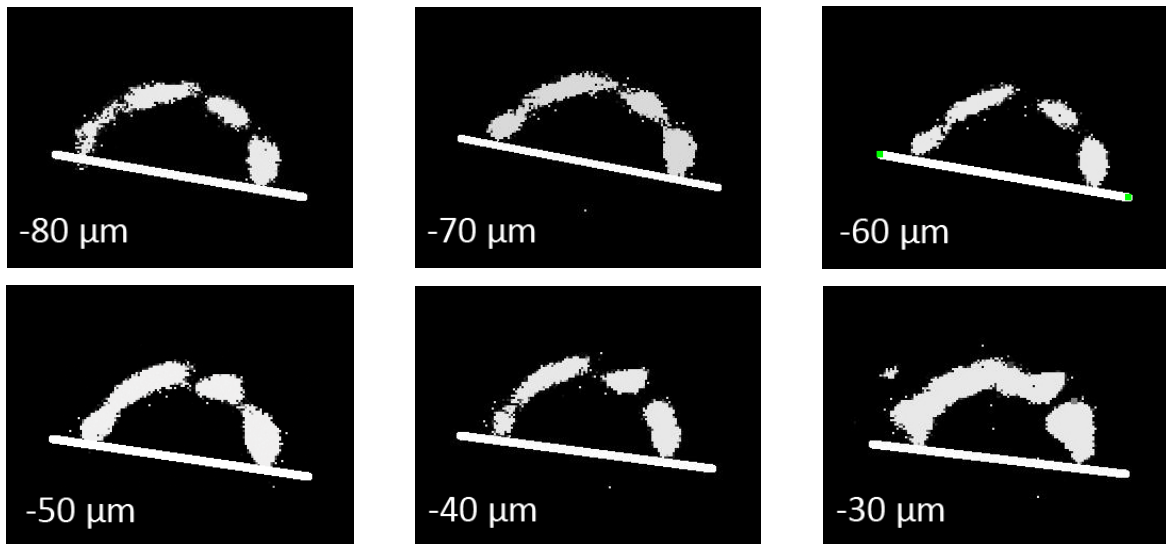


Figure 47: Images of the  $m = +3$  vortex order of the same experiment as in Figure 46. Exhibiting a rotation of  $\sim 3^\circ$  over  $50 \mu\text{m}$  z-shift, thus being twice as fast as would be expected from standard image rotation and by that imaging EVB LS for  $\sigma \cdot m > 0$ . The same gamma expansion and intensity adoption procedure as in Figure 46 was used.

When plotting these azimuthal rotation angles over the z-shift value, see Figure 48, left, it turns out that the EVB rotate with approximately twice the LR angular velocity, respectively, approximately zero angular velocity, showing good agreement with the solid theory lines  $(0, \omega_l, 2\omega_l)$ . And with that, these two series represent a direct observation of EVB LS in vacuum for  $\sigma \cdot m < 0$  and  $\sigma \cdot m > 0$ . This statement can be backed by looking at the data given in Table 7, where the estimated slopes for the experimental data of Figure 48, left and right, are given together with their absolute and relative standard errors. There, the indicated slopes for  $m = \pm 3$  and  $m = \pm 2$  vortex orders can be clearly distinguished from each other, within the estimated error, as well as their absolute values reproduce



## 4 Results

the predicted slopes from Bliokh and co-workers, being 0, 3.29, and 6.58 °/100 $\mu\text{m}$ , respectively.

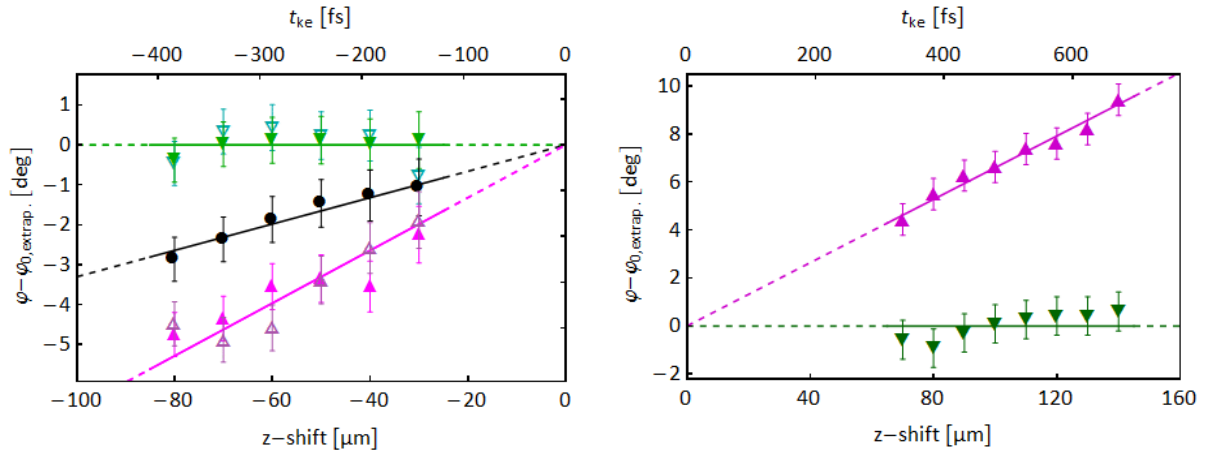


Figure 48: Left: Diagram, showing the measured azimuthal rotation angles of Figure 46 and Figure 47 subtracted by  $\varphi_{0,extrapol.}$  plus EVB orders  $m = \pm 1$  in a z-shift region, where the convergent EVB radii get of the order of the magnetic beam waist  $w_m \sim 40$  nm. Note, that the origin was chosen to be the observation plane, as depicted in Figure 22. The straight lines represent the expected azimuthal angles increase for 0, LR and 2LR, respectively. The colour coding is the same as in the preceding figures. The estimated error could be reduced to  $\pm 0.6^\circ$ , due to the gamma expansion and intensity adoption method. Right: The same as left, but for an experiment using a holographic vortex mask with 7.5  $\mu\text{m}$  in diameter and a convergence angle 0.41 mrad to “elongate” the Landau state region. The EVB orders depicted are  $m = \pm 2$ .

The  $m = \pm 1$  order can not be distinguished that clear. This could be due to the fact that the chosen z-shift region from -80 to -30  $\mu\text{m}$  is already far off the z-shift values where the irrotational- and rotational vortex phenomena are of equal “strength”.

$m$	Estimated slope $\bar{s}$ [°/100 $\mu\text{m}$ ]	Standard error $\pm \Delta s$ [°/100 $\mu\text{m}$ ]	Relative Standard error $\pm \Delta s$ [%]
-3	-0.35	1.92	n.a.
-2	0.07	1.36	n.a.
-1	0.76	1.92	n.a.
0	3.70	1.68	51.9
1	4.27	1.92	44.9
2	6.59	1.16	17.6
3	5.88	1.92	32.6

Table 7: Lists the estimated slopes with absolute and relative standard errors for the two experiments shown in Figure 48 in a z-shift region roughly around the magnetic beam waist.

For  $m = \pm 3$  vortices, this region occurs at a radius of 46 nm, which corresponds to a z-shift of 39  $\mu\text{m}$ , which lies well within the data sample from Figure 48, left. On the other hand  $m = \pm 1$  vortices reach that condition closer to the focal point at  $z = 23$   $\mu\text{m}$ , at a radius of 26 nm, which lies not even in the given z-shift region in Figure 48, left. For the  $m = \pm 2$  EVB in Figure 48, right, the radius should be

37 nm to meet that point of equal “strength”, lying at  $z = 91 \mu\text{m}$ , which is also well within the given  $z$ -shift range. If the linear model fit routine is fed with the experimental data, including also a value from  $z = -25 \mu\text{m}$ , which is not shown in Figure 48, left, the acquired slopes are  $\bar{s} = (4.63 \pm 1.63)^\circ / 100 \mu\text{m}$  for  $m = 1$  and  $\bar{s} = (0.21 \pm 1.63)^\circ / 100 \mu\text{m}$  for  $m = -1$ . Thus justifying the above statement also for the  $m = \pm 1$  vortex order.

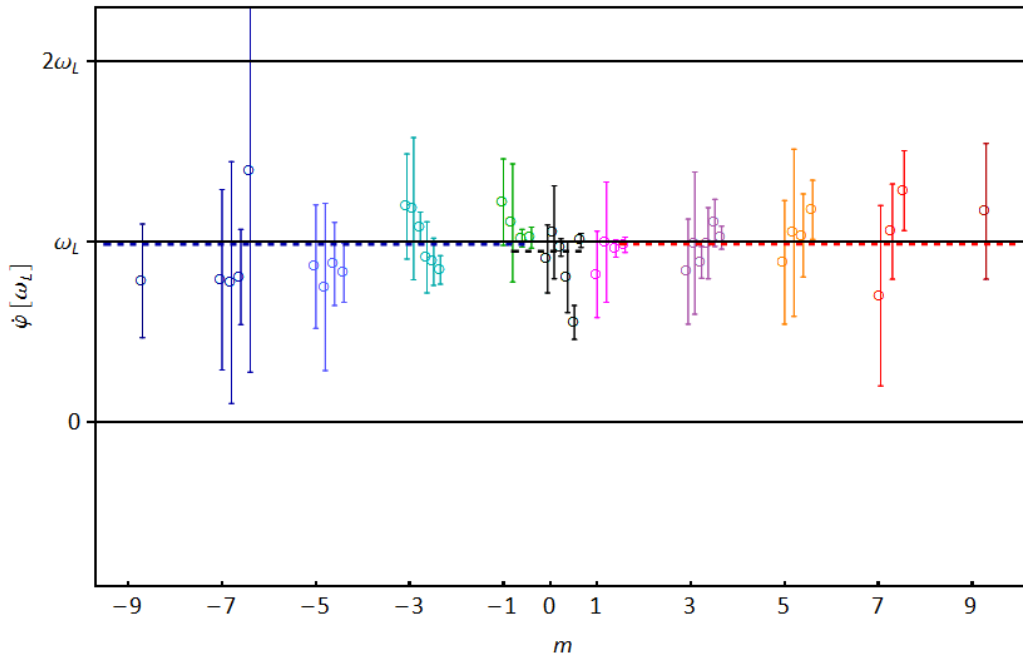


Figure 49: Shows a scatter plot, depicting the measured slopes and their estimated error for different vortex orders  $m$  acquired in seven experiments for  $z$ -shift values “far” off ( $>100 \mu\text{m}$ ) the focal region. The dashed lines represent their mean values, showing no definite trend to different rotational speeds. Thus, proving that LR overrules the irrotational vortex effect of the EVB, away from the magnetic beam waist. The colour coding is the same as in the preceding figures.

In a last step, slopes for all measured azimuthal rotation angles stemming from eight, respectively, seven experiments, were estimated using a linear fit routine weighted by the estimated errors for the two  $z$ -shift regions  $|z| \leq 100 \mu\text{m}$  and  $|z| > 100 \mu\text{m}$ , see Figure 49 and Figure 50. – Note that other experiments where e.g. an aperture was used as a KE were excluded due to fact that the introduced surface roughness errors would completely overrule the faint EVB azimuthal rotations.

These scatter plots show a robust trend for EVB azimuthal motion within the magnetic field of the OL. That is the strong dominance of only one rotational speed for  $|z| > 100 \mu\text{m}$  being independent of the vortex order, see Figure 49. The dark blue dashed line represent the weighted mean value for all measured vortex orders with  $m < 0$ , the black dashed line represent the weighted mean value for all measured vortex orders with  $m = 0$ , whereas the red dashed line stands for the weighted mean value

for all measured vortex orders with  $m > 0$ . Their mean slope values  $\bar{s}_{m<0} = (3.26 \pm 0.09)^\circ / 100\mu\text{m}$ ,  $\bar{s}_{m=0} = (3.13 \pm 0.09)^\circ / 100\mu\text{m}$  and  $\bar{s}_{m>0} = (3.26 \pm 0.08)^\circ / 100\mu\text{m}$  indicate no definite deviation from each other, as well as their absolute value fit reasonable well to the acquired slope for standard image LR, of e.g. the Si-KE under parallel illumination.

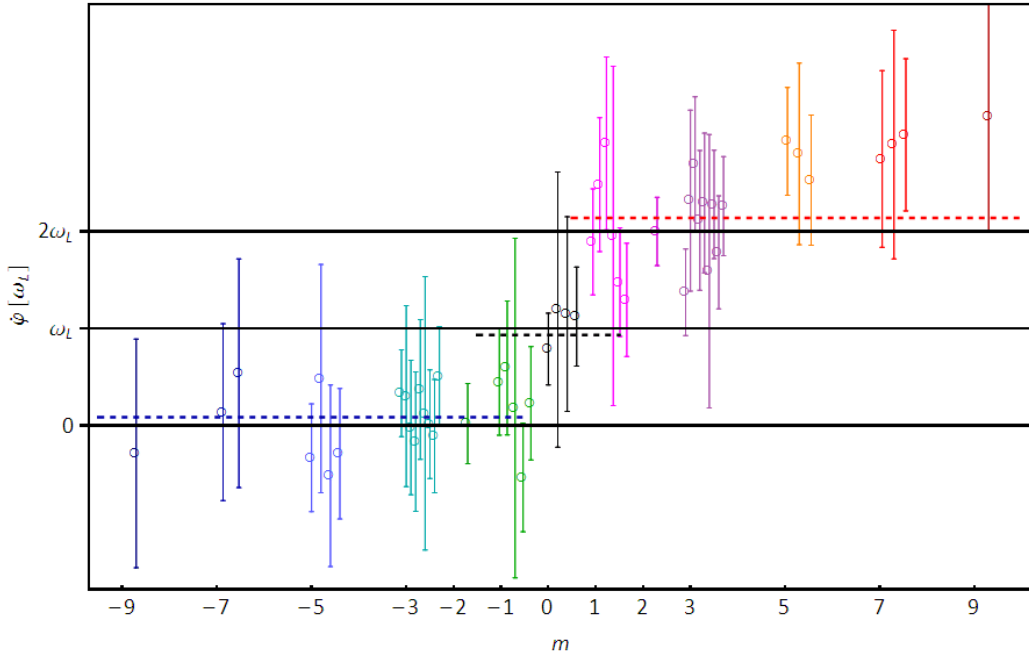


Figure 50: Same as Figure 49, but for  $z$ -shift values in close vicinity to the focus ( $|z| < 100\mu\text{m}$ ), clearly expressing vortex order depended slopes.

On the contrary, Figure 50 depicts a definite trend to vortex order dependent rotational dynamics in the  $z$ -shift regime in close proximity to the focal point but above the much faster Gouy-phase region ( $z_R < |z| < 100\mu\text{m}$ ). So to say, negative vortex orders show clearly diminished rotational dynamics compared to positive ones. The dashed lines in Figure 50 represent the mean values for positive-, negative- and  $m = 0$  vortex orders given by  $\bar{s}_{m<0} = (0.29 \pm 0.46)^\circ / 100\mu\text{m}$ ,  $\bar{s}_{m=0} = (3.08 \pm 0.93)^\circ / 100\mu\text{m}$  and  $\bar{s}_{m>0} = (7.05 \pm 0.45)^\circ / 100\mu\text{m}$ , respectively. And with that, proving the EVB azimuthal rotational behaviour being vortex order dependent according to the presented theory by Bliokh and his co-workers, as well as the described by the semi-classical model.

#### 4.1.4 Numerical Results

In this section, results of three different approaches simulating the EVB  $z$ -shift experiment will be given. This was done to better understand the results and provide a reference test for the methods to determine the azimuthal angles.

On the one hand, two wave-mechanical approaches will be presented, see Figure 51, Figure 52, Figure 53 and Figure 54, (Floss 2013).

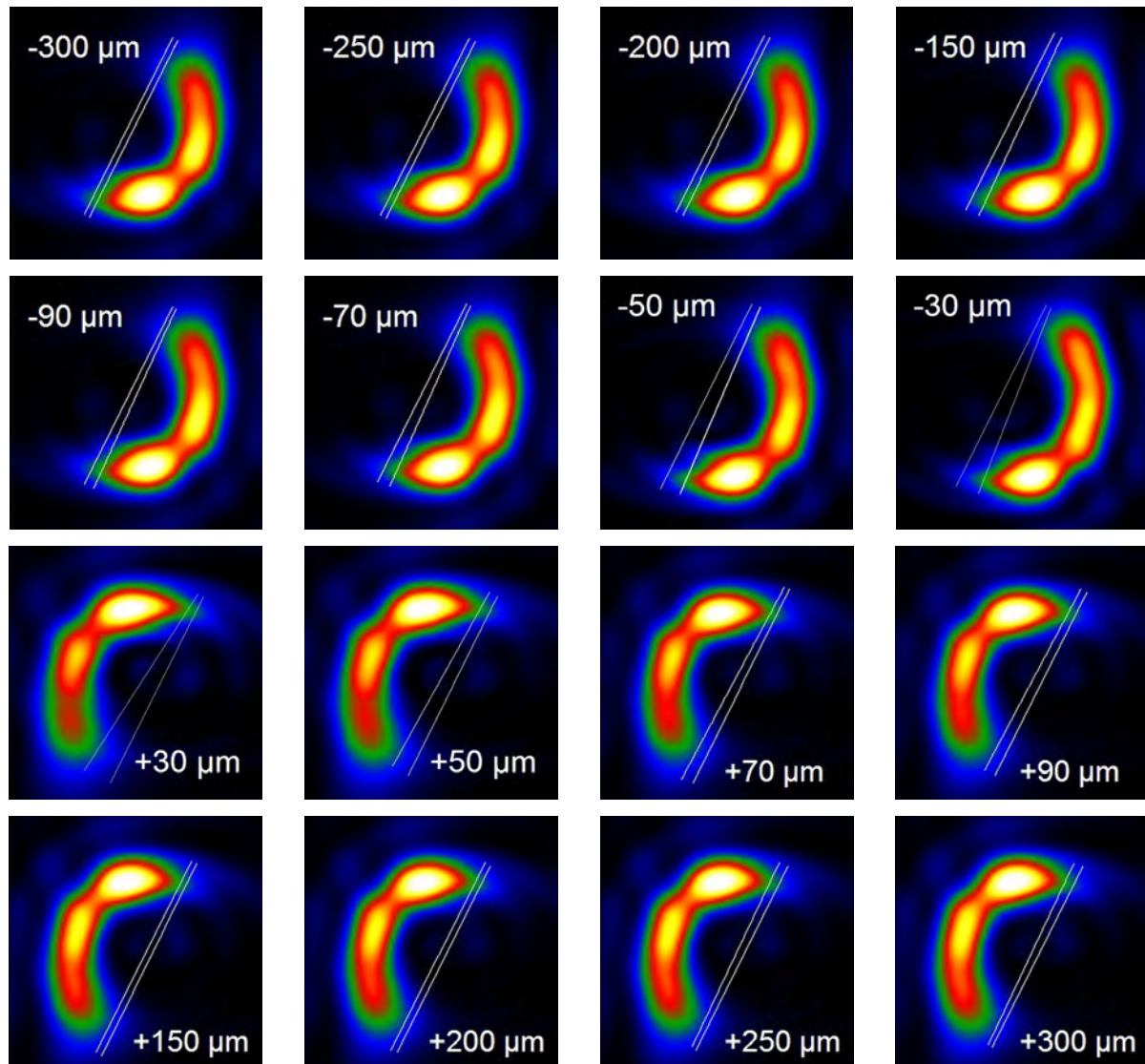


Figure 51: Excerpt of a  $z$ -shift series ranging from  $-300 \mu\text{m}$  to  $+300 \mu\text{m}$ , using a wave mechanical simulation of the vortex rotation experiment with  $z_f = 5 \mu\text{m}$ ,  $\theta = 1.16 \text{ mrad}$  and  $m = +3$ . The outer line represents a reference line with an angle of  $63.6^\circ$  as a guide to the eye, whereas the line closer to the simulated cut-vortex intensity distribution represents the measured angle, which will be given in the following. Rotational behaviour is only present at low  $z$ -values. The simulation did not include magnetic fields. The inner structure of the simulated cut-vortices given resembles the measured ones except the additional peaks shown in Figure 31.

And on the other hand, the results of a ray tracing code employing the LF and a bell shaped Glaser field mimicking the OL field will be shown, see Figure 55, Figure 56. – Figure 51 depicts an excerpt of a wave-mechanical simulation ranging from  $-300 \mu\text{m}$  to  $+300 \mu\text{m}$ . These images were calculated

using the free space propagator for scalar waves after passing a focusing lens. Magnetic fields were not included in the simulation code. This fact manifests itself by the missing rotation for  $z$ -values above  $|z| = 150 \mu\text{m}$ , see Figure 51. Below that region the Gouy-phase rotations get clearly visible, resembling the  $\arctan(z/z_R)$  behaviour quite well. Though, not the arctan was used to plot the theory line in Figure 52, but the semi-classical model with  $B_2 = 0$ , which is identical to the arctan for  $z$ -values off the Rayleigh range. The simulated half-moon like intensity maps in Figure 51 reveal a nontrivial inner structure, stemming from diffraction effects on the sharp KE. With that, the experimentally observed complex inner cut-vortex order structure can be, at least partly, assigned to these diffraction effects at the KE.

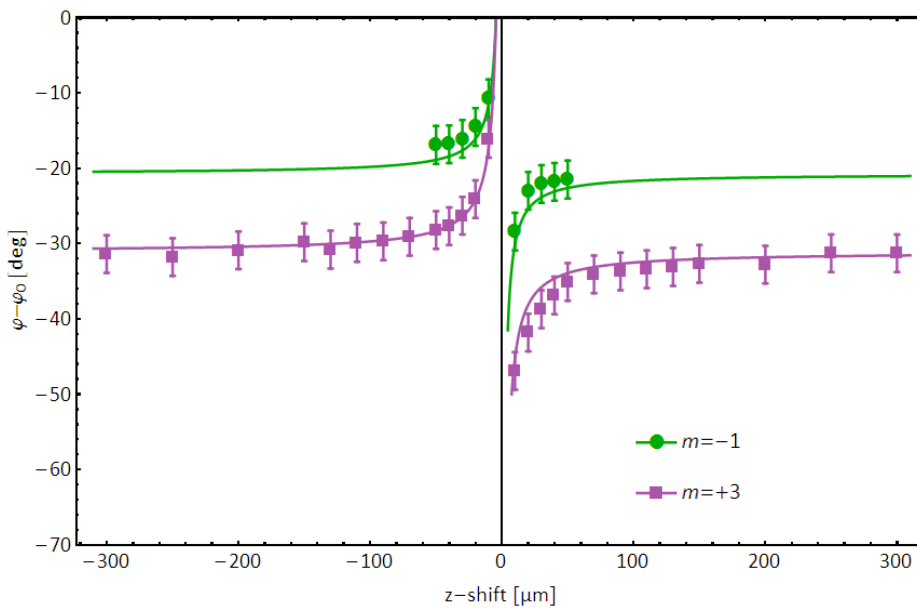


Figure 52: Shows the measured azimuthal angles of the simulated data in Figure 51 using the colour scale contrast method. The solid line represents the Gouy-phase, as well as the irrotational vortex behaviour included in the semi-classical model. The parameters of the semi-classical model were  $z_f = -4.5 \mu\text{m}$  and  $\theta = 0.7 \text{ mrad}$ . The offset angle for negative and positive  $z$ -shift values due to the  $180^\circ$  flip was  $\varphi_{0,-zs} = -95^\circ$  and  $\varphi_{0,+zs} = -96^\circ$ , respectively.

The estimated measurement reading- plus intensity adoption error in Figure 52 is  $\pm 2.5^\circ$  and thus roughly twice that of the one used for the TEM EVB rotation experiments, this is due to the fact that either the right or left arm of the half-moon like intensity distribution of a single vortex order exhibits no clearly defined edge onset, see Figure 51. Experimentally, mostly both arms of an EVB order show peaks at the edge onset, see for an example the three dimensional representation of such a measured intensity distribution in Figure 31. One assumption is that these features are due to KE geometry and –absorption effects, which were not included in the simulation. Nevertheless, the

observed rotational dynamics are well known for optical and electron beams (Hamazaki, Mineta et al. 2006, Guzzinati, Schattschneider et al. 2013, McMorran, Pierce et al. 2013). The result given in Figure 52, proves that the colour scale angle determination method used, is a viable tool to extract the rotational dynamics of the EVB z-shift experiments. Even the observed difference between the offset angle for positive and negative z-shift values of the order of 1-3 °, has also been observed in the analysis of the given simulation data. In addition, it is interesting to see that, without the overlaid LR of the magnetic field, the vortex order dependent asymmetry of rotational velocities (LS) does not occur, resembling the Gouy-phase, only.

Now, coming to the second wave-mechanical simulation results shown in Figure 53, which were kindly provided by Isabella Floss, a rich inner structure, due to diffractions effects, can also be seen. This time Kirchhoff's diffraction formula was solved for an incoming spherical electron wave. The cutting was done by setting the intensity of this incoming wave to zero in half of the azimuthal plane (from 0 to  $\pi$ ), at a certain z-value. This was repeated for different z-values ranging from +30 to +100  $\mu\text{m}$ , see Figure 53. The simulation parameters were  $\theta = 1.9$  mrad and the observation plane defocus  $z_f = -5$   $\mu\text{m}$ . The magnetic field was also not included in this simulation.

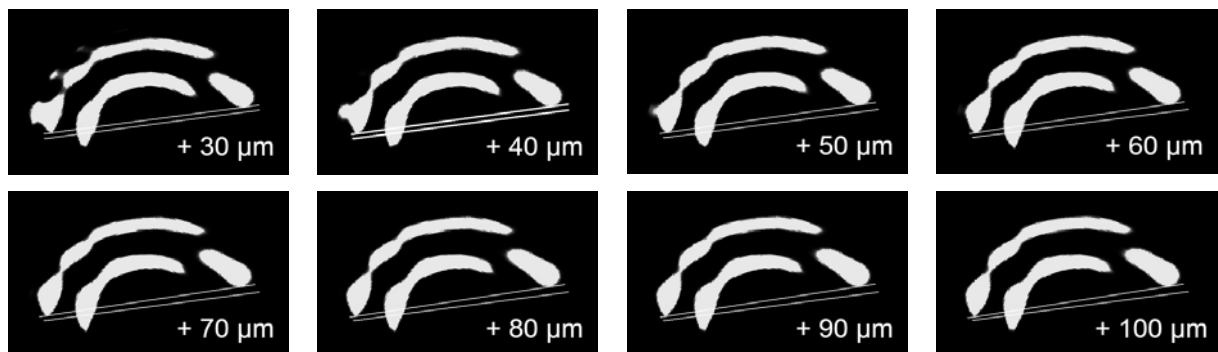


Figure 53: Gamma expanded z-shift series of a single cut vortex order  $m = +3$ , simulated by Isabella Floss, with measurement annotation lines added by the author. The intensity- or contrast limit was adjusted, such that the structure of each depicted vortex order is alike. In addition to the complex inner structure rotational dynamics are visible.

Concerning the inner structure of a single EVB order, these simulations show even better agreement with the experiment, e.g. the inner rings depicted in Figure 53, can also be observed in Figure 30, left and middle, Figure 32, inset, Figure 39 to Figure 41 for  $m = \pm 1, 0$ , Figure 42 and are especially strongly visible in Figure 44, upper row, where the outer vortex ring structure even drops in intensity below the inner ring. They also show the second peak at the edge onset, but it is still not clear whether they fully originate from diffraction effects of the KE, because its relative intensity compared to the edge onset peak on the other side, is much lower than the one observed experimentally. Nevertheless, the

occurring of both of these peaks renders the azimuthal angle determination easier and more accurate, independent of their origin. Figure 54, presents the measured azimuthal angles over the z-shift value determined by the strong gamma expansion and intensity adoption method. The accordance to the model is very good, indicating the applicability of the method to resolve faint azimuthal angle deviations occurring in the EVB z-shift experiments, provided the simulation data resembles the well known Gouy-phase behaviour.

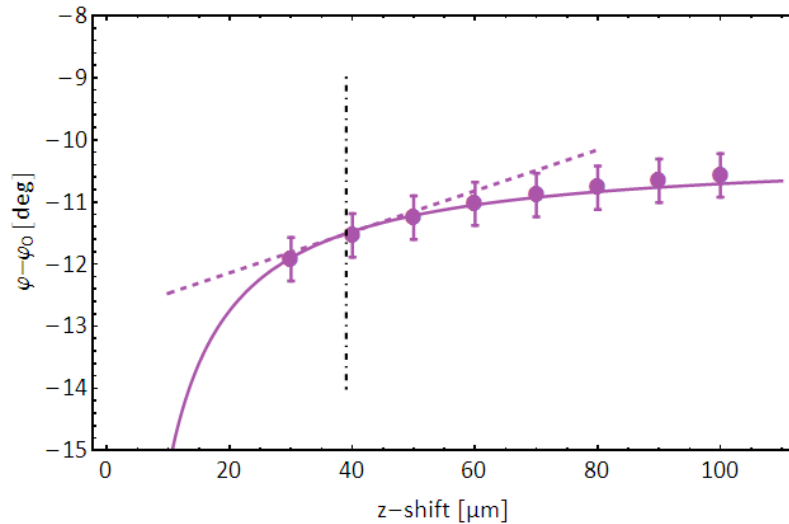


Figure 54: Shows the measured azimuthal angles of Figure 53 (purple solid dots) for a simulated convergence angle of 1.9 mrad. The dashed line represents the theory line with a slope of 3.3  $^{\circ}/100\mu\text{m}$ . The solid purple line represents the semi-classical model for a magnetic field of  $B_z = 1.89$  T, a semi-convergence angle of 1.16 mrad and  $z_f = -5$   $\mu\text{m}$ . Note that the semi-classical convergence angle is again lower than the wave-mechanical one, and that their ratio is 0.61 compared to 0.6, which was found for as a best fit in the experimental results section. The vertical black dot-dashed line indicates the z-shift value where the radius of the EVB approaches  $\rho = w_M \cdot \sqrt{|m|/2}$ . This is the position, where the EVB APC would add up to the vector potential induced one, as to give twice the LR. Also it is indicated the position where the slope of the semi-classical model without magnetic field amounts to 3.3  $^{\circ}/100\mu\text{m}$ . The error bars depict the pure reading- plus intensity adoption error of 0.35  $^{\circ}$ .

These two numerical simulations helped to better understand the angle determination procedure, as well as the inner structure observed. Moreover, the comparison of the simulated data with the semi-classical model delivers the same ratio between the convergence angles of the wave-mechanical simulation and the semi-classical model, which is of the order of 0.6. This further confirms the wave-mechanical approach, as well as it backs the best fit  $\theta$  value for the centroid motion in the semi-classical model. The deviation to the theoretical value of 0.42 could be due to diffractions effect.

As a next step the results of the ray tracing code employing the LF and a bell shaped Glaser field will

be given.

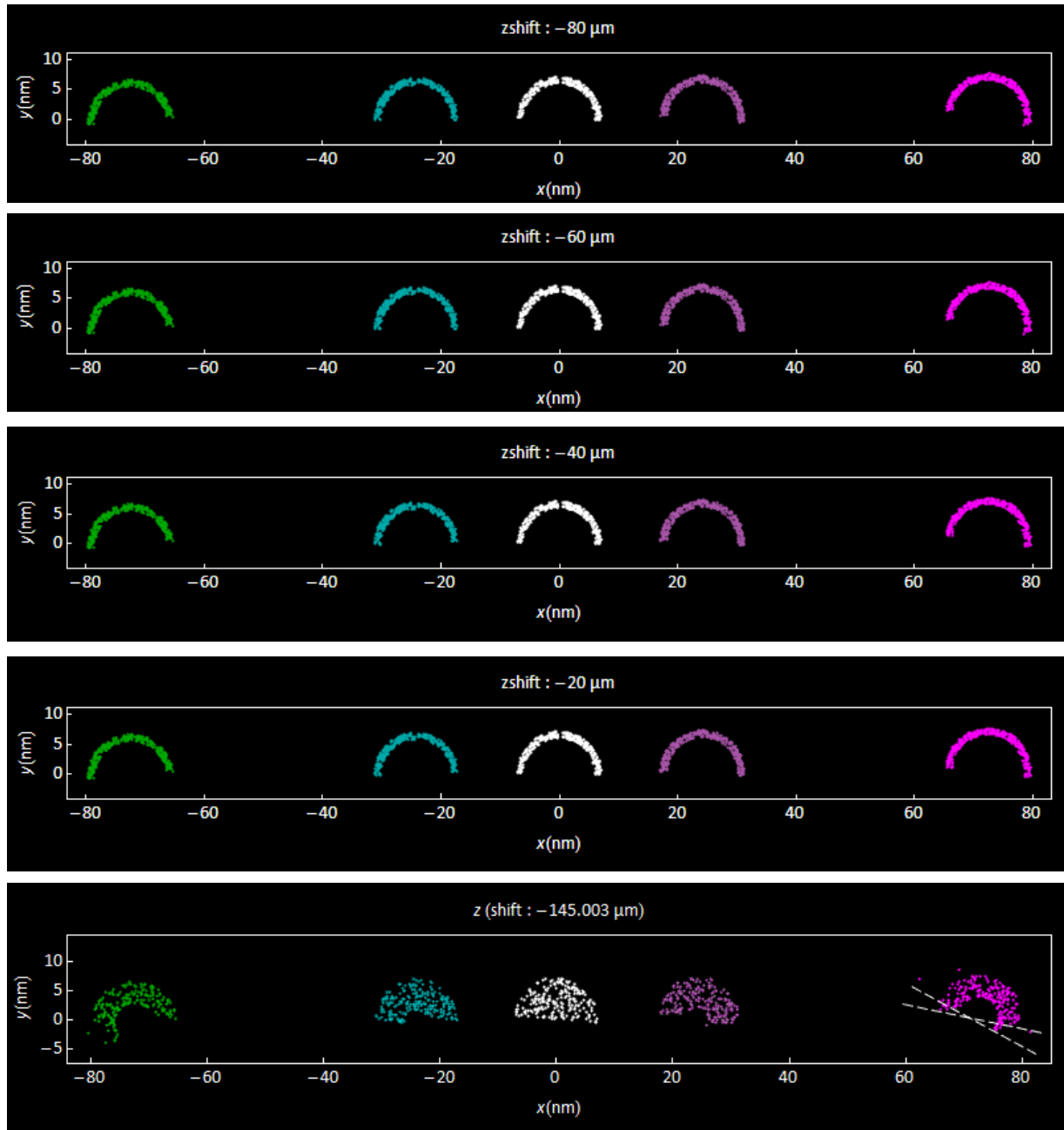


Figure 55: Ray tracing simulation, showing the electron distribution for the experimental parameters  $z_f = 5 \mu\text{m}$  and vortex orders  $m = 0, \pm 1, \pm 3$ , according to the colour scale used throughout the document for measured vortex orders. The  $z$ -shift values are indicated above the images. The last row shows a simulation result where the initial electrons were distributed over the whole area of a circle. An inner feature with clearly different rotation angle appears for the beams carrying OAM.

Figure 55 shows the positions of all together 2800 simulated electron trajectories for different orders of  $m$  at the observation plane, which was  $5 \mu\text{m}$  below the focal point for  $z$ -shift values between  $-85 \mu\text{m}$  and  $-25 \mu\text{m}$ . The semi-convergence angle was approximately of the order of the experimental



one and given to 1.35 mrad. For the simulation shown in Figure 55, the electrons were initially distributed over a ring of 1.2 nm thickness. The reason for that was twofold; to the first, it increases the electron density, which is important for better angular resolution and second it confines the electron trajectories to a vortex ring like structure in the observation plane with a thickness comparable to the experimental observed one. An interesting observation is, that when choosing the full circle area as initial electron distribution, the electron trajectories in the observation plane show increased azimuthal rotation angles, see Figure 55, last row. Quite like the experimental observed EVB do, as well as the simulation shown in Figure 53 does. With the “only” impediment being the absent diffraction features. Thus, the simulation resolves the overall shape of the measured vortex orders, but misses to show any complex inner structure, which is clearly due to the lack of diffraction effects in the used model. The lateral separation of single vortex orders by  $\sim 25$  nm and  $\sim 50$  nm, respectively, which can be assigned to diffraction effects at the holographic vortex mask grating, was artificially added to the simulation by choosing an initial skew angle for electrons with the same  $m$ . Note, that for the distribution of electron positions in Figure 55, last row, gained by full homogenous illumination, a minimum achievable radius shows up. The quantum mechanical explanation would employ the phase singularity reaching the centre of the EVB, classically it is the centrifugal force that counteracts and outweighs the centripetal force induced by the focusing action of the OL magnetic field at the focal point.

Faint azimuthal angle changes are visible for positive vortex orders, whereas negative orders do not show any significant change of their azimuth cutting angle, see Figure 55. This becomes clearer in Figure 56, where the calculated rotation angles are plotted against the  $z$ -shift value. In this figure the theory lines are represented by dashed lines. Their agreement with the semi-classical model is very good, showing the LS as well as the pure LR for high  $z$ -values. As expected, there is no discrepancy between the convergence angles of the simulation and the fitted semi-classical model. This can be understood as a result of the fact that the electrons' centroid was exactly the simulated electron path. The rectilinear shape of the simulated curve is a result of the limited number of electrons that can be used in the simulation, because of limited physical memory. This is comparable to the pixel size/resolution argument given in the methods section. For a certain achievable azimuthal angle resolution a certain pixel size is needed. Here, not the pixel size is defining the angular resolution, but the given electron density per area. It has been seen that higher electron densities smooth out the curve.

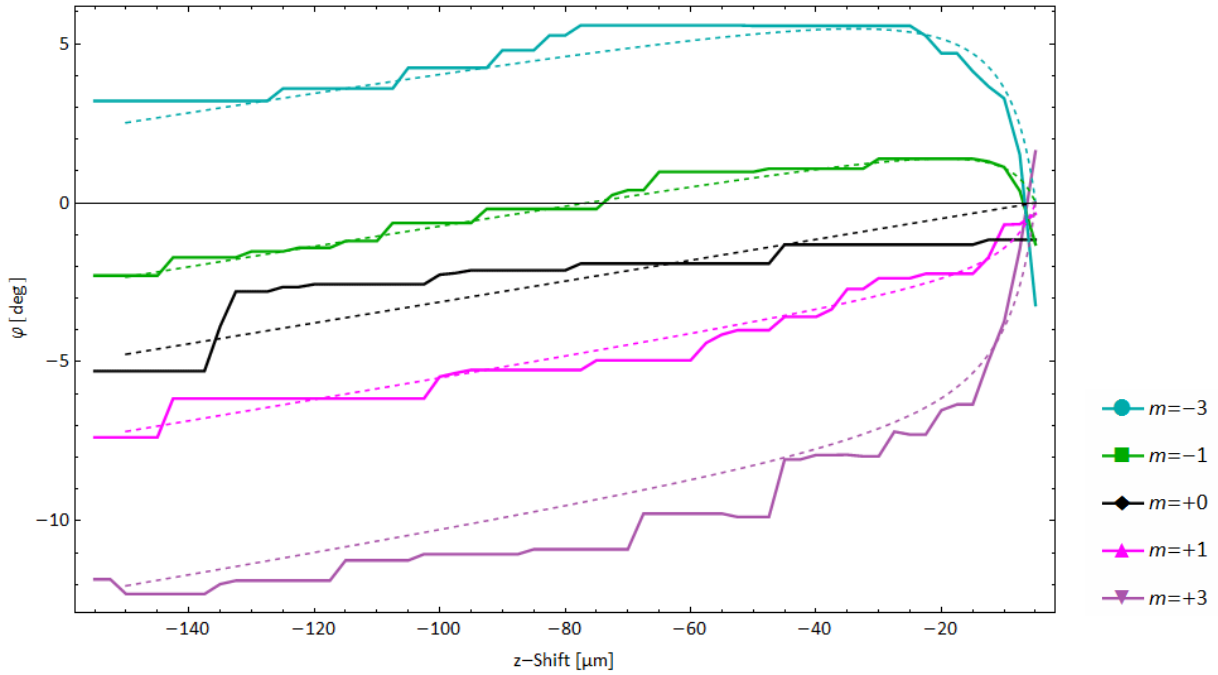


Figure 56: Numerically extracted azimuthal rotation angles of the simulated electron trajectories passing the KE. It was shifted to  $z$ -values between  $-150 \mu\text{m} < z < 0 \mu\text{m}$  for  $z_f = -5 \mu\text{m}$ . It was tried to come close to the experimental semi-convergence angle. The read out value was  $\theta = 1.35 \text{ mrad}$ . The dashed lines represent the semi-classical model for a magnetic field of  $B_z = 1.89 \text{ T}$ ,  $z_f = -5 \mu\text{m}$  and  $\theta = 1.35 \text{ mrad}$ .

The simulation results given before, deliver equally valid and well fitting descriptions of the cut-EVB azimuthal motion. The classical LF simulation resolves the experimental gained azimuthal angle dynamics best, due to the inclusion of the magnetic fields, whereas the wave-mechanical simulations explain the inner structure of EVB being due to diffraction effects.

## 4.2 STOC-Process Simulation Results

In this section the main results of the ray tracing simulation of the STOC-device will be presented.

Starting with an input beam of 1000 electrons randomly distributed on a ring with a mean radius of  $\rho = 100 \mu\text{m}$  and a thickness of  $20 \mu\text{m}$ , where the magnetic moments of the first 50% of the electrons are polarized parallel to the beam axis, whereas the last 50% are polarized anti-parallel, see Figure 57, left. The spin interaction is switched off, such that only the LF is simulated. Hue colour coding, according to Figure 57, right, is used to visualize the direction of the electron magnetic moment, such that green equals parallel magnetic moment and purple represents anti-parallel magnetic moment orientation, relative to the z-direction.

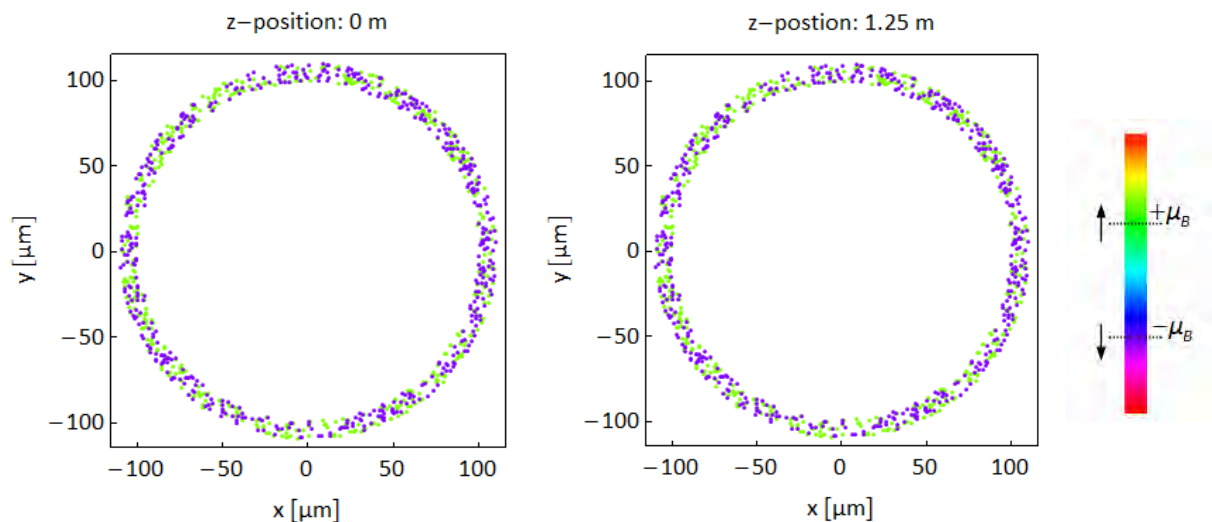


Figure 57: Left: Real space map of the ring-like electron distribution 0.2 m in front of the quadrupole. Middle: Real space map 5 cm after the electron traversed the quadrupole, which looks practically the same as left, indicating no visible beam deflection. Right: Hue colour scale indicating the ES orientation.

Comparing Figure 57, left, with Figure 57, middle, shows no visible change of the beam shape after traversing the quadrupole. This statement can be further refined by looking at the transverse velocity components  $v_{x,y}$  relative to the longitudinal electron velocity  $v_z$ , after the quadrupole, given in Figure 58, left. It was found that by slightly adjusting (tuning) the field strength of the quadrupole or alternatively, the acceleration voltage within  $\pm 100 \text{ meV}$ , the transverse electron trajectory deviations could be reduced well below  $10^{-12} \text{ rad}$ , see the so called reciprocal space map of the tuned Wien-filter device in Figure 58, left. Note that the input deviations were set to zero. This kind of simulation delivers a reference, to test if the basic Wien-filter behaviour is given.

For the present tuned Wien-filter case there are only faint signs for a preferred directional movement, see the circular shape in Figure 58; left. But as these deviations are of the order of femto-radians they can safely be neglected. The electrons' velocities are mainly randomly distributed over the whole azimuth with maximal velocities well below any observable threshold, see Figure 58, right. As will be seen later on, the introduction of ES and OAM to the simulation of the proposed STOC-device induces velocity variations at least four orders of magnitude larger than those observed here.

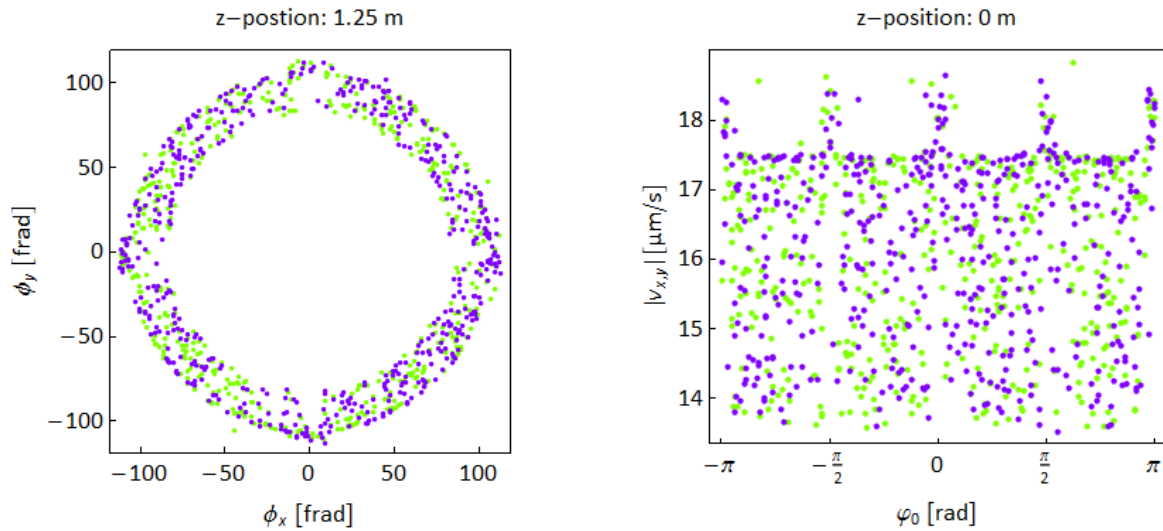


Figure 58: Left: Reciprocal space map of the output beam where only LF equations were used, the ES interaction was turned of, rendering transverse deviations lower than pico radians. Right: Shows the modulus of the transverse velocity components  $|v_{x,y}|$  of every single electron that was sent through the quadrupole as a dot plotted over its initial azimuthal angle,  $\varphi_0 = 0$  denotes the vertical line heading up from the quadrupole centre. The colour coding is the same as in Figure 57.

Thus, the LF is cancelled in the tuned quadrupole up to a very weak "noise" and as expected, no spin dependent pattern is visible.

The next step is to run the simulation with the electron magnetic moment switched on, whereas the electrons' OAM is still switched off. The quadrupoles' length is set to 1 m instead of 0.5 m as stated in the work of Karimi and colleagues. The deviation from the stated STOC-device length of 0.5 m is due to a missing factor two in the precession length formula given in the original publication. The mistake was corrected in an erratum to that publication. Additionally initial velocity components mimicking any fringe fields were not used at this point.

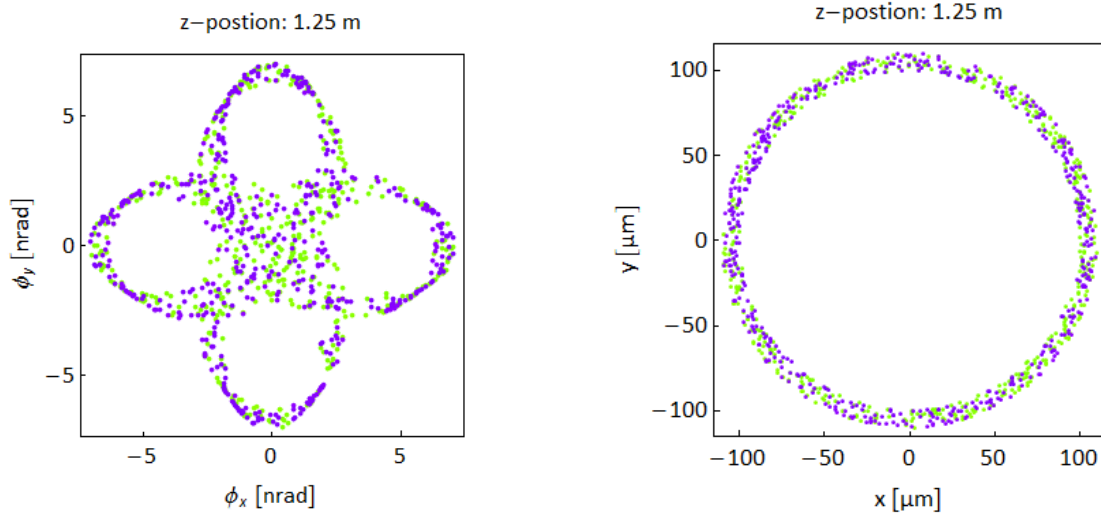


Figure 59: Left: Reciprocal space map of the simulated electrons after their flight through the quadrupole with the spin simulation switched on. Note that the deviation angles are extremely low. Right: It is clear from left, that the real space map of electron positions after passing the quadrupole shows no observable deviations.

To the simulation results given in Figure 59, left, quadrupole symmetry is evident but extremely weak. The angles of diffraction are comparable to those in a  $1 \text{ \AA}$  STEM probe. This is the reason why Figure 59, right, shows no visible changes to the input electron distribution in Figure 57, left. Therefore, the real space maps will not be shown for the following simulations. In addition, the random colour distribution in Figure 59 does not indicate an ES dependent spatial separation of electron positions.

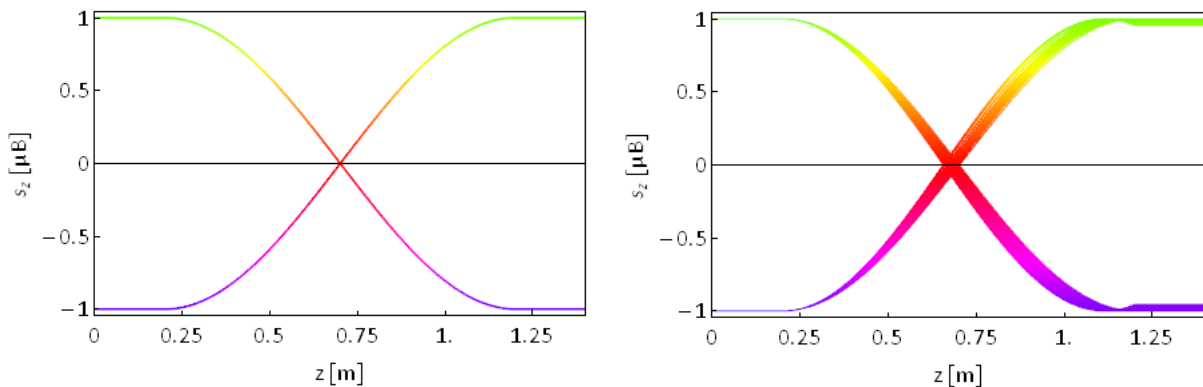


Figure 60: Left: ES evolution in units of the Bohr magneton over the course of the quadrupole for electrons located exactly at the  $100 \mu\text{m}$  ring. The ES flip by  $180^\circ$  is evident. Right: The same as left but for multiple electrons distributed on a  $20 \mu\text{m}$  thick rim with a mean radius of  $100 \mu\text{m}$ . All ES flip, but do spread over a certain range of magnetic moment of the order of 10%.

Even though the magnetic moments are not spatially separated after the passage of the quadrupole

Wien-filter the ES orientation of all electrons did indeed flip over, from parallel to anti-parallel and vice versa, see Figure 60. The trajectories in Figure 60, right, also indicate a noise around  $\pm s_z$  after their passage through the quadrupole; this is due to the thickness of the incident electron distribution of  $20 \mu\text{m}$ . It vanishes if the electrons are initially put exactly on the  $100 \mu\text{m}$  ring as can be seen in Figure 60, left. As a consequence of momentum conservation the magnetic moment flips induce transverse velocity components, shown in Figure 61, left. Together with Figure 62, left, showing the amount of azimuthal rotation after the electrons have passed the quadrupole device, one can conclude, that for certain azimuthal angles the electrons get also directed normal to the radius vector, which hints at an OAM gain at or around the azimuthal positions of  $0, \pm\pi/2$  and  $\pi$ .

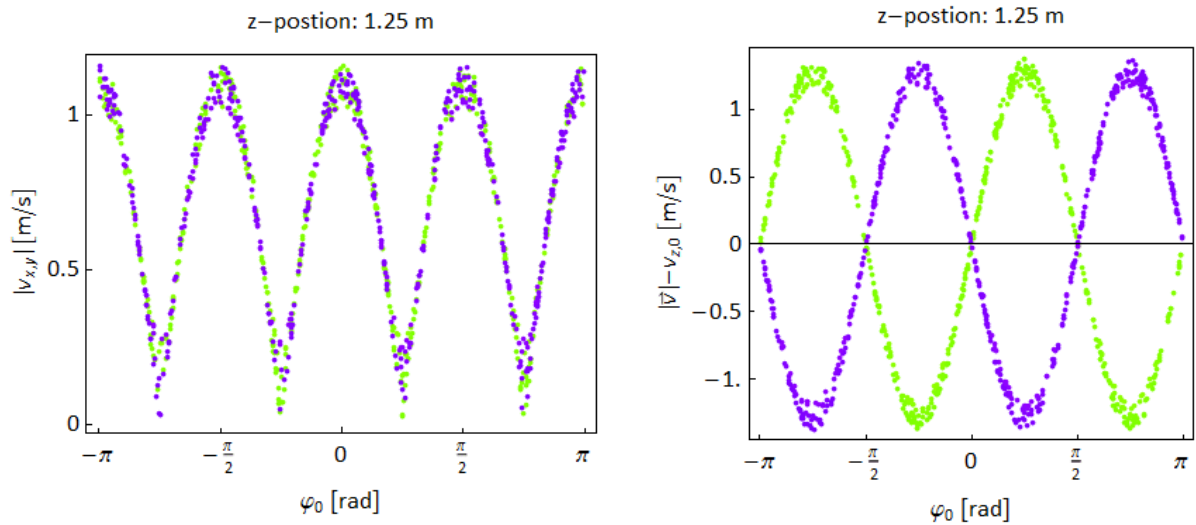


Figure 61: Left: Modulus of the transverse velocity components after the passage of the quadrupole plotted over the initial azimuthal angle  $\varphi_0$ . No transverse ES dependent distribution can be seen. Right: Modulus of the electron end velocity minus the initial velocity. Passing the quadrupole induces a longitudinal separation of ES depending on their azimuthal input position. The colour scaling is the same as in Figure 57.

The minima of the electron velocities plotted in Figure 61, left, correspond to a suppression of the transverse velocity at  $\pm\pi/4$  and  $\pm3\pi/4$ , this in turn induces a longitudinal momentum gain depicted in Figure 61, right, as well as a spatial separation of the spin states in the longitudinal direction, see Figure 62, right.

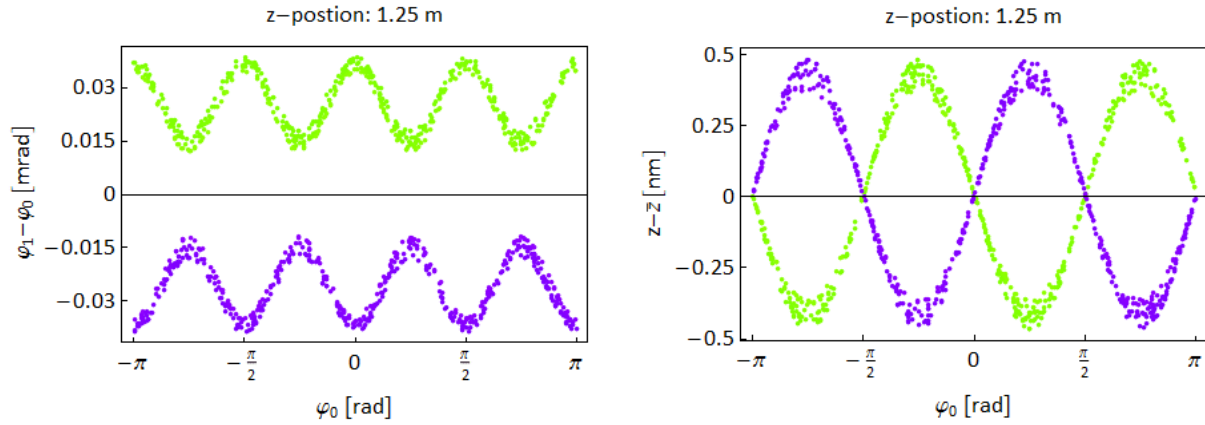


Figure 62: Left: The difference between the initial azimuthal angle and the final one, plotted over the initial azimuth  $\varphi_0$  should demonstrate that the transverse velocities gains given in Figure 61, left, are indeed directed in the direction of  $v_\varphi$ , and thus introduce OAM. Right: ES depended longitudinal path length variation for the two different spin states after simulating 7.55 ns and a mean path length of 1.25 m.

Above Figure 62, right, shows spatial separation of the electrons in z-direction, which could be interpreted as the longitudinal Stern-Gerlach effect, already described in 1997 by Herman (Batelaan, Gay et al. 1997, Gallup, Batelaan et al. 2001).

If this beam propagates further down the column through a magnetic round lens, e.g. the OL, faint ES dependent chromatic aberrations induce different focal points for parallel and anti-parallel oriented ES. Imaging the back focal plane of this lens slightly defocused, would show a focused inner ring of spin up electron states and a defocused outer ring of spin down electron states or vice versa changing to under-focus. The problem here is, besides the terrible low chromatic separation and disregarding fringe fields, that one would have to use special apertures in front of the quadrupole to select only the  $\pi/4$  and  $-3\pi/4$  or  $-\pi/4$  and  $3\pi/4$  electrons, because of the given field symmetry, which is further limiting this ideas' applicability as an alternative ES filter device.

Now, results of the simulation will be shown where the electron OAM has been activated. The OAM was introduced by adding a transverse electron velocity component following the formula (2.56). Note that the introduction of OAM of  $m = 1$  for an electron positioned at a radius of  $\rho = 100\mu\text{m}$  equals roughly 1 m/s azimuthal velocity. The fringing fields are still not included.

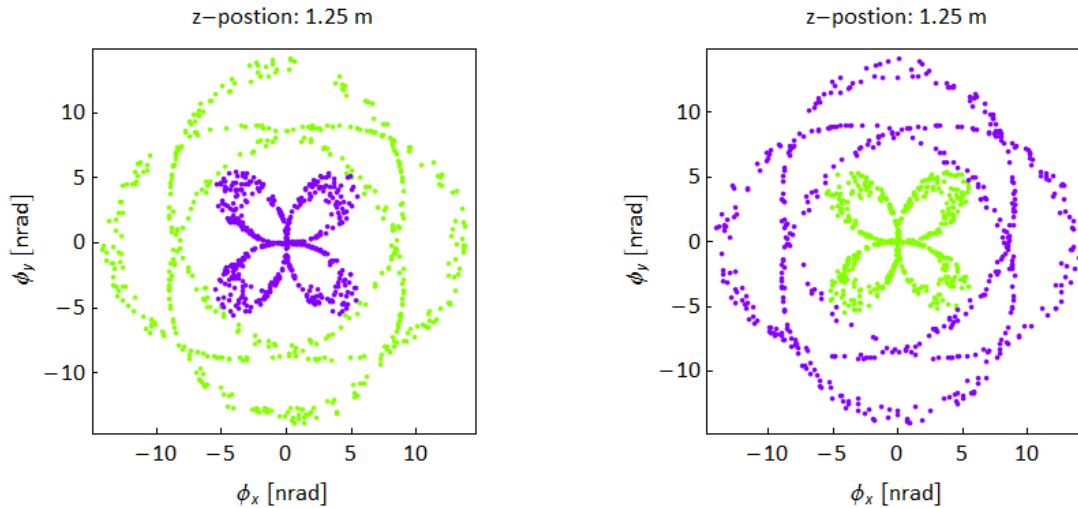


Figure 63: Left: Reciprocal space map after passing the quadrupole for electrons carrying initial positive OAM ( $m = +1$ ) demonstrating a clear ES dependent separation of the electron deflection angle. Right: Reciprocal space map for electrons having passed the quadrupole carrying the opposite sign of OAM. The ES are also clearly separated but with inversed ES sign. Note that the deflection angles doubled, but are still extremely low.

By imprinting the OAM on the electrons, the reciprocal space map changes dramatically, see Figure 63, though, it also yields quadrupole symmetry, there is a lateral ES dependent spatial separation of the electrons. All ES were flipped. This could be the proposed STOC-process stated by Karimi and co-workers. Although, an increase of deviation angles can be observed, they are still very low. Changing the input OAM state of the electrons, yields the same angular deviations, but with reversed ES sign, see Figure 63, right. The spin flips induce transverse velocity components, where, depending on the spin state, the OAM doubles or vanishes, further proving the presence of the STOC-process as described in the theory section, see Figure 64, left. These figures additionally point out that the spatial spin separation does not take place equally well for all electrons, especially those incident at  $0, \pm\pi/2$  and  $\pi$  are converted best, whereas those electrons incident at  $\pm\pi/4$  and  $\pm3\pi/4$  show little lateral separation. This can also be seen in the reciprocal space maps in Figure 63, where the electron deviations at the latter mentioned angles are nearly of the same order for both ES directions (seen by the touching of the inner fourfold quadrupole lobes with the outer rings). For these incident azimuthal angular positions the OAM is mainly converted into the longitudinal direction. If this outgoing electron beam is focused further down the column the ES states are spatially separated according to Figure 63, whereby the inner ring carries no OAM and the outer ring carries double the OAM of the  $m = 1$  input beam.



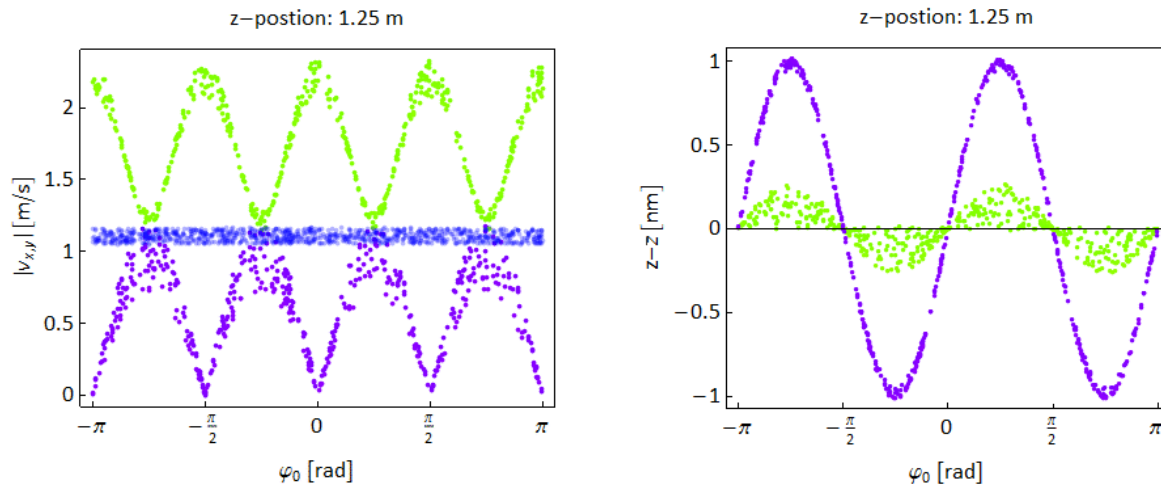


Figure 64: Left: Modulus of the transverse velocity components of electrons carrying positive OAM ( $m = +1$ ) plotted over the initial azimuth position  $\varphi_0$ . Note that the blue dots at approximately 1 m/s represent the initial angular velocity of each electron according to its OAM state. The passage of the quadrupole doubles the OAM for initially spin down electrons, when incident at certain azimuthal positions, whereas the OAM vanishes for initially spin up electrons, when incident on certain azimuthal positions. Right: Longitudinal path length variation for the same experiment, showing the longitudinal separation of spin states at those positions where no OAM change occurred.

Concerning the question, if and how the reciprocal space maps given in this section correlate to the plot of the norm of the transverse velocity components, it is evident that plotting the norm of the transverse velocity components of one electron after passing the quadrupole over its initial input angle, is something different than plotting the bare transverse velocity components of the single electrons after they passed the quadrupole. For example, Figure 65, compares the polar representation, left, with a plot of the transverse velocity components, right. The similarity of Figure 65, right, with the reciprocal space map in Figure 63, can be easily seen.

At this point the SCOFF model or method can be introduced by adopting the initial longitudinal velocity of each electron according to expression (3.2) in section 3.2.

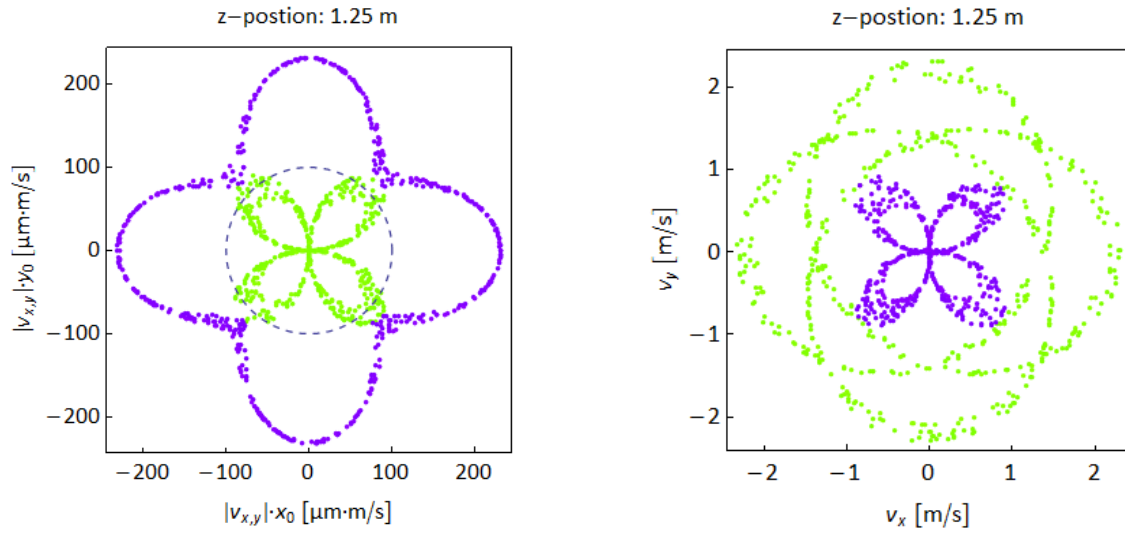


Figure 65: Left: The norm of the transverse velocity components acquired after the passage of the quadrupole device of each electron was taken to scale its initial position on the  $100 \mu\text{m}$  ring, marked as a dashed circle. If all electrons had not gained any transverse deviation they would be plotted at the marked circle. Right: A plot showing the bare transverse velocity components  $v_x$  and  $v_y$ , without the division by the electron velocity in  $z$ -direction, being clearly different to left.

As already stated there, the transverse velocity components stay untouched, because of the assumption that the fringe fields abruptly terminate. First, the question concerning the order of the fringe field effect shall be addresses. This can be done by simply using the proposed field strengths for the  $z$ -component of the quadrupole vector potential given by Karimi and co-workers and putting it into expression (3.2), such that the magnitude of longitudinal velocity change at the radius of the simulated ring of  $100 \mu\text{m}$ , can be given to,

$$\Delta v_{\text{SCOFF}}(\rho = 100 \mu\text{m}) = \frac{e \cdot A_z(\rho = 100 \mu\text{m})}{m_e} \approx \frac{10^{-19} \text{As} \cdot \pm 10^{-6} \text{Tm}}{10^{-30} \text{kg}} = \pm 10^5 \frac{\text{m}}{\text{s}}. \quad (4.2)$$

With that, the induced velocity changes are roughly five orders of magnitude larger than those induced by the STOC-process. Figure 66, left, gives the variation of the  $\Delta v_{\text{SCOFF}}$  over the initial azimuthal angle  $\varphi$  following the vector potential variation. The right part of that figure depicts the effect of introducing  $\Delta v_{\text{SCOFF}}$  on the electron velocity distribution at the output of the quadrupole. The beam conserves its four-fold symmetry, but gets deflected to angles of the order of  $0.4 \text{ mrad}$ , which is, not surprisingly, five orders of magnitude larger than the afore seen ES flip induced deviations. The same is true for the transverse velocity components given in Figure 67, right. The spatial ES separation is no more visible.

This can also be seen in the zoom in of Figure 66, right, in Figure 67, left.

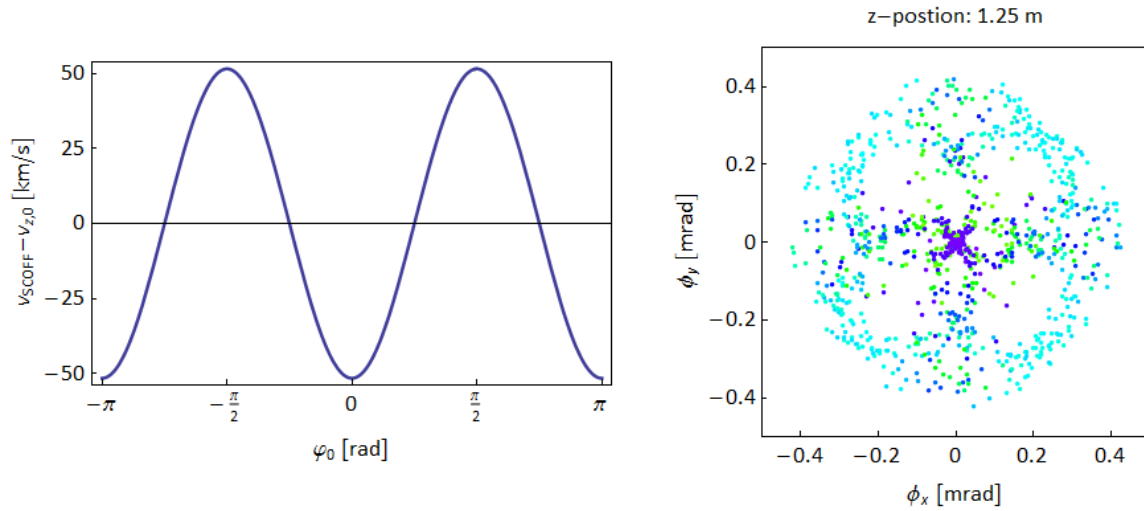


Figure 66: Left: Longitudinal electron velocity deviations induced by the SCOFF model, plotted over the initial azimuth  $\phi_0$ . Note the scale  $\sim 50$  km/s, compared to the ES flip induced velocities of 1 m/s. Right: Reciprocal space map showing the electron deviations after passing the quadrupole with initial OAM and SCOFF model adopted initial longitudinal velocities. Vast angular deviations are introduced minimizing the ES flip probability.

If there is a spatial ES separation, its efficiency is estimated to be very low. Because the simulation was done with 1000 electrons and practically none of them reached deviations as low as 10 nrad, where the ES separation would show up.

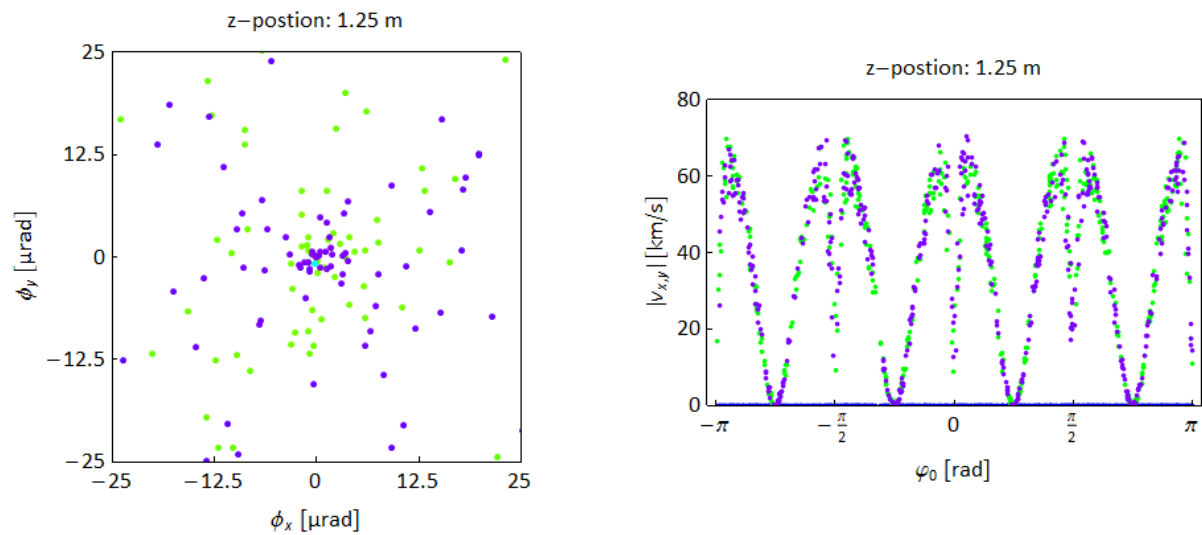


Figure 67: Left: Zoom in of the reciprocal space map given in Figure 66, right, showing also no clear spatial separation of ES. Right: The modulus of the transverse velocity components for different ES states plotted over the initial azimuth  $\phi_0$  does also not show any separation of ES dependent effects.

Karimi and his colleagues stated that the introduction of fringe fields in the form of the SCOFF model is not crucial. This assumption can not be backed by the above given simulations of the proposed ES

filter device. As the variation of the longitudinal velocity component in this simple model, is of the order of 60 km/s and induces transverse velocity variations of the same order, it completely overrides the STOC-process, except for the positions  $\pm\pi/4$  and  $\pm3\pi/4$ , where the beam shape is conserved. Although, at this positions the spatial spin separation is not that strong as at the places in between.

This calls for rethinking the used fringe model, as well as the whole scheme of the ES-filtering with quadrupoles. If it turns out to be a valid fringe field approximation, it would be interesting if the ansatz utilizing the chromatic aberrations of different spin states, mentioned above, could be more favourable.

## 5 Conclusion and Outlook

As stated in the introduction, this work's aim was to deepen our understanding of EVB behaviour in the magnetic field. This was tried by approaching the topic from both sides, the theoretical one in doing numerical simulations and introducing a simple semi-classical model, as well as from the experimental one, by doing multiple cut-EVB z-shift experiments. The results of these approaches will be shown in the following summarizing list:

- The results of the wave-mechanical numerical investigations explained the complex inner structure as being due to diffraction effects at the cutting KE and by that helped to improve and justify the used azimuthal angle determination method, such that faint LS rotations could be resolved. As the magnetic field was not yet included, their rotational dynamics correlate to the well known Gouy-phase rotations of OVB.
- Additionally, the results of the wave-mechanical numerical investigations also showed a discrepancy between the wave-mechanical convergence angle and the one used in the semi-classical model. It was of the same order like the one retrieved as a best fit to the experimental data. Thus, indicating that this discrepancy could be a result of diffraction effects. This should be further clarified.
- The ray tracing numerical simulations, mimicking the experimental setup to unveil the EVB rotational dynamics in the magnetic OL field, confirmed the observed complex rotational behaviour found in the experiments, including LR at high z-shift values and its' splitting into three different rotational states, according to 0, LR, 2LR, occurring roughly at the predicted magnetic beam waist.
- The ray tracing numerical simulations adopted to replicate a proposed ES polarizing Wien-filter with quadrupolar field symmetry from Karimi and collaborators (Karimi, Marrucci et al. 2012b) were successful in producing spatial ES separation. Also the proposed STOC-process has been observed. Additionally, it could be shown that the influence of fringe fields included by the SCOFF model can not be neglected as stated in their work. Their magnitude completely overrides the ES polarization. Also, it has been found that the proposed length of the quadrupole Wien-filter device must be extended to 1 m, as opposed to 0.5 m, due to a missing factor 2 in the precession length. This finding lead to an erratum of their original Physical Review Letters paper (Karimi, Marrucci et al. 2012a). Interestingly, the longitudinal Stern-Gerlach effect envisaged by Batelaan and co-workers in 1997, also showed up in the

simulation.

- The introduction of a semi-classical model, qualitatively, as well as quantitatively describes the experimentally found data on EVB rotations in magnetic fields for the whole accessible z-shift range, while Bliokhs' and co-workers' derivation concentrated only at a certain characteristic beam radius,  $\rho = \sqrt{m} \cdot w_M$ , corresponding to a rather narrow z-shift region. Moreover, it delivers an intuitive picture of the involved processes. The convergence angles had to be adopted according to the Ehrenfest theorem. As already stated above, the observed deviation of the theoretical predicted convergence angle for the centroid motion is possibly due to diffraction effects.
- The set of acquired experimental data consistently shows complex rotational dynamics; it can be stated that the picture given in Figure 6, in section 2.1.3, of an electron spiralling through the magnetic field with a constant slope is oversimplified and holds no longer true, when EVB character is imprinted to the electrons. Figure 68 tries to boil down the mechanical explanations given by the semi-classical model, as well as the experimental findings on the intimate relation between EVB azimuthal rotation dynamics and a quasi homogeneous magnetic field.

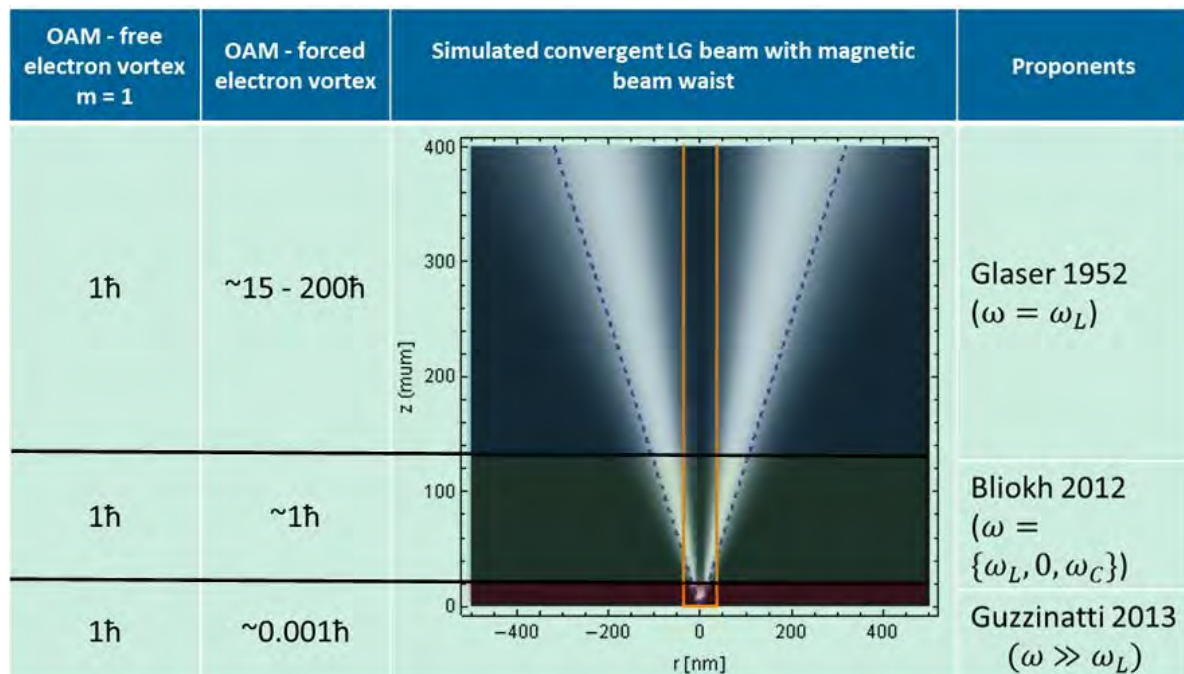


Figure 68: Shows a graphic summing up the findings of cut-EVB rotation experiments for the whole accessible z-shift region by comparing the OAM of the two complementary vortex phenomena, rotational and irrotational vortices.

There, in the third column, a cross section of an EVB represented by a convergent LG mode carrying OAM equivalent to one Plancks' constant can be seen, ranging from  $z = 400 \mu\text{m}$  to  $z = 0 \mu\text{m}$ . The blue dashed line indicates the beam radius and the two orange lines indicate the magnetic beam waist  $w_M$ . In principal, the experimental findings, contained herein, suggest that there are three main regions exhibiting clearly different rotational dynamics that smoothly change over from one into the other. That are, the long known LR regime investigated and described by Glaser (Glaser 1952) present at high  $z$ -shift values. There, the influence of the magnetic field on the incident EVB is roughly 100 times larger than that of the imprinted OAM, thus LR dominates for all vortex orders, which were investigated. Using higher OAM states, as they have been created by McMorran (McMorran, Agrawal et al. 2011), would only shift that region further away from the focus. Then, as the beam converges, approaching radial extensions comparable to the magnetic beam waist, the influence of the magnetic field forced vortex decreases considerable, such that both phenomena add up to yield LS behaviour, with its three distinct rotational velocities,  $0, \omega_L, \omega_C$ . These states have been recently predicted by Bliokh and co-workers (Bliokh, Schattschneider et al. 2012). Their experimental realization described herein is the first one reported, therefore it has been submitted to publication (Schattschneider, Schachinger et al. submitted). Further converging the EVB below the magnetic beam waist size renders the effects of the magnetic OL field negligible, while at the same time angular momentum conservation drastically increases the azimuthal rotation dynamics of the electron, such that fast CW and CCW rotations occur, depending on the sign of the incident vortex order. This has been recently experimentally proved by Guzzinati and colleagues by a similar technique as the one used herein (Guzzinati, Schattschneider et al. 2013).

As new findings and insights also raise new questions, here is a short collection of them, as well as an outlook.

Experimental detection of the LS is far from trivial using the method described in this work, to improve that, measurements of the thickness profile of the used Si-KE should be done to better understand the intensity drop of the cut-EVB edge onsets. Also the data analysis itself, which relied on the visual judgement of the experimentalist, could be replaced by an algorithm.

Moreover, other detection techniques could be possibly incorporated. For instance, in differential phase contrast microscopy angular deviations down to the  $\mu\text{rad}$  scale can be detected (Lohr, Schregle et al. 2012). Or, the use of a spiral holographic vortex mask that creates the EVB orders not laterally

separated but vertically separated by a certain defocus value could be beneficial (Verbeeck, Tian et al. 2012). Another idea to measure the LS without the use of a KE would incorporate the fact that a real space skewness of the electron beam in the front focal plane of the OL shows up as a shift in the diffraction pattern in its back focal plane. This is routinely used in electron microscopy to acquire dark field images. Thus, using the non-rotating LS to illuminate, e.g. a Si-crystal, would exhibit a slightly different diffraction pattern, as opposed to the one using the LS rotating with cyclotron frequency. For comparison, see (Leach, Keen et al. 2006), who were directly measuring the skew angle of the Poynting vector of an OVB.

It has been observed that, even without the KE cutting method, there are visual indications in the intensity distribution of the EVB for the transition from the rather slow Larmor- and cyclotron rotations to the much faster Gouy-phase regime in the form of sudden image deformations. The electron intensity distribution of an EVB of the size of the magnetic beam waist looks much like a shadow image of the holographic vortex mask. This image turns rapidly into the shown ring-like structure, when further converging the EVB, which could be a sign of strong acceleration of azimuthal rotation.

Moreover, it was found qualitatively that multi-ringed EVB show faster rotating inner rings, e.g. see Figure 44, this has also been observed for OVB (Arlt 2003), further investigations could clarify their detailed nature.

Also, Cui and colleagues have demonstrated that obstructed OVB show angular diffraction effects due to the Gouy-phase, comparable to single slit diffraction (Cui, Wang et al. 2012). In principal the EVB z-shift series have also shown peculiar inner structures, which were assigned to diffraction effects at the KE. Further work on that could shed some light on EVB angular diffraction.

Concerning the simulated STOC-process, it would be interesting to further investigate, how real, or more realistic fringe fields would change the output of that device. For example in an follow up work to that presented herein, a so called soft-fringe approximation was introduced (Grillo, Marrucci et al. 2013). It would also be interesting, if higher order multipoles could improve the ES separation. On the other side the question arises, if there are nanoparticles/(quasi-) crystallites which exhibit radial oriented lattice planes similar in symmetry to the q-plates proposed by Karimi and co-workers that would show ES separation up on their illumination by EVB.

As already mentioned in the introduction, EVB may be used for the manipulation of objects in the nanometre and sub-nanometre regime, the findings herein suggest that not only the irrotational vortex character of holographically produced EVB could be used for particle manipulation, but also the magnetic OL induced forced vortex. This one is orders of magnitude stronger for higher radii



electron beams. Indeed particle manipulation has been shown by just using the electron beam without EVB character (Zheng, Mirsaidov et al. 2012). As some questions concerning the origin of the observed effect remained open, it may be that the OL forced vortex could help to clarify that.

Additionally, the insights of this work could also be applied more practical to measure the longitudinal magnetic fields of the OL with accuracy of the order of 1.5 %.

Also, the observation in the 1970's by Beck and co-workers that the production of millimetre radio waves inside a microwave cavity immersed in a static homogenous magnetic field was possible at fractions of their associated cyclotron magnetic field values, could be an early realization and application of LS and should be studied further (Beck and Mills 1971).

So far, imaging the dynamics of LS reported herein has been shown for the quasi homogenous magnetic field of the OL thus, paving the way for investigations of a quite similar effect predicted to occur inside solid state matter, called OAM Faraday rotation (Greenshields, Stamps et al. 2012). This effect could provide the possibility of spatially resolved measurements of longitudinal magnetic field components in solids.

## 6 Bibliography

Arlt, J. (2003). "Handedness and azimuthal energy flow of optical vortex beams." *Journal of Modern Optics* **50**(10): 1573-1580.

Batelaan, H., Gay, T. J. and Schwendiman, J. J. (1997). "Stern-Gerlach Effect for Electron Beams." *Physical Review Letters* **79**(23): 4517-4521.

Baumann, S. M., Kalb, D. M., MacMillan, L. H. and Galvez, E. J. (2009). "Propagation dynamics of optical vortices due to Gouy phase." *Optics Express* **17**(12): 9818.

Bazhenov, V. Y., Vasnetsov, M. V. and Soskin, M. S. (1990). "Laser beams with screw dislocations in their wavefronts." *JETP Letters* **52**(8): 429-431.

Béché, A., Boxem, R. V., Tendeloo, G. V. and Verbeeck, J. (2013). "Magnetic monopole field exposed by electrons." arXiv: 1305.0570.

Beck, A. H. W. and Mills, W. P. C. (1971). "Millimetre-wave generator working at half the cyclotron resonance frequency." *Electronics Letters* **7**(18): 533-534.

Beck, A. H. W. and Mills, W. P. C. (1973). "Millimetre-wave generator that uses a spiralling electron beam." *Proceedings of the IEEE* **120**(2): 197-205.

Bergmann and Schäfer (2004). Band 3: Optik, Wellen- und Teilchenoptik.

Berndt, M. (2005). Online Lecture Notes: "Seminar zur Vorlesung Magnetismus II, Spinpolarisierte Elektronen". [http://www.anphy.uni-duesseldorf.de/ag\\_getzlaff/Veranstaltungen/Magnetismus/Bilder/Spinpolarisierte\\_Elektronen.pdf](http://www.anphy.uni-duesseldorf.de/ag_getzlaff/Veranstaltungen/Magnetismus/Bilder/Spinpolarisierte_Elektronen.pdf).

Bliokh, K. Y., Bliokh, Y. P., Savel'ev, S. and Nori, F. (2007). "Semiclassical Dynamics of ElectronWave Packet States with Phase Vortices." *Physical Review Letters* **99**: 190404.

Bliokh, K. Y., Ostrovskaya, E. A., Alonso, M. A., Rodríguez-Herrera, O. G., Lara, D. and Dainty, C. (2011). "Spin-to-orbital angular momentum conversion in focusing, scattering, and imaging systems." *Optics Express* **19**(27).

Bliokh, K. Y., Schattschneider, P., Verbeeck, J. and Nori, F. (2012). "Electron Vortex Beams in a Magnetic Field: A New Twist on Landau Levels and Aharonov-Bohm States." *Physical Review X* **2**: 041011.

Bongs, K., Burger, S., Dettmer, S., Hellweg, D., Arlt, J., Ertmer, W. and Sengstock, K. (2001). "Waveguide for Bose-Einstein condensates." *Physical Review A* **63**(3): 031602.

Busch, H. (1926). "Berechnung der Bahn von Kathodenstrahlen im axialsymmetrischen elektromagnetischen Felde." *Annalen der Physik* **81**: 974.

- Calbick, C. J. (1944). "Historical Background of Electron Optics." *Journal of Applied Physics* **15**: 685.
- Christenson, K. K. and Eades, J. A. (1986). "On "Parallel" Illumination in the Transmission Electron Microscope." *Ultramicroscopy* **19**: 191.
- Clark, L., Béch e, A., Guzzinati, G., Lubk, A., Mazilu, M., Boxem, R. V. and Verbeeck, J. (2013). "Exploiting Lens Aberrations to Create Electron-Vortex Beams." *Physical Review Letters* **111**: 064801.
- Cole, R. (2006). Introduction to Classical Fluids, Chapter 3: Rotational Flows: Circulation and Turbulence. Divergence, Curl, and Other Things That Go Bump In the Night. [http://maxwell.ucdavis.edu/~cole/phy9b/notes/fluids\\_ch3.pdf](http://maxwell.ucdavis.edu/~cole/phy9b/notes/fluids_ch3.pdf).
- Cui, H. X., Wang, X. L., Gu, B., Li, Y. N., Chen, J. and Wang, H. T. (2012). "Angular diffraction of an optical vortex induced by the Gouy phase." *Journal of Optics A: Pure and Applied Optics* **14**: 055707.
- Davis, B. S. and Kaplan, L. (2013). "Transverse phase variation of a Gaussian beam." *Journal of Optics* **15**: 075706.
- Dellby, N., Bacon, N. J., Hrn irik, P., Murfitt, M. F., Skone, G. S., Szilagy i, Z. S. and Krivanek, O. L. (2011). "Dedicated STEM for 200 to 40 keV operation." *European Physical Journal Applied Physics Letters* **54**: 33505.
- Demtr oder, W. (2005a). *Experimentalphysik Band 1 Mechanik und W arme*, Springer.
- Demtr oder, W. (2005b). *Experimentalphysik Band 3 Atome, Molek ule und Festk orper* Springer.
- Ehrenfest, P. (1927). "Bemerkung  uber die angen aherte G ultigkeit der klassischen Mechanik innerhalb der Quantenmechanik." *Zeitschrift f ur Physik A* **45**(7-8): 455-457.
- Erni, R., Rossell, M. D., Kisielowski, C. and Dahmen, U. (2009). "Atomic-Resolution Imaging with a Sub-50-pm Electron Probe." *Physical Review Letters* **102**: 096101.
- Eyidi, D., H ebert, C. and Schattschneider, P. (2006). "Short note on parallel illumination in the TEM." *Ultramicroscopy* **106**: 1144.
- FEI-Company-Datasheet (2007). Product Data: Tecnai™ G2 20, Number: 00DS-TE0114 07/07. F. Company.
- FEI (2013) Product Data Sheet: Titan ETEM G2 S-Twin Objective Lens Gap width 5.4 mm.
- Findlay, W. J. (1951). "The phase and group paths of radio waves returned from region E of the ionosphere." *J. Atmos. Terrest. Phys.* **1**: 353-366.
- Floss, I. (2013). "Project Work: Study of the Propagation of Convergent Electron Vortex Beams." TU-Vienna - Institute for Solid State Physics.
- Franke-Arnold, S., Allen, L. and Padgett, M. (2008). "Advances in optical angular momentum." *Laser & Photonics Reviews* **2**(4): 299-313.
- Franke-Arnold, S., Gibson, G., Boyd, R. W. and Padgett, M. J. (2011). "Rotary Photon Drag Enhanced

by a Slow-Light Medium." *Science* **333**: 65-67.

Freitag, B., Kujawa, S., Mul, P. M., Ringnalda, J. and Tiemeijer, P. C. (2005). "Breaking the spherical and chromatic aberration barrier in transmission electron microscopy." *Ultramicroscopy* **102**: 209.

Gallatin, G. M. and McMorran, B. (2012). "Propagation of vortex electron wave functions in a magnetic field." *Physical Review A* **86**: 012701.

Gallup, G. A., Batelaan, H. and Gay, T. J. (2001). "Quantum-Mechanical Analysis of a Longitudinal Stern-Gerlach Effect." *Physical Review Letters* **86**(20): 40508-40511.

Gerlach, W. and Stern, O. (1922). "Der experimentelle Nachweis der Richtungsquantelung im Magnetfeld." *Zeitschrift für Physik* **9**: 349-352.

Glaser, W. (1952). *Grundlagen der Elektronenoptik*. Vienna, Springer-Verlag Wien.

Greenshields, C., Stamps, R. L. and Franke-Arnold, S. (2012). "Vacuum Faraday effect for electrons." *New Journal of Physics* **14**: 11.

Grillo, V. (2013). Converter of orbital angular momentum into spin momentum for the polarisation of particle beams. US-Patent. United States.

Grillo, V., Marrucci, L., Karimi, E., Zanella, R. and Santamato, E. (2013). "Quantum simulation of a spin polarization device in an electron microscope." *New Journal of Physics* **15**.

Grover A. Swartzlander, J. and Hernandez-Aranda, R. I. (2007). "Optical Rankine Vortex and Anomalous Circulation of Light." *Physical Review Letters* **99**: 163901.

Guzzinati, G., Schattschneider, P., Bliokh, K. Y., Nori, F. and Verbeeck, J. (2013). "Observation of the Larmor and Gouy Rotations with Electron Vortex Beams." *Physical Review Letters* **110**: 093601.

Haider, M., Uhlemann, S., Schwan, E., Rose, H., Kabius, B. and Urban, K. (1998). "Electron microscopy image enhanced." *Nature* **392**: 768.

Hamazaki, J., Mineta, Y., Oka, K. and Morita, R. (2006). "Direct observation of Gouy phase shift in a propagating optical vortex." *Optics Express* **14**(18): 8382-8392.

Hat'nCoat (2009). "Sketch, showing the TEM objective lens." Retrieved 01.06.2013, 2013, from <http://upload.wikimedia.org/wikipedia/commons/5/50/TEM-lens.svg>.

He, H., Friese, M. E. J., Heckenberg, N. R. and Rubinsztein-Dunlop, H. (1995). "Direct Observation of Transfer of Angular Momentum to Absorptive Particles from a Laser Beam with a Phase Singularity." *Physical Review Letters* **75**(5): 826-829.

Heckenberg, N. R., McDuff, R., Smith, C. P. and White, A. G. (1992). "Generation of optical phase singularities by computer-generated holograms." *Optics Letters* **17**(3): 221-223.

Hemsing, E., Knyazik, A., Dunning, M., Xiang, D., Marinelli, A., Hast, C. and Rosenzweig, J. B. (2013). "Coherent optical vortices from relativistic electron beams." *Nature Physics* **9**: 549-553.

- Jesacher, A., Schwaighofer, A., Fürhapter, S., Maurer, C., Bernet, S. and Ritsch-Marte, M. (2007). "Wavefront correction of spatial light modulators using an optical vortex image." *Optics Express* **15**(9): 5801-5808.
- Karimi, E., Grillo, V., Boyd, R. W. and Santamato, E. (2013). "Generation of a spin-polarized electron beam by multipoles magnetic field." arXiv.
- Karimi, E., Marrucci, L., Grillo, V. and Santamato, E. (2012a). "Erratum: Spin-to-Orbital Angular Momentum Conversion and Spin-Polarization Filtering in Electron Beams, [Phys. Rev. Lett. 108, 044801 (2012)]." *Physical Review Letters* **109**: 209901.
- Karimi, E., Marrucci, L., Grillo, V. and Santamato, E. (2012b). "Spin-to-Orbital Angular Momentum Conversion and Spin-Polarization Filtering in Electron Beams." *Physical Review Letters* **108**: 044801.
- Karimi, E., Marrucci, L., Grillo, V. and Santamato, E. (2012c). "Supplementary material for Spin-to-orbital angular momentum conversion and spin-polarization filtering in electron beams." *Physical Review Letters* **108**: 044801.
- Knöner, G., Parkin, S., Nieminen, T. A., Vincent L. Y. Loke, Heckenberg, N. R. and Rubinsztein-Dunlop, H. (2007). "Integrated optomechanical microelements." *Optics Express* **15**(9): 5521-5530.
- Kuppens, S., Rauner, M., Schiffer, M., Sengstock, K., Ertmer, W., Dorsselaer, F. E. v. and Nienhuis, G. (1998). "Polarization-gradient cooling in a strong doughnut-mode dipole potential." *Physical Review A* **58**(4): 3068-3079.
- Kuwahara, M., Ichihashi, F., Asano, H., Nakanishi, T., Kusunoki, S., Tanaka, N., Takeda, Y., Saitoh, K. and Ujihara, T. (2004). "Development of Spin-Polarized Pulsed TEM." *Journal of Physics: Conference Series* **371**: 012004.
- Leach, J., Keen, S., Padgett, M. J., Saunter, C. and Love, G. D. (2006). "Direct measurement of the skew angle of the Poynting vector in a helically phased beam." *Optics Express* **14**(25): 11919-11924.
- Leach, J., Yao, E. and Padgett, M. J. (2004). "Observation of the vortex structure of a non-integer vortex beam." *New Journal of Physics* **6**: 71.
- Löffler, S. and Schattschneider, P. (2012). "Elastic propagation of fast electron vortices through crystals." *Acta Crystallographica Section A* **A68**: 443-447.
- Löffler, W., Exter, M. P. v., Hooft, G. W. t., Nienhuis, G., Broer, D. J. and P. Woerdman, J. (2011). "Search for Hermite-Gauss mode rotation in cholesteric liquid crystals." *Optics Express* **19**(14).
- Lohr, M., Schregle, R., Jetter, M., W, C., Scholz, F. and Zweck, J. (2012). "Differential phase contrast 2.0—Opening new “fields” for an established technique." *Ultramicroscopy* **117**: 7-14.
- Lubk, A., Clark, L., Guzzinati, G. and Verbeeck, J. (2013). "Topological analysis of paraxially scattered electron vortex beams." *Physical Review A* **87**: 033834.

- Lugt, H. J. (1979). *Wirbelströmung in Natur und Technik*. Karlsruhe, G. Braun.
- Manni, F., Lagoudakis, K. G., Paraíso, T. K., Cerna, R., Léger, Y., Liew, T. C. H., Shelykh, A., Kavokin, A. V., Morier-Genoud, F. and Deveaud-Plédran, B. (2011). "Spin-to-orbital angular momentum conversion in semiconductor microcavities." *Physical Review B* **83**.
- Manzo, C., Paparo, D. and Marrucci, L. (2006). "Light-induced rotation of dye-doped liquid crystal droplets." *Physical Review E* **73**.
- Marrucci, L., Manzo, C. and Paparo, D. (2006). "Optical Spin-to-Orbital Angular Momentum Conversion in Inhomogeneous Anisotropic Media." *Physical Review Letters* **96**: 163905.
- McMorran, B. J., Agrawal, A., Anderson, I. M., Herzing, A. A., Lezec, H. J., McClelland, J. J. and Unguris, J. (2011). "Electron Vortex Beams with High Quanta of Orbital Angular Momentum." *Science* **331**: 192-195.
- McMorran, B. J., Pierce, J., Yahn, T. and Harvey, T. (2013). *Investigations of Electron Vortex Beams Carrying Orbital Angular Momentum*. Multi Conference on Systems and Control (MSC 2013).
- Meyer, J. C., Girit, C. O., Crommie, M. F. and Zettl, A. (2008). "Imaging and dynamics of light atoms and molecules on graphene." *Nature* **454**: 07094.
- Mills, W. P. C. (1971). *Millimetre wave generation by a helical electron beam*, University of Cambridge.
- Mitutoyo (2008). *Oberflächen-Rauheitsmessung PR1269(2)-Praktische Hinweise für Labor und Werkstatt*. M. GmbH. [www.mitutoyo.de](http://www.mitutoyo.de).
- Munro, E. (1971). *Computer-aided-design methods in electron optics*, University of Cambridge: 251.
- NASA (1990). *Wake Vortex Study at Wallops Island*. <http://lisar.larc.nasa.gov/UTILS/info.cgi?id=EL-1996-00130>, NASA.
- Nye, J. F. and Berry, M. V. (1974). "Dislocations in wave trains." *Proc. Roy. Soc. London* **336**: 165-190.
- O'Mara, W. C. (1990). *Handbook of Semiconductor Silicon Technology*. William Andrew Inc. .
- Oosterbroek, R. E., Berenschot, J. W. E., Jansen, H. V., Nijdam, A. J., Pandraud, G., Berg, A. v. d. and Elwenspoek, M. C. (2000). "Etching Methodologies in <111> -Oriented Silicon Wafers." *Journal of Microelectromechanical Systems* **9**(3): 390-398.
- Orloff, J. (1997). *Handbook of Charged Particle Optics*, CRC Press.
- Padgett, M. and Bowman, R. (2011). "Tweezers with a twist." *Nature Photonics* **5**: 343–348.
- Padgett, M. J. and Allen, L. (1995). "The Poynting vector in Laguerre-Gaussian laser modes." *Optics Communications* **121**: 36-40.
- Phillips, R. L. and Andrews, L. C. (1983). "Spot size and divergence for Laguerre Gaussian beams of any order." *Applied Optics* **22**(5): 643-644.

Rittweger, E., Han, K. Y., Irvine, S. E., Eggeling, C. and Hell, S. W. (2009). "STED microscopy reveals crystal colour centres with nanometric resolution." *Nature Photonics* **3**: 144-147.

Rüdenberg, R. (1943). "The Early History of the Electron Microscope." *Journal of Applied Physics* **14**: 434.

Rusz, J. and Bhowmick, S. (2013). "Boundaries for Efficient Use of Electron Vortex Beams to Measure Magnetic Properties." *Physical Review Letters* **111**: 105504.

Saleh, B. E. A. and Teich, M. C. (2007). *Fundamentals of Photonics Second Edition*, John Wiley

Schachinger, T. (2012). Project Work: "Klassische Elektronenbahnen in magnetostatischen Dipolfeldern", TU Vienna.

Schattschneider, P., Löffler, S., Stöger-Pollach, M. and Verbeeck, J. (2012). "Is magnetic chiral dichroism feasible with electron vortices?" *Ultramicroscopy* **136**: 81-85.

Schattschneider, P., Schachinger, T., Stöger-Pollach, M., Löffler, S., Steiger-Thirsfeld, A., Bliokh, K. Y. and Nori, F. (submitted). "Imaging the Dynamics of Free-Electron Landau States." *Science*.

Schattschneider, P., Stöger-Pollach, M., Löffler, S., Steiger-Thirsfeld, A., Hell, J. and Verbeeck, J. (2012a). "Sub-nanometer free electrons with topological charge." *Ultramicroscopy* **115**: 21-25.

Schattschneider, P., Stöger-Pollach, M. and Verbeeck, J. (2012b). "Novel Vortex Generator and Mode Converter for Electron Beams." *Physical Review Letters* **109**: 084801- 084806.

Schattschneider, P., Stöger-Pollach, M. and Werner, W. (2011). "Electron Beam Techniques for Nanoanalysis." *Lecture Notes*.

Schattschneider, P. and Verbeeck, J. (2011). "Theory of free electron vortices." *Ultramicroscopy* **111**: 1461.

Schattschneider, P., Verbeeck, J., Mauchamp, V., Jaouen, M. and Hamon, A.-L. (2010). "Real-space simulations of spin-polarized electronic transitions in iron." *Physical Review B* **82**: 144418.

Scheineff, M. R. (1989). "Second order transfer matrices for inhomogeneous field Wien filters including spin precession." *Optik* **82**: 99-113.

Scherzer, O. (1936). "Über einige Fehler von Elektronenlinsen." *Zeitschrift für Physik* **101**(9-10): 593-603.

Schmitt-Measurement-Systems (2000). *Raoughness Average Overview*. I. Schmitt Measurement Systems. <http://www.schmitt-ind.com>.

Serabyn, E., Mawet, D. and Burruss, R. (2010). "An image of an exoplanet separated by two diffraction beamwidths from a star." *Nature* **464**: 1018-1020.

Shuvaev, A., Pimenov, A., Astakhov, G. V., Mühlbauer, M. and Molenkamp, L. W. (2013). "Room temperature electrically tunable terahertz Faraday effect." *Applied Physics Letters* **102**: 241902.

Steiger-Thirfield, A. (2013). Personal communication, FIB milling roughness approximately 5 nm mostly due to drift for larger structures.

Tamburini, F., Mari, E., Thidé, B., Barbieri, C. and Romanato, F. (2011). "Experimental verification of photon angular momentum and vorticity with radio techniques." *Applied Physics Letters* **99**: 204102.

Teichert, C., MacKay, J. F., Savage, D. E., Lagally, M. G., Brohl, M. and Wagner, P. (1995). "Comparison of surface roughness of polished silicon wafers measured by light scattering topography, softxray scattering, and atomicforce microscopy." *Applied Physics Letters* **66**.

Tiemeijer, P. (2012). "Personal Communication: The relative z-height indication of the stage is fairly accurate, within a few percent."

Tiemeijer, P. (2013). Personal Communication: Simulated B-Field of a T20 SuperTwin at 200kV equals 1.89T.

Torres, J. P. and Torner, L. (2011). Twisted Photons-Applications of Light with Orbital Angular Momentum.

Uchida, M. and Tonomura, A. (2010). "Generation of electron beams carrying orbital angular momentum." *Nature* **464**(08904): 737-739.

Uhlenbeck, G. E. and Goudsmit, S. (1925). "Ersetzung der Hypothese vom unmechanischen Zwang durch eine Forderung bezüglich des inneren Verhaltens jedes einzelnen Elektrons." *Die Naturwissenschaften* **47**(20/II).

UniblueSystems (2013). ".DM3 File information script." Retrieved 01.09.2013, 2013, from <http://filext.com/file-extension/DM3>.

Varmchuk, E. J. and Gordon, M. J. V. (1979). "Observation of Stationary Vortex Arrays in Rotating Superfluid Helium." *Physical Review Letters* **43**(3): 214.

Verbeeck, J., Tian, H. and Béch e, A. (2012). "A new way of producing electron vortex probes for STEM." *Ultramicroscopy* **113**: 83–87.

Verbeeck, J., Tian, H. and Schattschneider, P. (2010a). "Production and application of electron vortex beams." *Nature* **467**(09366): 301-304.

Verbeeck, J., Tian, H. and Schattschneider, P. (2010b). "Production and application of electron vortex beams - supplementary information." *Nature* **467**: 09366.

Verbeeck, J., Tian, H. and Tendeloo, G. V. (2013). "How to Manipulate Nanoparticles with an Electron Beam?" *Advanced Materials* **25**: 1114-1117.

Williams, D. B. and Carter, C. B. (1996). *Transmission Electron Microscopy*.

Xin, H. L. and Zheng, H. (2012). "On-column 2p bound state with topological charge  $\pm 1$  excited by an atomic-size vortex beam in an aberration-corrected scanning transmission electron microscope." *Microscopy and Microanalysis* **18**(4): 711-719.



Zhao, Y., Edgar, J. S., Jeffries, G. D. M., McGloin, D. and Chiu, D. T. (2007). "Spin-to-Orbital Angular Momentum Conversion in a Strongly Focused Optical Beam." *Physical Review Letters* **99**.

Zheng, H., Mirsaidov, U. M., Wang, L.-W. and Matsudaira, P. (2012). "Electron Beam Manipulation of Nanoparticles." *Nano Letters* **12**: 5644–5648.

Zweck, J. (2013). Personal Communication: Measured B-Field of a Tecnai at 92.77% objective excitation equals 1.87 T.



“Truth is ever found in simplicity, never in the multiplicity and confusion of things”, Isaac Newton.